Structure and Transport in Epitaxial $BaSnO_3$: Doping, Mobility and the Insulator-Metal Transition

A DISSERTATION

SUBMITTED TO THE FACULTY OF THE

UNIVERSITY OF MINNESOTA

BY

Koustav Ganguly

IN PARTIAL FULFILLMENT OF THE REQUIREMENTS

FOR THE DEGREE OF

DOCTOR OF PHILOSOPHY

Advisors: Bharat Jalan and Chris Leighton

August 2018

Acknowledgments

The work presented in this dissertation would not have been accomplished without the contributions of several people living in two different continents. My biggest thanks go to my advisors, Bharat Jalan and Chris Leighton, for their continuous support, guidance, and motivation during the course of my Ph.D. They are both outstanding scientists and teachers, and it has been a privilege for me to have worked in their labs. Their constant push to be the best at what they do always motivates me to strive for excellence as well. Our meetings and discussions over the last six years have not only helped me with my research and scientific training, but also made me more confident and prepared to face real-world problems. My whole experience working with them has been truly priceless, and I thank them deeply for that.

I have also been fortunate enough to have worked with several talented members of the Jalan and Leighton groups. Shameek Bose and Palak Ambwani were the senior graduate students when I joined the groups and were instrumental in not only training me on the various synthesis and characterization equipment but also in helping me handle the frustrations of failed experiments, bad films, or broken sputtering targets. I have also benefitted immensely from the numerous discussions I have had with Mike Manno, Danny Phelan, Liam O'Brien, Srinivas Polisetty, Vina Faramarzi, Eric McCalla, Joe Batley, Laxman Thoutam, Ryan Haislmaier, Xin Zhang, Bob Newman, Peng Xu, Jeff Walter, Tianqi Wang, Abhinav Prakash, Justin Watts, Helin Wang, Yanjun Yang, Bryan Voigt, Alan Albrecht, Bill Nunn, Jin Yue, Will Postiglione, John Dewey, Linmin Wang, Vipul Chaturvedi, Jialiang Chen, Shutong Li, and Tristan Truttmann. Furthermore, I have been lucky to have had the opportunity to mentor a talented bunch of undergraduate students – Nathaniel Kraft, Chris Cheng, and Lindsey Borgeson, who have all run experiments for me on several occasions. Some of these talented people have left the group to enjoy successful academic and industrial careers. I wish them all the very best in all their future endeavors. My special thanks go to Will Postiglione. His help with the last section of my dissertation was instrumental. Together we have tackled many challenges associated with film growth

and electron mobility optimization, and have learned from each other in the process. I would also like to acknowledge the efforts of Jeff Walter and Helin Wang with regards to the successful demonstration of ion-gel gating behavior in $BaSnO_3$. It is truly amazing to see what started as a discussion (one of several) between Jeff and me on a fine Friday evening is now a Ph.D. research project for Helin. The help I received from Tianqi Wang and Abhinav Prakash during vacuum annealing of my films cannot be overemphasized. They have run numerous annealing experiments for me at odd hours and on very short notice.

I would like to whole-heartedly thank Hwanhui Yun, Prof. Andre Mkhoyan, and Prof. Jong Seok Jeong for not only help with STEM imaging, but also for several discussions and ideas. Hwanhui's enthusiasm for research is contagious and awe-inspiring. None of the work discussed here would be possible without the constant support of the wonderful staff of the Chemical Engineering and Materials Science department. I would like to especially thank Teresa Bredahl and Julie Prince for helping me with day to day logistical and academic issues. I remember showing up in their offices clueless about what to do, and they would always guide me in the right direction. I would also like to acknowledge the help I received over the years from Mary Nissen, Jody Pepper, Chris Fruzyna, Danny Williams, Gayle Gabrielski, Fathi Ibrahim, Dan McDonald, Jim Pirie, Ann Tran, Lisa Wissbaum, Phil Engen, and Ted Butler.

Outside the department, I would like to thank Boyi Yang and Prof. Alan Goldman in the Physics department, Javi Barriocanal, Linda Sauer, Bing Lou, and Greg Haugstad at the Minnesota Characterization Facility, and Kyle Hoffman, Eric Suter, and Doug Bird at Quantum Design for their crucial help in several stages of my research.

Beyond academia, friends were the best part of my life here in Minneapolis. When I came to the US in 2012, I did not realize that there was more than just academics waiting for me here. My friends have always been there for me, through thick and thin. Along the way, we have had some great memories to cherish forever.

Finally, I want to take this opportunity to thank Prof. S. K. Roy, Prof. R. Mitra, Aniruddha Jana, and Soham Hazra from my undergraduate days in IIT Kharagpur. Prof. Roy has always been a great mentor to me throughout my academic career. It was his encouragement and guidance that made me come to the US for higher studies.

Last but not the least, I would like to acknowledge my family for their constant support and encouragement over the years. My parents and grandmother deserve the most important place in this dissertation and it is to them whom I dedicate this dissertation. Thank you for always believing in me. You guys are the best!

Koustav Ganguly

To my parents and grandmother,
who have all waited long for this day.

Abstract

The recent discovery of high room temperature electron mobility in wide band gap $BaSnO_3$ (BSO) has generated exceptional interest in this perovskite oxide for electronic devices. Outstanding issues with regards to epitaxial films include understanding transport mechanisms, determining the optimal dopant, and understanding the role of structural defects (like dislocations) in limiting mobility. Here, we discuss detailed temperature and field-dependent electronic transport in both oxygen vacancy and La-doped BSO films grown *via* high pressure oxygen sputter deposition. High-resolution X-ray diffraction (HRXRD), atomic force microscopy (AFM), and scanning transmission electron microscopy (STEM) confirm phase-pure, close to stoichiometric, smooth, epitaxial BSO(001). Film thickness, growth rate, deposition temperature, and substrate (*i.e.*, lattice mismatch) have all been systematically varied and related to mobility. Detailed transport accompanied with STEM has been used to understand the structure-electronic property relationships and reveal the correlation between misfit and threading dislocations in BSO thin films. As-grown undoped, insulating films can be made conductive with *controllable n*-type doping by vacuum reduction, resulting in 300 K Hall mobilities up to 35 $cm^2V^{-1}s^{-1}$ (on $LaAlO_3$(001)) at 5×10^{19} cm^{-3}. The mobility-electron density relation has been probed in this manner, down to 2×10^{17} cm^{-3}, the lowest electron density probed in BSO till date. 2% La-doped BSO films, on the other hand, demonstrate 300 K electron mobilities up to 70 $cm^2V^{-1}s^{-1}$ at ~2×10^{20} electrons per cm^3. With increasing film thickness a clear insulator-metal transition is observed with both dopants, likely related to defect density near the substrate. The low temperature upturn in resistivity observed in metallic-like BSO has been analyzed using out-of-plane and in-plane magnetoresistance (MR) measurements. Two-dimensional weak localization (WL) has been identified as the underlying mechanism behind this low temperature quantum correction. Overall, the results not only validate the technique of high-pressure oxygen sputtering as a viable approach to produce high quality BSO films, but also provide insight into the mobility-electron density relation, and mobility-limiting factors in these films. The mobility values reported in this thesis are

record values for sputtered films and are comparable to that obtained *via* pulsed laser deposition (PLD) in previous studies.

List of Publications

Koustav Ganguly, H. Yun, W.M. Postiglione, L. Borgeson, J.S. Jeong, K.A. Mkhoyan, B. Jalan, and C. Leighton, "Structure and mobility optimization of high-pressure-oxygen-sputtered $Ba_{0.98}La_{0.02}SnO_3$ thin films", in preparation for submission to *Physical Review Materials*.

Koustav Ganguly, W.M. Postiglione, L. Borgeson, A. Prakash, H. Yun, J.S. Jeong, K.A. Mkhoyan, B. Yang, A.M. Goldman, B. Jalan, and C. Leighton, "Thickness-driven insulator-metal transition and two-dimensional weak localization in epitaxial $BaSnO_3$ thin films", in preparation for submission to *Physical Review Materials*.

H. Yun, **Koustav Ganguly**, W.M. Postiglione, B. Jalan, C. Leighton, K.A. Mkhoyan, and J.S. Jeong,"Microstructure characterization of $BaSnO_3$ thin films grown on $LaAlO_3$ and $PrScO_3$ substrates using transmission electron microscopy", *Scientific Reports* **8**, 10245 (2018).

H. Yun, M. Topsakal, A. Prakash, **Koustav Ganguly**, C. Leighton, B. Jalan, R.M. Wentzcovitch, K.A. Mkhoyan, and J.S. Jeong, "Electronic structure of $BaSnO_3$ investigated by high-energy-resolution electron energy-loss spectroscopy and ab initio calculations", *Journal of Vacuum Science and Technology A* **36**, 031503 (2018).

Koustav Ganguly, A. Prakash, B. Jalan, and C. Leighton, "Mobility-electron density relation probed *via* controlled oxygen vacancy doping in epitaxial $BaSnO_3$", *APL Materials* **5**, 056102 (2017).

X. Ren, E. Schmidt, J. Walter, **Koustav Ganguly**, C. Leighton, C.D. Frisbie, "Rubrene single-crystal transistors with perfluoropolyether liquid dielectric: exploiting free dipoles to induce charge carriers at organic surfaces", *Journal of Physical Chemistry C* **121**, 6540 (2017).

Koustav Ganguly, P. Ambwani, P. Xu, J.S. Jeong, K.A. Mkhoyan, C. Leighton, and B. Jalan, "Structure and transport in high pressure oxygen sputter-deposited $BaSnO_{3-\delta}$", *APL Materials* **3**, 062509 (2015)

T. Wang, **Koustav Ganguly**, P. Marshall, P. Xu, and B. Jalan, "Critical thickness and strain relaxation in molecular beam epitaxy-grown $SrTiO_3$ films", *Applied Physics Letters* **103**, 212904 (2013)

Contents

List of Tables

Chapter 1

Chapter 7

List of Figures

Chapter 1

Chapter 2

Chapter 3

Chapter 4

Chapter 5

Chapter 6

Chapter 7

Chapter 8

List of Abbreviations

STO	$SrTiO_3$
RRR	Residual Resistivity Ratio
2DEG	Two-Dimensional Electron Gas
LAO	$LaAlO_3$
HEMT	High-Electron-Mobility Transistor
CB	Conduction Band
TCO	Transparent Conducting Oxide
BSO	$BaSnO_3$
CBM	Conduction Band Minimum
VBM	Valence Band Maximum
BSO:La	$Ba_{1-x}La_xSnO_3$
PLD	Pulsed Laser Deposition
MBE	Molecular Beam Epitaxy
MIT	Metal-Insulator Transition
PVD	Physical Vapor Deposition
TMP	Turbomolecular Pump
DC	Direct Current
RF	Radio Frequency
XRD	X-Ray Diffraction

HRXRD	High-Resolution X-Ray Diffraction
WAXRD	Wide-Angle X-Ray Diffraction
RC	Rocking Curve
RSM	Reciprocal Space Mapping
FWHM	Full-Width-at-Half-Maxima
SLD	Scattering Length Density
2D	Two Dimensional
GIXR	Grazing Incidence X-Ray Reflectivity
GIIXD	Grazing Incidence In-plane X-ray Diffraction
AFM	Atomic Force Microscopy
PSD	Position Sensitive Detector
PID	Proportional-Integral-Derivative
SEM	Scanning Electron Microscopy
SE	Secondary Electron
BE	Backscatter Electron
EDAX	Energy Dispersive Analysis of X-rays
EDS	Energy Dispersive Spectroscopy
PIXE	Particle-Induced X-ray Emission
TEM	Transmission Electron Microscopy
STEM	Scanning Transmission Electron Microscopy
BF	Bright Field
ADF	Annular Dark-Field

FIB	Focused Ion Beam
EELS	Electron Energy-Loss Spectroscopy
LAADF	Low-Angle Annular Dark-Field
MAADF	Medium-Angle Annular Dark-Field
HAADF	High-Angle Annular Dark-Field
AC	Alternating Current
PPMS	Physical Property Measurement System
IMT	Insulator-Metal Transition
HRTEM	High-Resolution Transmission Electron Microscopy
GSO	$GdScO_3$
TD	Threading Dislocation
MD	Misfit Dislocation
WL	Weak Localization
MR	Magnetoresistance
LSAT	$(La_{0.3}Sr_{0.7})(Al_{0.65}Ta_{0.35})O_3$
PSO	$PrScO_3$

"What man is a man who does not make the world better."

Balian of Ibelin

Kingdom of Heaven (2005)

Chapter 1: Introduction

1.1 Perovskite Oxides

Metal oxides are a group of earth-abundant materials that display properties relevant to numerous technological applications. Depending on the number of components, these oxides can range from simple binary oxides, such as ZnO, to more complex ternary and quaternary formulations containing multiple cations. A particular class of *complex* metal oxides that have generated much attention over the past few decades are the perovskites. Named after the eponymous mineral $CaTiO_3$, perovskite oxides have a general chemical formula of ABO_3 and crystallize in a structure shown in Fig. 1.1(a). Although this cubic representation is an oversimplification for most perovskite crystals, it is useful in depicting the three ionic sites in the unit cell: corners represent the *A* site, the body center represents the *B* site, and the face centers are occupied by oxygen. The six oxygen ions surrounding the *B* site cation form an octahedral cage, and the crystal structure in Fig 1.1(a) can be equivalently visualized as a three-dimensional network of corner-shared BO_6 octahedra, as shown in Fig. 1.1(b).

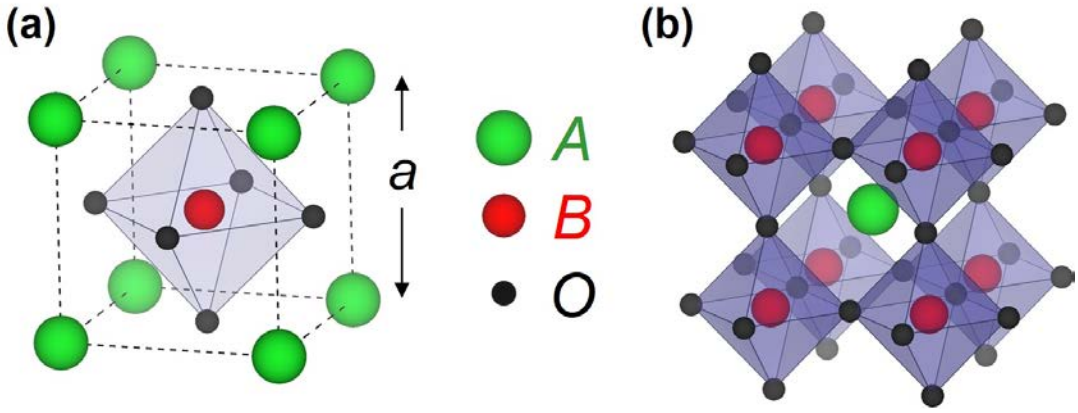

Fig. 1.1: (a) The perovskite unit cell showing the positions of the *A* site, *B* site, and oxygen. (b) An alternate presentation of the same crystal showing a three-dimensional network of corner shared BO_6 octahedra.

Assuming the ions are rigid spheres that touch along the edge and face diagonal of the cube in Fig. 1.1(a), the lattice parameter, *a*, can be related to the ionic radii of the *A*, *B*, and O ions (R_A, R_B, and R_O, respectively) through simple geometry as:

$$2(R_A + R_O) = \sqrt{2}a \qquad \text{and} \qquad 2(R_B + R_O) = a \tag{1.1}$$

The above equalities both hold true only for an ideal cubic unit cell. In general, a Goldschmidt tolerance factor, *t*, is used to quantify deviations from the ideal cubic structure and is defined by:

$$t = \frac{R_A + R_O}{\sqrt{2}(R_B + R_O)} \tag{1.2}$$

Comparing Eqs.1.1 and 1.2, it becomes clear that $t = 1$ for the cubic crystal structure. Surprisingly, the perovskite structure is extremely amenable to variations in the ionic radii of the *A* and *B* cations, thus resulting in *t* values in the range of 0.89 – 1.02. This variation in *t* is accommodated through tilting and distortion of the BO_6 octahedra, and is accompanied by displacements of the cations and changes in the *B*–O–*B* bond angle (Fig. 1.2). This lowers the crystal symmetry from cubic to tetragonal, rhombohedral, orthorhombic, monoclinic and triclinic [1, 2].

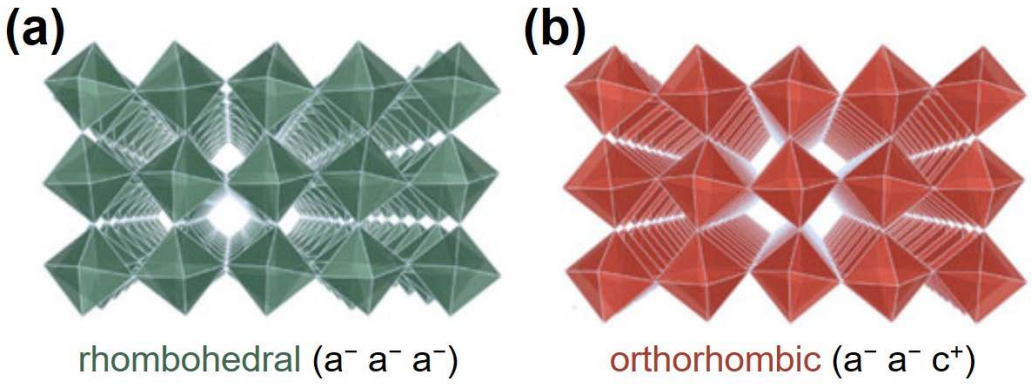

Fig. 1.2: Schematic illustration of the BO_6 octahedral tilting in perovskite oxides with (a) rhombohedral, and (b) orthorhombic crystal structures. The rotational patterns are also indicated. Figure adapted from [2].

The elements from the periodic table that can fill the *A* and *B* sites without destabilizing the perovskite lattice are shown in Fig. 1.3(a). Owing to the staggeringly large number of *A* and *B* cation combinations, perovskite oxides display a myriad of diverse functionalities, including ferromagnetism [3], ferroelectricity [4], piezoelectricity [5], high T_c superconductivity [6], and colossal magnetoresistance [7] (Fig. 1.3(b)).

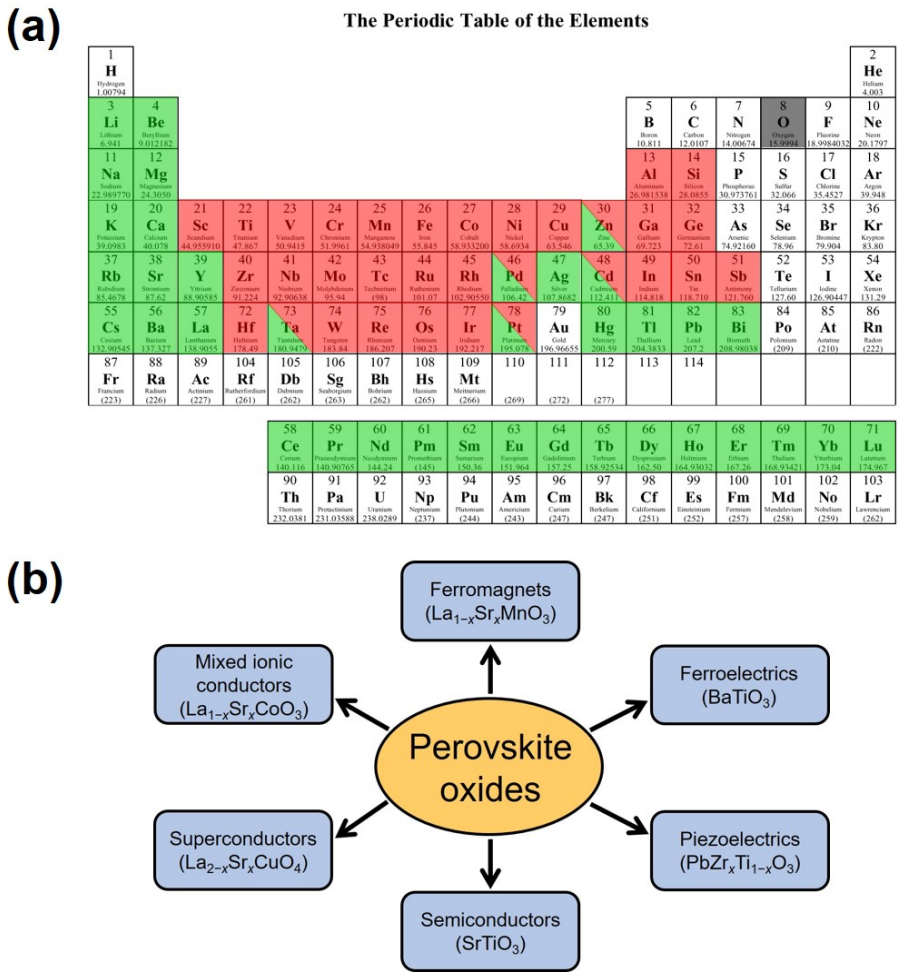

Fig. 1.3: (a) The periodic table highlighting the elements that can be incorporated into the perovskite structure. Elements shaded in green can go into the *A* site, while those in red can go into the *B* site. (b) Diverse functionalities of perovskite oxides and their derived structures.

Furthermore, these properties can be enhanced or controlled *via* doping, strain, or proximity effects. Chemical doping in perovskite oxides is achieved by heterovalent substitutions at the *A* or *B* sites, or by the creation of oxygen vacancies (V_O). For instance, the substitution of a trivalent cation *a* on a divalent *A* site can be expressed as: $a + A_A^x \rightarrow a_A^{\cdot} + A + e^{'}$. Similarly, in a very simplistic picture, each V_O can be thought to generate two electrons following the defect reaction: $O_O^x \rightarrow {}^1/_2\, O_2(g) + V_O^{\cdot\cdot} + 2e^{'}$. In addition to the rich variety of bulk properties in perovskite oxides, novel phenomena are often observed in thin films. Moreover, close lattice matching between perovskite oxides opens up an interesting avenue for seamless stacking of different thin films into one composite structure, termed as a *heterostructure*. Heterostructures can range from being as simple as a single interface between two compounds to much more complicated superlattices of different compounds. These can not only integrate multiple functionalities in the same structure but can occasionally result in the observation of ground states that are absent from the individual constituents. A classic example is the existence of interface metallicity in the heterostructure of two insulators $LaAlO_3$ and $SrTiO_3$ [8].

1.2 $SrTiO_3$: The Archetypal Perovskite Oxide

Strontium titanate ($SrTiO_3$) or simply STO, a popular substrate choice for epitaxy of complex oxides, is the most heavily studied perovskite oxide. STO has a cubic ($Pm\bar{3}m$) crystal structure with a lattice parameter of 3.905 Å at room temperature. However, below 105 K, neighboring TiO_6 octahedra rotate in opposite directions (antiferrodistortive), thus lowering the crystal symmetry to form a tetragonal structure [9, 10]. STO is believed to be

a quantum paraelectric, where the onset of a spontaneous polarization (at low temperatures) is suppressed by quantum fluctuations. STO's high dielectric constant (ε_r) of 300 at room temperature increases to tens of thousands at low temperatures and shows large deviations from the Curie-Weiss behavior [11-13].

In addition to possessing remarkable dielectric properties, STO is also a wide band-gap semiconductor with an indirect gap of 3.2 eV separating the O-2*p* valence band from the Ti-3*d* conduction band [14]. It can be easily doped *n*-type by Nb^{5+} (for Ti^{4+}) or La^{3+} (for Sr^{2+}) substitution or with V_O [15-18]. Large temperature (*T*)-dependent ε_r and scattering rates result in a large Bohr radius, negligible donor binding energies, large residual resistivity ratios (RRRs), the absence of carrier freeze-out, and high electron mobilities. Low temperature electron mobility (μ) as high as 22,000 $cm^2V^{-1}s^{-1}$ has been observed in *n*-type STO single crystals, increasing up to at least 53,000 $cm^2V^{-1}s^{-1}$ in epitaxial thin films [15, 19, 20]. Mobility in the latter can be further improved to 120,000 $cm^2V^{-1}s^{-1}$ by application of uniaxial stress [21]. At room temperature, however, μ <10 $cm^2V^{-1}s^{-1}$ has been established as the limit for STO, which stood to be the highest among perovskite oxides for a long time until the discovery of high room temperature μ in the alkaline earth stannate, $BaSnO_3$.

1.3 Heterostructures and the Two-Dimensional Electron Gas

As mentioned above, heterostructures provide a rich and exciting playground for combination and enhancement of functionalities of perovskite oxides. Also, strong inter-layer coupling and a high density of interfaces in these heterostructures sometimes lead to the emergence of novel phenomena through modulation of charge, orbital, spin, and lattice degrees of freedom, as shown in Fig. 1.4 [22, 23]. The design of these heterostructures can range from being as simple as a single interface between two layers to much more complicated superlattices involving two or more perovskite oxides [24]. Growth techniques offering atomic scale precision are therefore a requirement for growing these complex structures with well defined atomically-sharp interfaces.

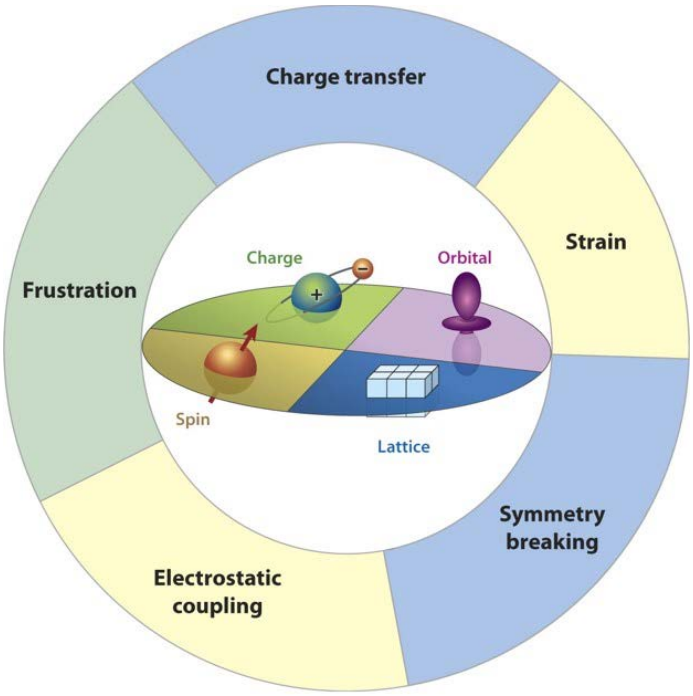

Fig. 1.4: Schematic showing the interplay of charge, orbital, spin, and lattice degrees of freedom in perovskite oxides, and how they can be tuned at heterostructure interfaces through local symmetry breaking, strain, charge transfer, frustration, and electrostatic coupling. Figure adapted from [23].

A typical example of an emergent phenomenon in perovskite oxides is the formation of a two-dimensional electron gas (2DEG) at the interface between a thin layer of $LaAlO_3$ (LAO) grown on a TiO_2-terminated STO(001) substrate [8]. The underlying mechanism for this interfacial metallicity still remains under debate, with V_O formation (Fig. 1.5(b)) and cation intermixing (Fig. 1.5(c)) thought to be as important as the intrinsic mechanism of the *polar catastrophe* (Fig. 1.5(d)) [25-28]. Along the (001) direction, STO is composed of alternating charge neutral layers of SrO and TiO_2, whereas, LAO is polar and consists of alternating LaO^+ and AlO_2^- layers. So, when LAO is grown epitaxially over a TiO_2-terminated STO(001), a strong polar discontinuity appears at the interface, leading to an electrostatic potential that increases linearly with LAO film thickness (Fig. 1.5(d)). To prevent this potential from diverging, electrons (0.5 e^-/u.c.) are transferred across the

interface from LAO to STO [28]. The observed 2DEG displayed temperature independent electron density (*n*) and μ exceeding 10,000 $cm^2V^{-1}s^{-1}$ at 2 K [8]. However, the μ value at 300 K was still < 10 $cm^2V^{-1}s^{-1}$. Similar polar-nonpolar heterointerfaces between rare earth titanates, $RTiO_3$ (*R* = La, Nd, and Gd) have also been studied showing 2D electron densities up to ~3 x 10^{14} cm^{-2} (0.5 e^-/u.c.) for $LaTiO_3$/STO and $GdTiO_3$/STO, and an unprecedented 3 x 10^{15} cm^{-2} for $NdTiO_3$/STO [29-34].

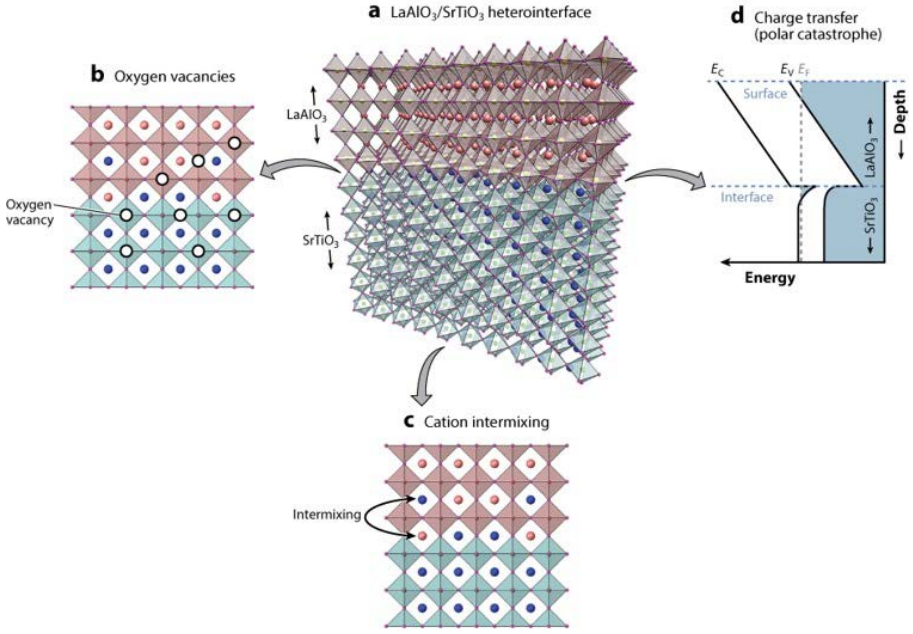

Fig. 1.5: (a) The $LaAlO_3/SrTiO_3$ heterointerface. Mechanisms such as (b) formation of oxygen vacancies, (c) cation intermixing, and (d) polar catastrophe are thought to be responsible for the interfacial conductivity in this heterostructure. Figure adapted from [10].

The spatial separation of the 2DEG from the donors, a technique termed as *modulation doping*, is a key concept that leads to high electron mobility. High mobilities and long mean free paths are essential for observing phenomena like Shubnikov-de Haas oscillations and quantum Hall effect, or to use these electron gases in high-electron-mobility transistors (HEMTs) [35, 36]. So far, titanate-based heterostructures have been at

the center of most studies on high mobility 2DEGs in perovskite oxides. Although these heterostructures exhibit extremely high μ (~10^4 $cm^2V^{-1}s^{-1}$) at low temperatures, the room temperature μ is < 10 $cm^2V^{-1}s^{-1}$. This significantly reduced mobility is attributed to the high electron effective mass in the Ti-3*d*-derived conduction band (CB) [37]. To obtain higher μ, highly dispersive CBs derived from *s*-orbitals are desirable and can be achieved, for example, by substitution of Ti by Sn.

1.4 $BaSnO_3$: A High Room Temperature Mobility Perovskite Oxide

Semiconducting oxides with predominantly *s*-orbital-derived conduction bands are attractive due to their potential for low electron effective mass and high room temperature mobility. ZnO is an illustrative example, with μ up to 430 $cm^2V^{-1}s^{-1}$ at ambient [38, 39], increasing to 700,000 $cm^2V^{-1}s^{-1}$ at cryogenic temperatures [40], enabling observation of the integer and fractional quantum Hall effects [39, 41]. Particularly in wide bandgap cases like ZnO, such semiconductors are also of interest as transparent conductive oxides (TCOs), as part of the drive to displace indium tin oxide [42]. While much exploration of binary wide gap semiconducting oxides has been stimulated, relatively little, in this regard, has been done with perovskite oxides. This is despite the remarkable chemical flexibility and functionality of perovskites (Sec. 1.1), which could potentially include high mobility wide band gap semiconductors. Realizing high room temperature μ in perovskites, potentially *via s*-bands rather than *d*-derived bands, is important for several reasons. Primary among these is the need, for the advancement of oxide electronics [10, 43-45], to translate the extraordinary diversity in functionality that has been demonstrated in perovskite oxide heterostructures to room temperature. A high room temperature mobility perovskite semiconductor could enable applications such as ambient temperature high mobility oxide two-dimensional electron systems, oxide transistors, and all-perovskite spintronic devices. In this context, the recent discovery of room temperature μ exceeding 300 $cm^2V^{-1}s^{-1}$ at unusually high electron densities (n ~10^{20} cm^{-3}) in wide band gap $BaSnO_3$ single crystals is significant [46-48]. This is the highest reported 300 K mobility in perovskite oxides and can be compared, for instance, to <10 $cm^2V^{-1}s^{-1}$ in STO [15]. BSO's

exceptional electronic transport properties suggest potential applications in transparent electronics [48, 49], room temperature two-dimensional electron systems [45, 50-52], high mobility oxide transistors [53-55], and power electronics [56, 57].

1.4.1 **Properties of $BaSnO_3$**

$BaSnO_3$ (BSO) belongs to a family of perovskite oxides called alkaline earth stannates, which have the generic chemical formula $ASnO_3$ (A = Ca, Sr and Ba). With the systematic increase in the ionic radius of the A-site cation (from Ca^{2+} to Ba^{2+}) the tolerance factor (t) increases from 0.927 to 1.018, and correspondingly the band gap decreases from 4.4 eV to 3 eV [58]. BSO adopts the ideal cubic crystal structure ($Pm\bar{3}m$) with a perfect 180° Sn–O–Sn bond angle and lattice parameter of 4.116 Å. A wide indirect band gap of $E_g \approx 3$ eV results in a visible transmittance ~80% [47, 59, 60]. In its bulk form, BSO shows remarkable thermal stability up to 1000 °C [61, 62], making it suitable for applications such as thermally stable capacitors and gas sensors [63].

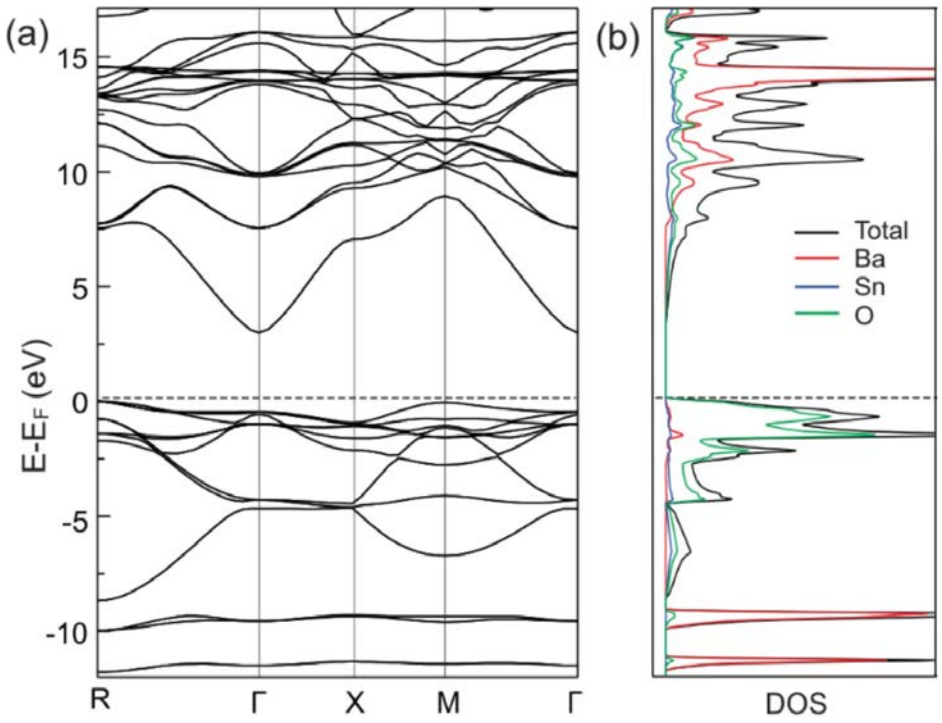

Fig. 1.6: (a) Calculated band structure and (b) corresponding density of states (DOS) of BSO. Figure adapted from [64].

The electron mobility (μ) of a material can, in a simplistic picture, be represented by the *Drude model* according to:

$$\mu = \frac{e\tau}{m_e^*} \tag{1.3}$$

where e is the electronic charge, m_e* is the electron effective mass, and τ^{-1} is the total scattering rate. So, according to Eq. 1.3, a decrease in m_e* and τ^{-1} will result in higher μ. Band structure calculations on $BaSnO_3$ have revealed that the conduction band minimum (CBM) and valence band maximum (VBM) are positioned at the Γ and R points in reciprocal space [52, 64-69], respectively, as shown in Fig. 1.6. The CBM is dominated by Sn-5*s* states, resulting in an increased dispersion of the CB, and in turn, a relatively small m_e*. Theoretically calculated values of m_e* vary substantially from $0.028 – 0.54m_e$ (where m_e is the electron rest mass) [37, 49, 52, 64, 67, 70, 71], as do experimentally determined values ($0.14 – 0.61m_e$) [72-79]. However, some of the more recent results cluster around m_e* ≈ $0.2m_e$ [72-74]. The other factor in Eq. 1 is the total scattering rate for the electrons, which at room temperature can be limited by phonons and impurities (both neutral and ionized) in BSO single crystals as shown in Fig. 1.7 [58]. A recent theoretical work quantitatively explained the high room temperature μ as a result of unusually low phonon scattering rates, roughly an order of magnitude smaller than in STO [69]. So, in essence, a combination of both small m_e* and small scattering rates is thought to give BSO its extraordinarily high room temperature mobility.

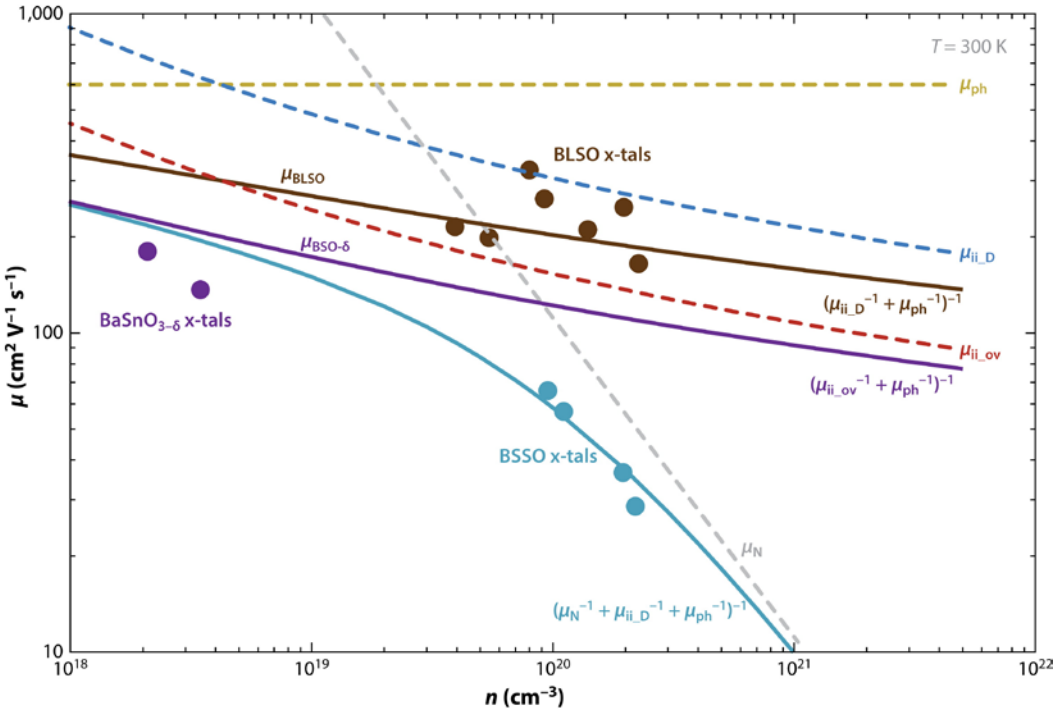

Fig. 1.7: Mobility (μ) *vs.* electron density (*n*) in doped BSO single crystals. Theoretically estimated μ curves from various scattering sources: phonons (μ_{ph}), neutral impurities (μ_N), and ionized impurities (μ_{ii}) are plotted as dashed lines. Solid lines are related to a combination of multiple scattering sources. Figure adapted from [58].

1.4.2 **Chemical Doping in $BaSnO_3$**

Like STO, BSO can also be doped by chemical substitution on either the *A* (Ba) or *B* (Sn) sites. While *p*-type doping has proved to be extremely challenging, *n*-type doping has commonly been achieved through La^{3+} substitution for Ba^{2+} and Sb^{5+} substitution for Sn^{4+}. By far the most widely studied doping has been the substitution of Ba by La (La_{Ba}). Lanthanum, like most rare earth elements, forms a stable +3 cation, and as such it acts as an electron donor in BSO. The bulk solubility limit for La_{Ba} has been experimentally determined to be ~3 – 4 at.%, above which the pyrochlore $La_2Sn_2O_7$ phase was seen to form as a second phase [46, 47]. However, this thermodynamic limit can be exceeded in

thin films deposited under non-equilibrium conditions, and even films with $x \approx 0.7$ have been reported [57]. The bulk lattice parameter, *a*, shows a linearly increasing trend *vs*. *x* [46, 47], even though La^{3+} (136 pm) has a smaller ionic radius compared to Ba^{2+} (161 pm) [80]. This is thought to be a consequence of the CB being mainly comprised of Sn-5*s* states with Sn–O antibonding character. The electrons donated by La^{3+} occupy these empty antibonding states and hence result in repulsive forces between Sn and O leading to a lattice expansion [47]. Liu *et al.* predicted the La donor level to be very shallow (~50 meV below the CB) in BSO [37] and, indeed, both $Ba_{1-x}La_xSnO_3$ (BSO:La) single crystals and thin films exhibit degenerate metallic conduction starting at a low dopant concentration (*x*). While bulk single crystals exhibit 300 K mobilities as high as 320 $cm^2V^{-1}s^{-1}$ [47, 48], epitaxial thin films show μ up to 183 $cm^2V^{-1}s^{-1}$ [81] at $n \sim 10^{20}$ cm^{-3}. The resulting conductivity (σ) in both cases is outstanding across all perovskite oxides, and even competitive with existing TCOs [57]. Gd-doped BSO epitaxial films have also been reported by Alaan *et al.* [82]. These films displayed $\mu(300\ K) \approx 30$ $cm^2V^{-1}s^{-1}$, while also exhibiting a strong paramagnetic moment; the field dependence of the magnetization (*M*) was shown to fit well to a Brillouin function with $g = 2$ and $J = 7/2$. A very recent study carried out in our group looked at the viability of Pr and Nd doping in BSO single crystals as well [83]. Magnetometry and heat capacity measurements were carried out to directly estimate dopant densities and electron effective mass.

While La has been the *ideal* dopant for the Ba site, Sb substitution at the Sn site (Sb_{Sn}) has also been reported. Sb ionizes to a +5 oxidation state and hence, like La is also an electron donor. Similar to La_{Ba}, an increasing, but markedly non-linear trend is observed in *a vs. x* up to the solubility limit of $x \approx 0.2$ [61, 84]. However, $BaSn_{1-x}Sb_xO_3$ (BSO:Sb) displays lower mobilities compared to its BSO:La counterpart, with single crystals exhibiting a maximum of ~80 $cm^2V^{-1}s^{-1}$ 300 K mobility at *n* of ~10^{20} cm^{-3} [75]. Moreover, Kim *et al.* reported that the observed electron densities were a factor of ~5 lower than the nominal doping concentration, possibly due to the formation of Sb interstitials, poor dopant activity, or significant electron compensation [75]. BSO:Sb thin films also show *n* values lower than expected and a maximum μ of ~20 $cm^2V^{-1}s^{-1}$ at $n \sim 5 \times 10^{20}$ cm^{-3} [76]. The

reduced μ in BSO:Sb has been attributed to an additional scattering mechanism active only for Sb_{Sn}. As the CB comprises Sn-5*s* hybridized with O-2*p* orbitals, the electron conducts through the SnO_6 octahedra. The Sb impurities directly interrupt this conduction pathway and hence scatters the electrons more effectively than La impurities [76].

Similar to STO, oxygen vacancies (V_O) should act as *n*-type dopants in BSO. However, density functional calculations have suggested quite high oxygen vacancy (V_O) formation energies and deep V_O donor levels [85]. While the formation of V_O during growth was presumed by Kim *et al.* to be responsible for the observed conductivity of undoped BSO single crystals [75], thick BSO:La films were shown to exhibit good oxygen stability up to 530 °C [86]. Prior to the publication of the work discussed in chapter 4 of this dissertation, it was thus not clear how facile V_O doping is in BSO, or whether it could provide an alternate route to *n*-type doping.

1.4.3 **Challenges with Epitaxy of $BaSnO_3$: Impact of Defects on Mobility**

In order to realize the devices and applications listed in Sec. 1.4, high quality epitaxial thin films of BSO are required. Thin film epitaxy not only relies on precise control over stoichiometry during deposition but also often on the use of substrates that are closely lattice-matched with the film. Stoichiometric films coherently grown on low mismatch substrates have very low defect densities and display properties that resemble or exceed those in bulk single crystals. For any given film-substrate combination, there is a critical thickness (t_{crit}) above which the film can release the elastic strain energy imposed by the substrate by forming an array of *misfit dislocations* at the interface. As expected, this critical film thickness relates inversely to the degree of mismatch between the film and the substrate. While group IV and III-V semiconductor thin films often display strain relaxation *via* this mechanism, in the case of perovskite oxides several other mechanisms have also been observed, such as octahedral tilting [2], oxygen vacancy ordering [87], ferroelectric domain formation [88], and structural phase transitions [89].

The Matthews-Blakeslee criterion [90] can be used to relate lattice mismatch to the t_{crit} for BSO grown on commercial substrates:

$$t_{crit} = \frac{|\boldsymbol{b}|}{2\pi|f|}\frac{(1-\upsilon\,cos^2\alpha)}{(1+\upsilon)\,cos\lambda}\,(ln\frac{t_{crit}}{|\boldsymbol{b}|}+1) \quad (1.4).$$

Here ν is the Poisson's ratio (~0.247 for BSO), $f\left(=\frac{a_{sub}-a_{film}}{a_{film}}\right)$ the misfit strain, $\boldsymbol{b}$ the dislocation Burgers vector (a [100]), α the angle between the dislocation line and its Burgers vector (90° for edge dislocations) and λ the angle between the dislocation line and the film/substrate interface (0° for dislocations lying at the interface). Table 1.1 lists the calculated values of t_{crit} for BSO films grown on some of the commercial substrates.

Table 1.1: Substrate structure, lattice parameter, and mismatch with $BaSnO_3$ (a = 4.116 Å)

Substrate	*a* [Å]	*Mismatch* [%]	t_{crit} [Å]
$LaAlO_3$ (rhombohedral)	3.789*	-8.6	10
LSAT† (cubic)	3.868	-6.4	20
$SrTiO_3$ (cubic)	3.905	-5.4	30
$DyScO_3$ (orthorhombic)	3.947*	-4.3	40
$GdScO_3$ (orthorhombic)	3.961*	-3.9	50
$KTaO_3$ (cubic)	3.989	-3.2	60
$PrScO_3$ (orthorhombic)	4.027*	-2.2	100
MgO (cubic, rock salt)	4.212	+2.3	100
$SrZrO_3$†† (orthorhombic)	4.101	-0.4	> 900

*Pseudocubic lattice parameter (See Appendix I) †$(La_{0.3}Sr_{0.7})(Al_{0.65}Ta_{0.35})O_3$

††$SrZrO_3$ is not a commercial substrate. It is listed here only to illustrate the critical thickness results for a well-matched material

The need for thin films for most applications has stimulated research on BSO epilayers grown *via* a variety of methods, such as pulsed laser deposition (PLD) [47, 48,

76, 82, 91], high pressure oxygen sputtering [92, 93], and oxide molecular beam epitaxy (MBE) [56, 57, 81, 94-96]. Similar to GaN [97], a primary difficulty is the dearth of appropriate commercial substrates near the 4.116 Å BSO lattice parameter, as shown in Table 1.1. Typically employed substrates (with lattice mismatches) include $SrTiO_3$ (-5.4%) and MgO (+2.3%), along with the more recently used $RScO_3$ (-2.2 to -4.3%), where R = Pr, Sm, Tb, and Dy. These mismatches result in low t_{crit} for strain relaxation in BSO films (Table 1.1), a high density of misfit dislocations (~10^{12} cm^{-2} in $SrTiO_3$(001)/BSO) [56, 92, 96] and, subsequently, significant threading dislocation densities (~10^{11} cm^{-2} in $DyScO_3$(001)/BSO) [81]. Mobilities in thin films are consequently lower than in bulk crystals, although progress is being made. Initial work on PLD of BSO:La on $SrTiO_3$(001) reported room temperature $\mu \approx 70$ $cm^2V^{-1}s^{-1}$ [47, 48], but recent improvements, including lower mismatch scandate substrates [56, 81, 91, 95], undoped buffer layers [55, 57, 98, 99], and higher purity MBE methods [56, 57, 81, 94, 95] have increased this to 183 $cm^2V^{-1}s^{-1}$ [81].

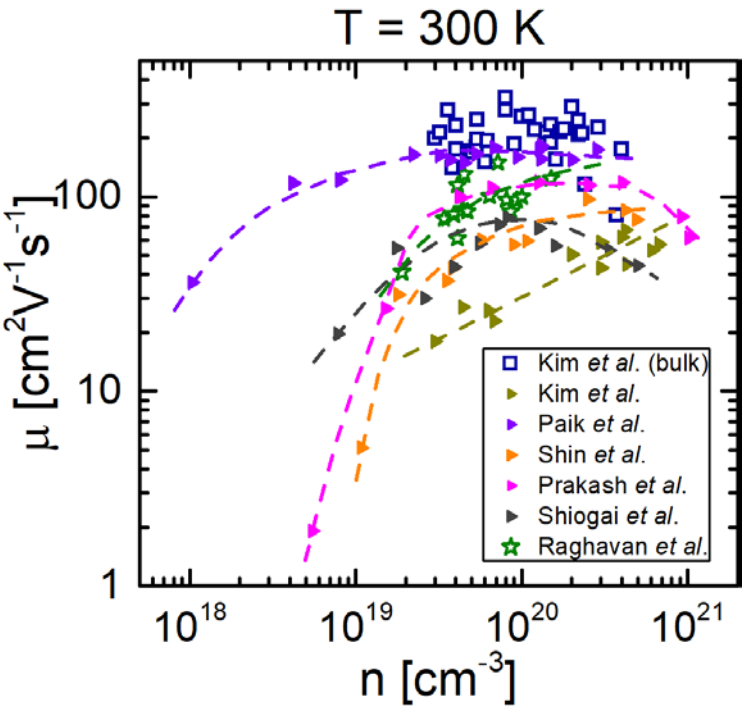

Fig. 1.8: Log-log plot of the 300 K Hall electron mobility, μ, *vs*. the 300 K Hall electron density, *n*, for the BSO:La from other reports in the literature [47, 48, 56, 57, 81, 98, 99]. The open square points are for bulk single crystals, and the solid points correspond to epitaxial films.

In contrast to bulk [47, 48], a common feature in these doped epitaxial BSO films is μ increasing significantly with *n* over the doping range probed [47, 48, 56, 57, 76, 81, 91, 93, 98, 100, 101], which can be seen in Fig. 1.8. This is typically attributed to improved screening of defects at higher *n*, although the effects of ionized impurities, dislocations, and non-stoichiometry are challenging to disentangle [57]. In related systems such as GaN, dislocation scattering results in $\mu \propto n^{1/2}$ [102], while in BSO a more complex μ(*n*) is observed; a recent work ascribed this to a crossover from dislocation-limited to ionized impurity-limited μ with increasing La doping [57]. This is shown in Fig. 1.9, where, as *n* increases in sequence from 1.5 x 10^{19} cm^{-3}, to 4 x 10^{20} cm^{-3}, and finally to 1 x 10^{21} cm^{-3}, the dominant mobility limiting mechanism changes from dislocation scattering, to both ionized impurity and phonon scattering, to finally just ionized impurity scattering. Although dislocations in BSO may be expected to be charged (as in GaN) [102], their exact structure and dislocation core electrostatics are unknown. In such a situation, gathering additional experimental information on the μ-*n* relation, especially in the dislocation dominated regime, is clearly important. Lightly-doped epitaxial BSO films with *n* below ~10^{19} cm^{-3} have only been probed to a limited extent so far (much like bulk crystals), likely due to difficulties with dopant incorporation/activity and compensation by acceptors/deep levels.

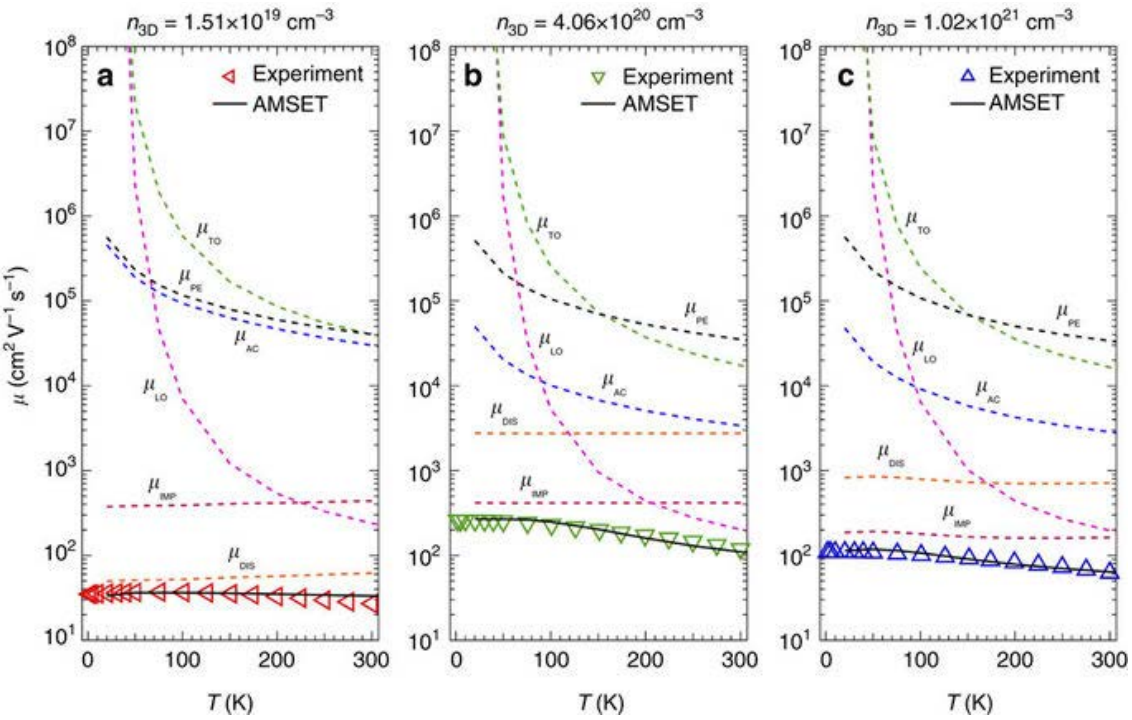

Fig. 1.9: Measurement temperature (*T*) dependence of μ for $Ba_{1-x}La_xSnO_3$ epitaxial films with (a) n = 1.5 x 10^{19} cm^{-3}, (b) n = 4 x 10^{20} cm^{-3}, and (c) 1 x 10^{21} cm^{-3}. Contributions from different electron scattering mechanisms are shown by the dashed lines. Dislocation density as calculated from the model were 2 x 10^{12} cm^{-2} in (a), 7 x 10^{11} cm^{-2} in (b), and 3 x 10^{12} cm^{-2} in (c). Figure adapted from [57].

While progress with mobility optimization in heteroepitaxial BSO films has been rapid, open questions still remain regarding mobility-limiting scattering rates and conduction mechanisms in general. A low temperature resistivity upturn is frequently observed in $BaSnO_3$, suggesting proximity to a disorder-driven metal-insulator transition (MIT). Understanding the metal-insulator transition in BSO is a key missing component in the literature and will be essential to answer questions about the role of defects in determining the electronic ground-state in BSO. Moreover, a thorough study of structure and mobility optimization by systematic variation of growth parameters will be crucial in establishing structure-electronic property relationships in BSO thin films. The work

discussed in this thesis tries to answer some of these open questions pertaining to BSO thin films.

Chapter 2: Experimental Methods

This chapter discusses the methods used for synthesis and characterization of $BaSnO_3$ (BSO) polycrystalline sputtering targets and epitaxial thin films. The first part of the chapter describes the methods used for the synthesis of bulk targets (Sec. 2.1.1) and thin films (Sec. 2.1.2), whereas the second part focuses on the various structural (Sec. 2.2) and electronic transport characterization (Sec. 2.3) techniques used in this work.

2.1 Synthesis

Two forms of BSO were primarily used in this study: (a) polycrystalline powders, and (b) epitaxial thin films sputter-deposited on commercial single crystalline substrates. Synthesis of stoichiometric polycrystalline powders was necessary to make bulk sputtering targets. Details of the steps involved in powder processing, sintering, and target bonding are described in Sec. 2.1.1. Thin film BSO was deposited *via*. high pressure oxygen sputtering from the bulk targets as discussed in Sec. 2.1.2. The commercial single crystal substrates used for thin film deposition are considered in Sec. 2.1.2.2.

2.1.1 Synthesis of Bulk $BaSnO_3$ Sputtering Targets

$Ba_{1-x}La_xSnO_3$ (x = 0, 0.002, 0.02, and 0.1) sputtering targets were synthesized by following standard powder processing, cold compaction, and sintering steps [103]. First, $BaCO_3$, La_2O_3, and SnO_2 (Sigma-Aldrich Co., purity > 99.9%) precursor powders were dried at elevated temperatures to get rid of absorbed moisture. A 24 hr. drying cycle at 1000 °C was used for La_2O_3 (extremely hygroscopic), whereas a 3 hr. cycle at 300 °C was used for the rest. Following the drying schedule, stoichiometric amounts of the powders were weighed while hot, and subsequently mixed and ground for 1 – 3 hrs. (depending on La content) in an alumina mortar and pestle procured from CoorsTek, Inc. Grinding ensures reduction of particle size (larger surface area is favorable for solid-state reaction) and homogeneous mixing of the reactant powders. The mixed powders were then transferred

to an alumina crucible (CoorsTek, Inc.) to be placed in a box furnace (Carbolite RHF 1600) for carrying out the solid-state reaction: $(1-x)\ BaCO_3\,(s) + x\ La_2O_3\,(s) + SnO_2\,(s) \rightarrow Ba_{1-x}La_xSnO_3\,(s) + CO_2\,(g)\uparrow$. The reactants were held at 1200 °C for 24 hrs. to react in air. The reacted powders were then re-ground and reacted again. This process was repeated until the resulting powders were confirmed by X-ray powder diffraction (Sec. 2.2.1.2) to be phase-pure. A total reaction time of 72 hrs. was observed to be typical for BSO.

Once the reaction was complete, the powders were mixed with an organic liquid binding agent and then packed into a 2" diameter stainless steel die for uniaxial compaction. The binder comprised of deionized water (350 ml), glycerine (100 ml, Fisher Scientific, 99.5%), and polyvinyl alcohol (10 g, Sigma-Aldrich Co., 99%, hydrolyzed). The cold compaction was done in an automated single action press at a force of 40,000 lbs (3200 psi). In addition to the 2" diameter ceramic discs, smaller 0.5" diameter pellets were also produced using an equivalent pressure. The latter would serve as representative samples for structural and electronic transport characterizations. Next, the compacted discs and pellets were sintered in air at 1350 – 1550 °C for 24 hrs. to promote densification and improve the structural integrity of the ceramic compacts. Sintering was carried out in the Carbolite RHF 1600 box furnace, where each compact was placed in between two flat alumina plates to prevent warping (resulting from temperature variation within the compact). Note that the furnace was brought down from high temperature very slowly, at 0.5 °C/min, to avoid thermal shock induced target cracking. After the sintering step, the targets were sanded using 3M 600 grit sandpaper to ensure thickness uniformity and removal of any visible surface imperfections.

Mechanically compact sintered targets need to be bonded to Cu backing plates before they can be mounted onto the sputtering gun in the high pressure oxygen sputtering chamber. A Cu backing plate ensures that the target is in electrical contact with the cathode and thermal contact with the target transfer rod. Owing to a sizable difference in their impedance, undoped (insulating) and La-doped (metallic) BSO targets had to be sputtered using RF and DC modes, respectively. As such, the targets had to be bonded to the Cu backing plates using two different bonding agents. A thermally and electrically conductive

Ag-based epoxy, Epotek H20E (Ted Pella, Inc.), was used to bond an undoped BSO target to a 1" Cu backing plate for RF sputtering. After application, curing of the epoxy was carried out on a hotplate at ~100 °C for 1.5 hrs. The consensus to use this epoxy was reached after many previous failed target bonding experiments with other epoxies like Torr Seal (Kurt J. Lesker Co.) and Epotek H70E (Ted Pella, Inc.). La-doped BSO DC targets, on the other hand, were bonded onto a 2" Cu backing plate using indium. First, Indium was soldered to one side of the target using a fine tip soldering iron, and subsequently, the target was bonded onto an indium coated Cu backing plate on a hotplate at ~200 °C. The bonded assembly was allowed to slowly cool to room temperature, and any excess indium on the sides was sanded off. After bonding, the assembly was screwed into the RF and DC guns in the sputtering chamber.

2.1.2 Thin Film Deposition: High Pressure Oxygen Sputtering

Reactive sputtering is a widely used and easily scalable physical vapor deposition (PVD) technique, where the bombardment of high-energy ionized molecules of a reactive gas mixture (typically Ar + O_2/N_2/H_2S) onto a target material results in both atomization and chemical reaction (oxidation/nitridation/sulfidation). A high electric potential, established between the target (cathode) and a substrate (anode), is required to ionize the gas mixture and sustain the plasma. Under the applied potential the ionized gas molecules (positively charged) accelerate rapidly towards the target (negatively charged); the subsequent momentum transfer results in the ejection of target atoms that react with the reactive component of the gas mixture before reaching the substrate. The relative simplicity of design, tolerance to variation in target composition, and scalability to large area targets and substrates makes reactive sputtering especially attractive for high volume device manufacturing. Conventional reactive sputtering of metal oxide thin films is carried out using an Ar/O_2 gas mixture in the 10 – 200 mTorr pressure range. In this pressure range, however, a large number of energetic oxygen anions are generated, which accelerate towards the substrate (anode) and cause re-sputtering of cations from the deposited film. This effective etching process results in severe cation non-stoichiometry and formation of

holes in the film [104, 105]. Re-sputtering can be avoided to some extent by reduction of O_2 partial pressure in the gas mixture or by switching to an off-axis sputtering mode in which the substrate is placed outside of the main path of the sputtered beam. But, the former results in oxygen non-stoichiometry and the latter in the reduction of deposition rate.

To mitigate the aforementioned challenges associated with conventional oxygen sputtering, we employed a relatively less common high-pressure oxygen sputtering technique for the growth of epitaxial BSO films. This technique uses high purity O_2 (~ 1 Torr) to generate the plasma for sputtering in an on-axis geometry. The high oxygen pressure not only near-eliminates re-sputtering by thermalizing the oxygen anions before they reach the substrate, but also leads to better oxygenation of the films. Furthermore, the on-axis geometry yields workable deposition rates for a wide variety of oxides. This high pressure oxygen sputter deposition technique was originally developed at the Forschungzentrum Jülich by U. Poppe and others to deposit high quality epitaxial films of $YBa_2Cu_3O_7$ with superior film microstructure and superconducting T_C, without the need for post-growth high temperature annealing in O_2 [106, 107]. The method has since been used for the deposition of a wide range of other functional oxide thin films, including ferromagnetic $(La,Sr)MnO_3$ [108] and $(La,Sr)CoO_3$ [87, 108], ferroelectric $BaTiO_3$ [109], multiferroic $BiMnO_3$ [110], and $SrTiO_3$ [111].

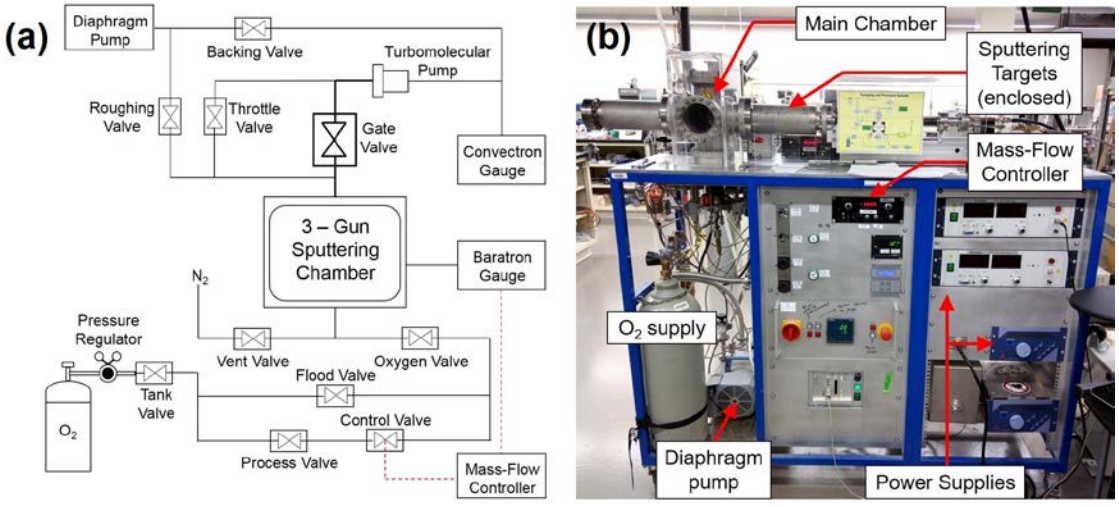

Fig. 2.1: (a) Schematic pumping diagram and (b) photograph of the high-pressure oxygen sputtering system.

A schematic pumping diagram of the high pressure oxygen sputtering chamber used for deposition of BSO epitaxial films in this study is shown in Fig. 2.1(a). A chamber base pressure of ~1 x 10^{-6} Torr was achieved in this system with an Agilent V-81 M turbomolecular pump (TMP) backed by a Vacuubrand MD 4 NT diaphragm pump. This diaphragm pump was also used as the roughing pump for the chamber. The chamber base pressure was measured using an Oerlikon Leybold IONIVAC ITR-90 ion gauge, whereas the TMP backing pressure was monitored using a Kurt J. Lesker Convectron® gauge. The entire pumping system is oil-free and compatible with the use of 99.998% purity research grade oxygen (Matheson Tri-Gas, Inc.) as the discharge gas. During deposition, with the main VAT gate valve closed and the TMP pumping through a 1/8" high impedance stainless steel line, the O_2 pressure inside the chamber was maintained at 1.5 – 2.3 Torr. This gas pressure was measured by an MKS Baratron® Type 626 capacitive manometer and the gas flow was regulated by an MKS 248A flow control valve controlled by an MKS Type 250 pressure/flow controller. Pure dry N_2 served as the vent gas during loading and unloading of samples.

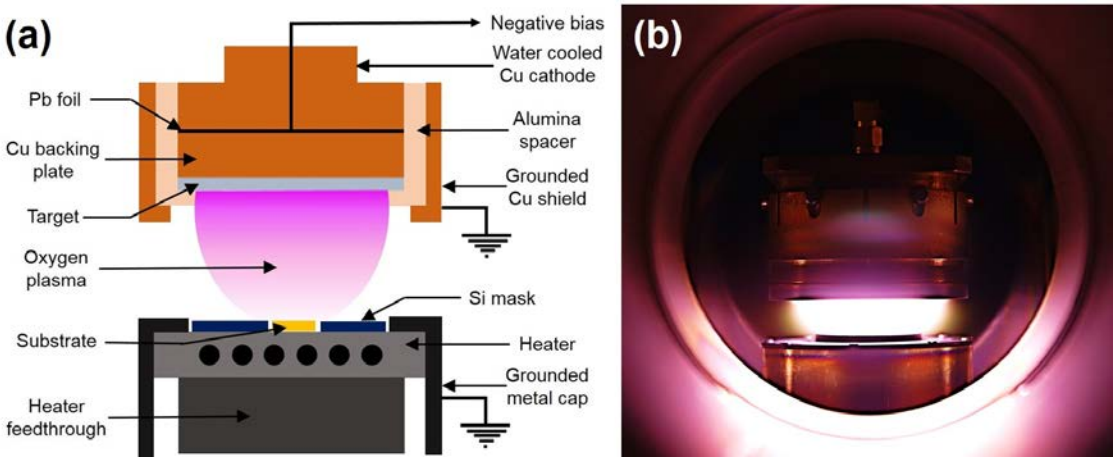

Fig. 2.2: (a) Schematic diagram of a DC sputter gun and the substrate heater assembly. (b) Photograph showing the oxygen plasma during deposition, and the DC sputter gun and substrate heater assembly.

A photograph of the deposition system highlighting some of the key features is presented in Fig. 2.1(b). The main chamber is a stainless steel enclosure in the shape of a spherical cube having six ports: the top port is used for loading/unloading samples; the four side ports are used for the TMP, the target transfer arm, and two serve as quartz viewports; the bottom port is used for the substrate heater feedthrough. The target transfer arm houses three sputter guns that can be connected to DC and RF power supplies. Fig. 2.2(a) shows a schematic of a DC sputter gun and the substrate heater assembly. The general features of both the DC and RF sputter guns are quite similar. The 2" BSO target was bonded to a Cu backing plate (as discussed in Sec. 2.1.1), which was then screwed onto the water-cooled Cu cathode. A thin Pb foil was placed in between to ensure conformal electrical and thermal contact. An insulating alumina spacer isolated the cathode from the outer grounded Cu shield and ensured that the plasma was confined only to the target. A Heinzinger PNC 600 – 300 neg high-precision switched mode DC power supply (600 V, 300 mA max.) and a TRUMPF Hüttinger PFG 300 RF generator were used to provide the negative biases during DC and RF sputtering, respectively. The chamber is equipped with a cylindrical heater block capped by a high temperature stainless steel plate. A Kanthal® (Sandvik GmbH) FeCrAl alloy strip meandering around the block functions as the resistance heating element. A Ni/NiCr thermocouple is also embedded in the block. The heater temperature was controlled by a Eurotherm 2404 temperature controller during deposition. The substrates were simply placed on the stainless steel plate. A Si frame (mask) was placed surrounding the substrates in order to prevent deposition of sputtered elements on to the heater surface during growth. Fig. 2.2(b) shows a picture of the DC oxygen plasma, and the sputter gun and heater assembly. Both the gun and heater assembly were cooled by flowing water at 20 – 21 °C. With no rotation of the substrate platform possible, the

substrates were placed as close to the center of the radially symmetric plasma as possible to reduce lateral thickness variations in the deposited films.

2.1.2.1 *Sputtering Procedure*

Although undoped and La-doped BSO films were deposited with different experimental conditions, a consistent procedure was employed before and after growth. Newly installed target had to be *extensively* "pre-sputtered" (~24 hrs.) with the target transfer arm fully retracted away from the substrate heater. This was done to ensure the removal of potential contaminants and adsorbed species on the surface of a new target. When the targets were deemed ready for film growth, substrates and the Si mask were loaded, and the chamber was subsequently pumped for 3 – 4 hrs. to reach a base pressure of ~1 x 10^{-6} Torr. After this the VAT gate valve was closed, and 0.5 – 1.2 Torr of flowing O_2 was introduced (pumped by the TMP through the 1/8" bypass line). Prior to growth, the substrates were annealed for 15 mins. at 900 °C to remove any organic surface contamination [111]. To ignite the RF plasma, the power of the RF generator was raised slowly (~0.2 W/sec.) from 0 W to a critical value ~15 W at a constant O_2 pressure of 1.2 Torr. The power and O_2 pressure were then increased in steps up to the desired growth condition. The target was then pre-sputtered away from the heater until the DC-bias value indicated in the power supply leveled off, suggesting a stable plasma. A similar procedure was followed for DC sputtering. First, the current was raised to 18 mA (with limiting voltage of 0 V) at 0.5 Torr O_2. Then, the limiting voltage was slowly (~1 V/sec.) increased until the plasma ignition was achieved at ~400 V. After this, the current (now limiting) and O_2 pressure were slowly raised at ~1 mA/sec. and ~0.1 Torr/sec. up to the growth condition, and then the target was allowed to pre-sputter until the indicated voltage value leveled off. Finally, to initiate growth the target transfer arm was brought over the heater *via*. a software interface. After growth, the following sequence was followed: the transfer arm was fully retracted, the plasma was slowly shut down, the bypass valve was closed, the chamber was flooded with 600 Torr of O_2, and the heating cycle was turned off. Upon reaching ambient temperatures, the chamber was vented with dry N_2 and the samples were removed.

2.1.2.2 *Choice of Substrates: The Mismatch Problem*

The substrates used for BSO thin film growth were commercial $LaAlO_3$(001), $SrTiO_3$(001), $GdScO_3$(001), $PrScO_3$(001), and MgO(001) single crystals (5 x 5 x 0.5 mm^3, single side polished), procured from CrysTec GmbH. A schematic diagram showing the various commercial substrates around the 4.116 Å BSO lattice parameter can be found in Fig. 2.3. The absence of any commercial substrate material within 2% mismatch with BSO is noteworthy. As a result, the thin films grown on these highly mismatched substrates have a very small critical thickness for strain relaxation, and BSO films relax readily, forming misfit and threading dislocations [112]. The impact of these dislocations on the structure and electronic properties of the films will be discussed in detail in the following chapters. Prior to loading in the chamber, each substrate was blown with a high velocity dry N_2 stream. No solvent cleaning was used as this often leaves unwanted organic residue on the surface.

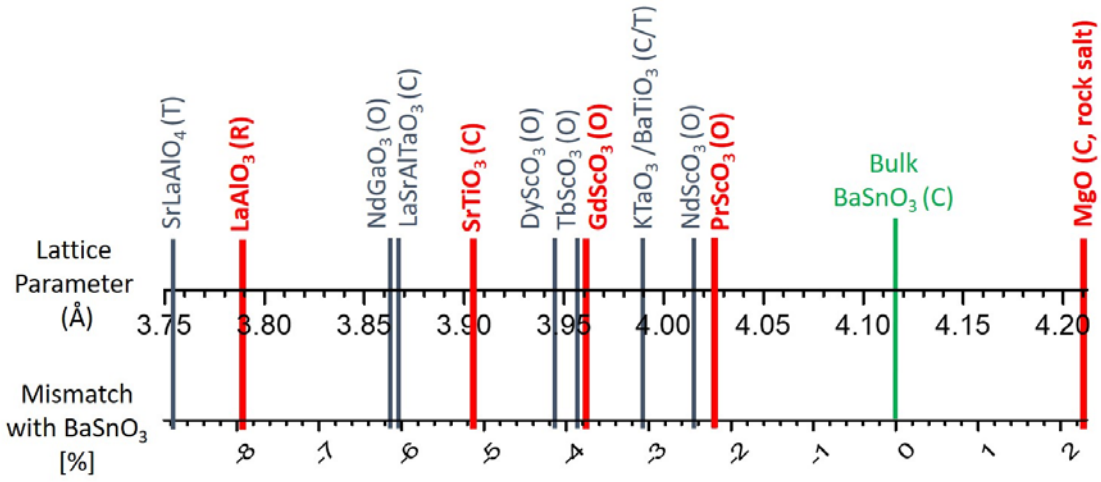

Fig. 2.3: Schematic diagram showing the bulk lattice parameter of commercial substrates along with their mismatch with BSO. The substrates highlighted in red are used in this study. Notes: lattice parameters are cubic or pseudocubic where applicable; symbols C, O, T, and R denote cubic, orthorhombic, tetragonal, and rhombohedral symmetry; all crystals are perovskites, with the exception of MgO.

2.2 Structural Characterization

The following section details the various experimental techniques used to characterize the structural properties of BSO polycrystalline powders, sputtering targets, and thin films. Powders and targets were characterized using X-ray powder diffraction (Sec. 2.2.1.2), scanning electron microscopy equipped with energy dispersive spectroscopy (Sec. 2.2.3), and particle-induced X-ray emission (Sec. 2.2.4). Structural properties of thin films, on the other hand, were probed using various modes of X-ray diffraction (Sec. 2.2.1.3 and 2.2.1.4), atomic force microscopy (Sec. 2.2.2), and scanning transmission electron microscopy (Sec. 2.2.5).

2.2.1 X-Ray Diffraction

X-Ray diffraction (XRD) is an analytical technique widely used for structural phase identification, high-precision lattice parameter measurement, strain analysis, texture analysis, and grain size estimation [113-115]. This technique is based on the constructive interference between X-rays, of wavelength (λ) $\approx$ 0.1 – 10 Å, elastically scattered from a set of periodically arranged atomic planes with interplanar spacing (d_{hkl}) similar to the λ of the incident X-rays [115]. The necessary criterion for diffraction, the Bragg condition, states that the constructive interference can *only* occur at a specific angle of incidence (the Bragg angle, θ_B) between the incoming wave and the normal ($\boldsymbol{n}_{\mathbf{hkl}}$) to the diffracting plane. Moreover, the diffracted wave vector ($\boldsymbol{k}$) is required to be coplanar with the incident wave vector ($\boldsymbol{k}_{\mathbf{i}}$) and $\boldsymbol{n}_{\mathbf{hkl}}$. In the most commonly used specular XRD setup, by rotating the sample and detector with respect to the incident X-ray beam, *i.e.*, changing angles θ and 2θ, respectively, while maintaining $\theta = \frac{1}{2}(2\theta)$, a plot of intensity *vs.* 2θ is obtained. While the Bragg condition only defines a specific diffracting angle ($2\theta_B$), the actual intensities of the peaks in the XRD pattern are determined by the scattering factors of each atom in the unit cell of the crystal.

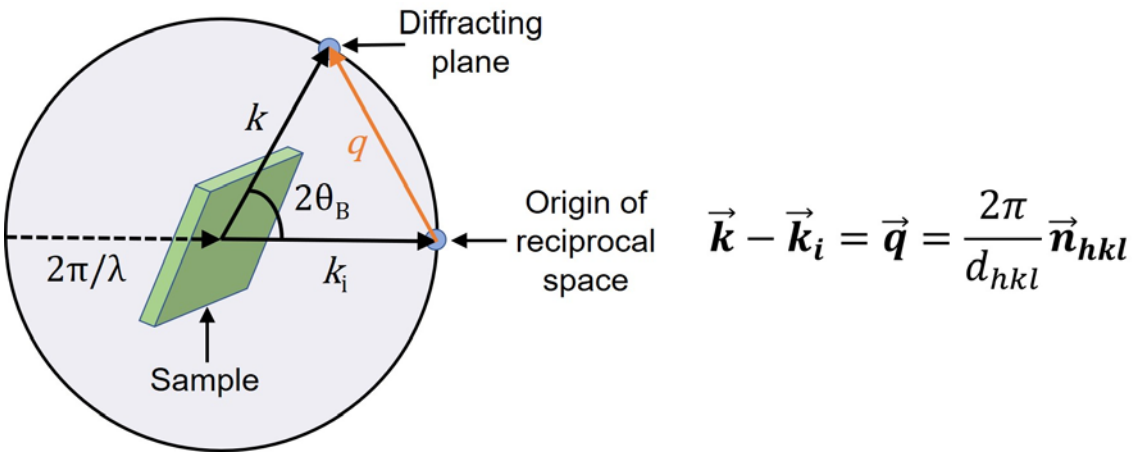

Fig. 2.4: Illustration of the Bragg condition for diffraction in reciprocal space.

It is often useful to analyze diffraction experiments in reciprocal space (or momentum space), which is simply a Fourier transform of the real space [116]. In reciprocal space, each family of crystalline planes is represented as a point, and the electromagnetic wave by a wave vector, $\boldsymbol{k}$, with magnitude $2\pi/\lambda$, pointing along the propagation direction. After undergoing *elastic* scattering, the X-ray wave exits the sample at an angle 2θ with respect to the incident beam. So, the incident and scattered wave vectors ($\boldsymbol{k}_i$ and $\boldsymbol{k}$, respectively) have the same magnitude and differ only in direction. The difference between these two vectors ($\boldsymbol{k} - \boldsymbol{k}_i$) is termed as the scattering vector, $\boldsymbol{q}$. Simple geometry yields:

$$|\vec{q}| = \frac{4\pi}{\lambda} sin\,\theta \qquad (2.1).$$

In reciprocal space, the Bragg condition then states that diffraction occurs only when $\boldsymbol{q}$ is equal to the reciprocal lattice vector for the diffracting plane (*hkl*), as depicted in Fig. 2.4.

2.2.1.1 *X-Ray Diffraction Setup*

The most simplistic XRD setup requires an X-ray source, a sample goniometer, and an X-ray detector. The X-rays are generated in a cathode ray tube when an electron beam, produced by heating a filament (typically W), strikes a metal target (Cu, Fe, Co, *etc*.). The high energy electron beam knocks out core-shell electrons from the target atoms, which subsequently relax back by emitting characteristic X-rays of fixed wavelengths. In addition to the characteristic lines, the deceleration of the electron beam caused by the target atomic nuclei produces a continuous broad spectrum of radiation, also known as *Bremsstrahlung*. Wavelength filtering and beam conditioning are required to generate a tightly focused beam with narrow wavelength dispersion and angular divergence. Although typical lab scale X-ray diffractometers are operated in the kW range with a fixed wavelength, higher intensities and variable wavelengths are achievable in particle accelerator based synchrotron sources. The sample goniometer consists of a set of calibrated motors that provide very accurate translation and rotation of the sample. The two most commonly used lab scale X-ray detectors are scintillation detectors and gas proportional counters. In scintillation detectors, the X-ray photons first collide with a phosphor screen (scintillator) producing photons in the blue region of the visible spectra, which are subsequently converted into voltage pulses by a photomultiplier tube attached directly behind the scintillator. In gas proportional counters, X-ray photons are used to ionize a gas, such as Ar or Xe, and the electrons of the ion pair are subsequently accelerated by a large voltage towards an anode wire to create a voltage pulse.

2.2.1.2 *Powder Diffraction*

Powder diffraction is an XRD technique optimized specifically for polycrystalline samples, in which the random crystallographic orientation of grains allows for observation of diffraction patterns very close to those theoretically predicted for each individual plane. Phase identification and compositional analysis are then carried out by comparing the experimental diffraction patterns with those of known materials. Most powder

diffractometers use the Bragg-Brentano geometry, shown in Fig. 2.5(a), in which $\boldsymbol{q}$ is perpendicular to the sample surface (specular scan), and the sample and detector are rotated in a coupled fashion with θ = ½ (2θ). In addition to phase compositional analysis, powder XRD can also yield information about the lattice parameter, grain size, and microstrain.

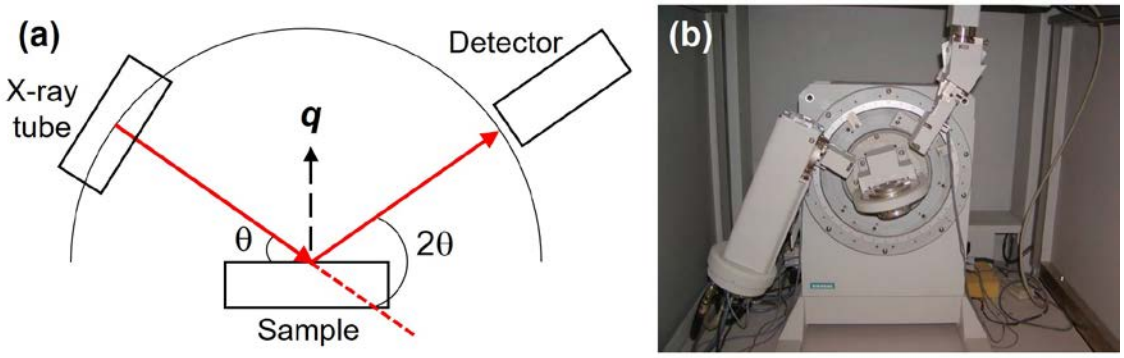

Fig. 2.5: (a) A schematic diagram illustrating the Bragg-Brentano geometry common in X-ray powder diffractometers. (b) A photo of the Bruker-AXS D5005 diffractometer used in this study.

In this study, a Bruker-AXS D5005 (picture shown in Fig. 2.5(b)) and a Rigaku Miniflex-600 were used to analyze the phase-purity and lattice parameter of BSO polycrystalline powders and bulk ceramic targets. Cu *K*α X-rays, with λ = 1.54 Å, were used in all the experiments. A Ni filter was used to filter out the Cu *K*β component, and additional slits were used to collimate the incident and diffracted beams. Samples were scanned in a wide range in 2θ, typically 20 – 130°, and the resulting diffraction patterns were analyzed by comparison to the ICDD database. One such diffraction pattern is presented in Fig. 2.6(a), with the various peaks labeled with the corresponding phases. Data of the type shown in Fig. 2.6(a) were also used to used to calculate the bulk lattice parameter (*a*) for cubic BSO using:

$$a = \frac{\lambda\sqrt{h^2 + k^2 + l^2}}{2\,sin\,\theta_B} \quad (2.2).$$

Here, *h*, *k*, and *l* are the Miller indices of the plane corresponding to the diffraction peak. Using Eq. (2.2), *a* was determined from each of the observed peaks and plotted *vs*. $\cos^2\theta_B/\sin\theta_B$ (Fig. 2.6(b)). This was done to minimize systematic errors in the estimation due to height and sample depth effects. The most accurate value of the lattice parameter was then extracted from the *y*-axis intercept of a linear fit through the data.

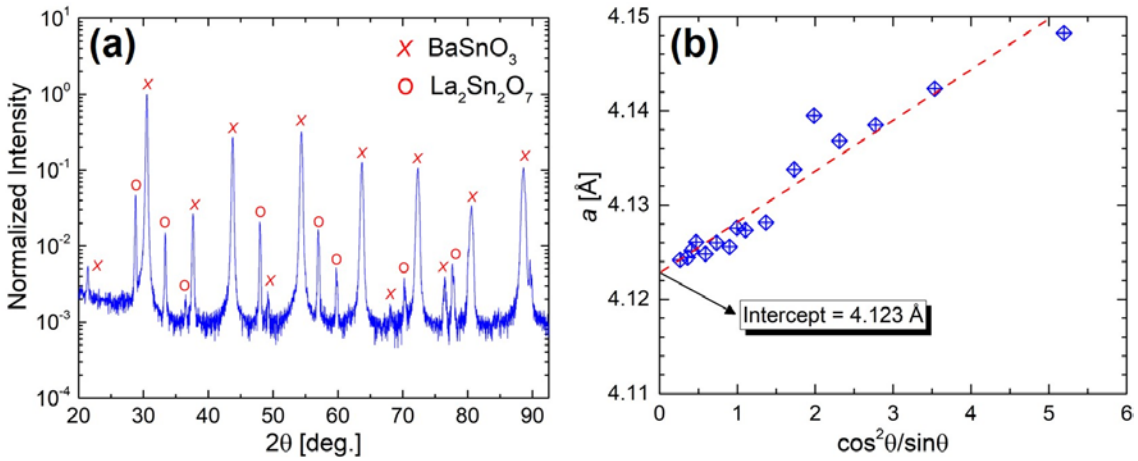

Fig. 2.6: (a) Powder diffraction scan of a 10% La-doped BSO pellet. Symbols *X* and *O* mark the peak positions corresponding to primary cubic $BaSnO_3$ and secondary pyrochlore $La_2Sn_2O_7$ phases. (b) Estimation of bulk lattice parameter from the powder diffraction in (a).

2.2.1.3 *High Resolution X-Ray Diffraction*

Although the simple and robust technique of powder XRD (described in Sec. 2.2.1.2) is often sufficient for phase identification and structural refinement, it is susceptible to measurement errors stemming from the angular and spectral divergence of the X-ray beam. In single crystals and epitaxial thin films, precise measurements of lattice parameters, strain, and mosaicity require the use of high-resolution XRD (HRXRD), where modifications and additions are made to the diffractometer to reduce the aforementioned measurement errors. Divergence and Soller slits are employed for beam collimation, reducing the angular divergence, while single crystal monochromators are used to

minimize the spectral divergence. Furthermore, the goniometer cradle is accurately calibrated for precise sample alignment with respect to the X-ray beam. The improved resolution, however, comes at a cost of reduction in beam intensity.

All HRXRD data discussed in this work were collected on a PANalytical X'Pert Pro MRD (Fig. 2.7(a)), a high resolution diffractometer equipped with a 1.8 kW Cu X-ray tube source. The motorized sample stage in this instrument is mounted on a ½ circle Eulerian goniometer cradle, enabling sample translations along the *x*, *y*, and *z* directions and tilts ψ, ω, and φ, as shown in Fig. 2.7(b). Using 1/2° divergence slits and a hybrid 4-bounce Ge(220) monochromator, a parallel beam of Cu $K\alpha_1$ radiation with $\lambda = 1.54059$ Å and angular spread (combination of both angular and spectral divergence) of ~0.0039° was obtained [117]. X-ray photon detection was done by a gas proportional counter based on a Xe/CH_4 gas mixture. The BSO films were mounted onto the sample holder using double-sided tape and carefully aligned by optimization of the substrate 002 peak intensity. The various modes of HRXRD used in this work include wide-angle XRD (WAXRD), rocking curve (RC), and symmetric specular and asymmetric non-specular reciprocal space mapping (RSM).

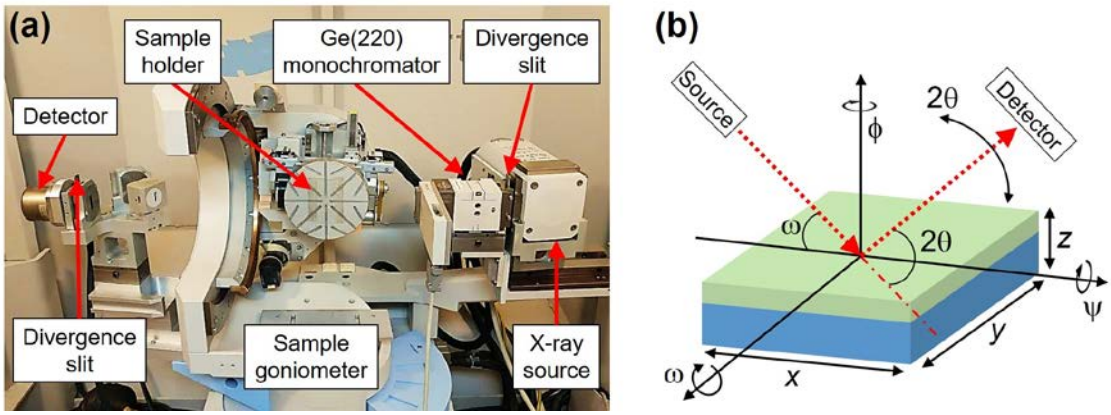

Fig. 2.7: (a) The PANalytical X'Pert Pro MRD used for the HRXRD measurements with the major components labeled. (b) Schematic depicting the various degrees of freedom available for sample positioning and measurement.

Specular WAXRD coupled scans performed in a continuous mode with a sweep rate of 0.005°/s, were used to extract the out-of-plane lattice parameter, a_{op}, and Scherrer length, Λ, of the sputtered BSO films. The a_{op} depends on the 002 film peak position only and can reveal information regarding the cation stoichiometry and strain in the films. The Λ, on the other hand, is given by:

$$\Lambda \approx \frac{0.9\,\lambda}{\beta\, cos\, \theta_{002}} \qquad (2.3).$$

Here, θ_{002} is one-half of the 002 peak position, and β (in radians) is the full-width-at-half-maxima (FWHM) of the 002 peak. Hence, it is related to the broadening of the Bragg peak as a result of the film's finite size (in the absence of microstrain) along the out-of-plane direction. One such WAXRD scan is shown in Fig. 2.8(a) for a 300-Å-thick undoped BSO film deposited on $GdScO_3$(001). The a_{op} extracted is slightly expanded compared to the bulk value of 4.116 Å, and can be a result of slight cation non-stoichiometry or residual strain in the film. It can also be noted that Λ closely matches the film thickness, *t*, deduced from the periodicity of the *Kiessig fringes* around the film peak, suggesting negligible microstrain. The observation of Kiessig fringes around the film Bragg peak is a result of the mutual interference of X-rays that are reflected from the film surface and the film/substrate interface [118, 119]. The two set of reflected beams alternatively interfere with each other constructively and destructively giving rise to fringes around the Bragg peak. The periodicity of Kiessig fringes is a function of the film thickness, while their amplitude is dependent on the scattering length density (SLD) difference between the film and the substrate. Other factors affecting these fringes include interface and surface roughness, X-ray coherence length, and thickness fluctuations over the probed area.

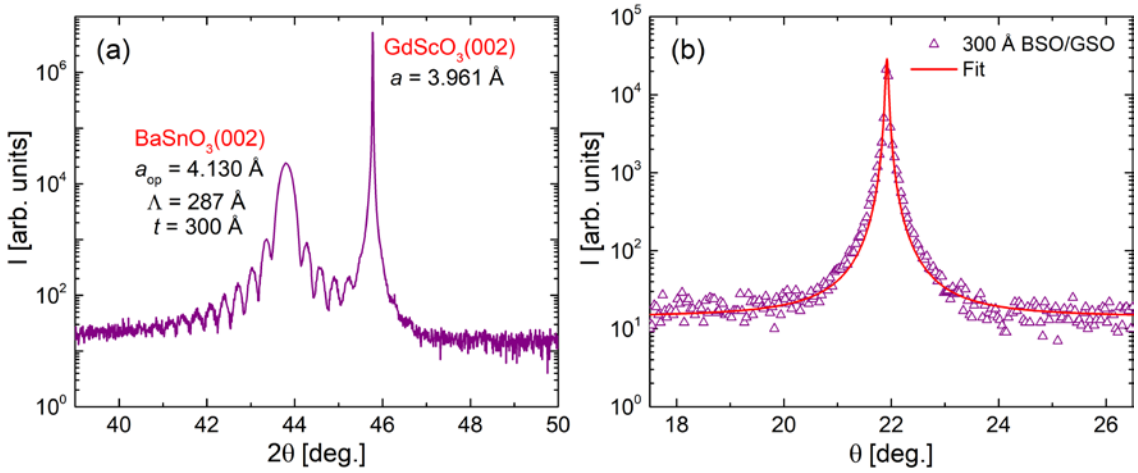

Fig. 2.8: (a) High-resolution WAXRD around the (002) reflections, and (b) 002 RC for a 300-Å-thick undoped BSO film deposited on a $GdScO_3$(001) substrate. Useful structural parameters extracted from the scans are included.

In addition to WAXRD coupled scans discussed above, rocking curve (RC) scans are often performed to characterize epitaxial thin films and single crystals. In an ideal crystal with perfectly parallel lattice planes, the Bragg diffraction condition is met *only* when ***q*** is *exactly* perpendicular to the planes, as shown in Fig. 2.9(a). However, in reality, crystals are comprised of microcrystallites that are slightly misaligned with respect to each other (Fig. 2.9(b)) resulting in a small mosaic spread [115]. In this case, the Bragg condition is satisfied over a range of angles of ***q***, and therefore, an RC scan, performed by varying ω while keeping 2θ constant, can be used to probe the extent of mosaicity in "non-ideal" films. Such scans can not only be used to quantify the mosaic spread, but also to study strain relaxation in epitaxial thin films. An example RC scan through the 002 film peak is shown in Fig. 2.8(b) for a 300-Å-thick undoped BSO film deposited on $GdScO_3$(001).

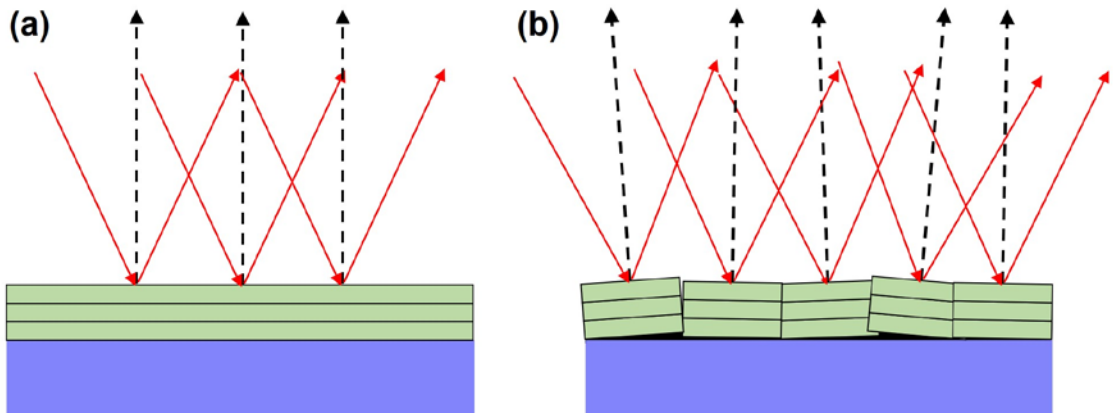

Fig. 2.9: Schematic of (a) an ideal single crystal thin film on a substrate with perfectly parallel lattice planes, and (b) a real crystal thin film with finite mosaicity. The dashed black lines denote the direction of the $\boldsymbol{n_{hkl}}$ for each microcrystallite. Bragg condition is only satisfied when $\boldsymbol{q}$ is parallel to $\boldsymbol{n_{hkl}}$ for each microcrystallite.

The HRXRD modes discussed so far are only sensitive to the lattice planes along the out of plane direction. To extract useful structural information along the in-plane direction a very powerful two-dimensional (2D) technique, called *reciprocal space mapping*, is often employed that allows simultaneous visualization of the out-of-plane and in-plane relationship between the film and the substrate. As the name suggests, this scan maps out a 2D region of the reciprocal space containing both the film and substrate Bragg peaks (Fig. 2.10(a)). The procedure involves the continuous sweeping of $\boldsymbol{q}$ to change both its magnitude and direction and is accomplished by carrying out a series of 2θ-ω coupled scans at different offsets, Δ, defined by:

$$\Delta = \omega - \frac{1}{2}(2\theta) \tag{2.4}$$

RSMs performed with Δ = 0 are called symmetric specular RSMs, whereas, RSMs with finite Δs are termed as asymmetric non-specular RSMs. Each combination of 2θ-ω

uniquely maps to a point in the reciprocal space, and can be subsequently converted into reciprocal lattice units (q_x and q_y) as follows:

$$q_x = \frac{2\pi}{\lambda} [\cos\omega - \cos(2\theta - \omega)] \tag{2.5}$$

$$q_y = \frac{2\pi}{\lambda} [\sin\omega + \sin(2\theta - \omega)] \tag{2.6}.$$

Reciprocal space contour maps were subsequently generated by plotting q_x and q_y *vs.* detected intensity and used to estimate the in-plane lattice parameter of the films. The RSMs discussed in this work were acquired on the PANalytical X'Pert Pro using the same basic setup as that of WAXRD and RC, but with 1/4° slits. An example non-specular RSM around the (013) peaks is shown in Fig. 2.10(b) for a 2% La-doped BSO film grown on a $PrScO_3$(001) substrate.

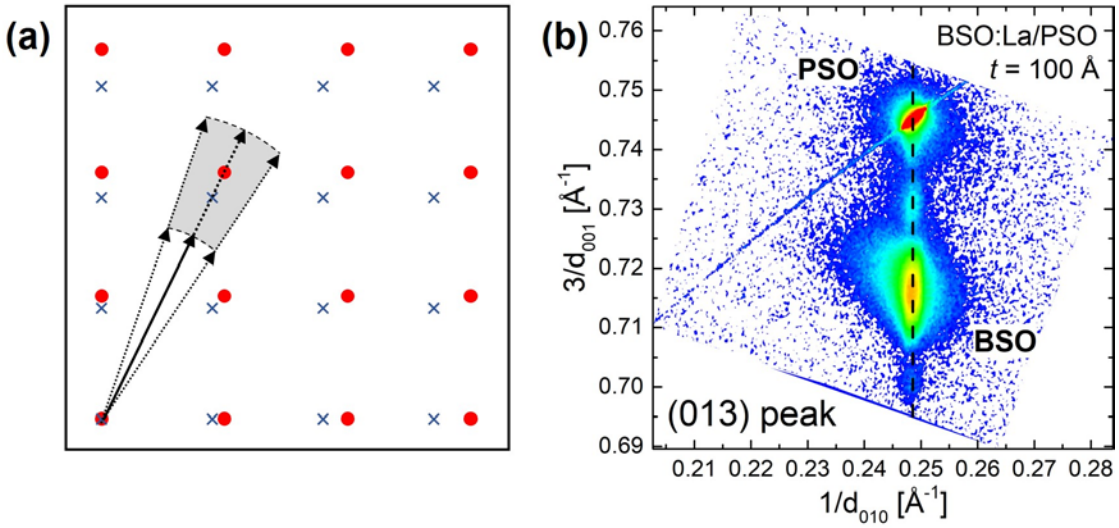

Fig. 2.10: (a) Reciprocal space depiction of a strain-relaxed epitaxial film (blue cross) and a single crystal substrate (red dot) superimposed on each other. The shaded area marks the area mapped out by the RSM measurement around the (013) reflections. (b) An RSM showing a fully strained $Ba_{0.98}La_{0.02}SnO_3$ film on a $PrScO_3$(001) substrate.

2.2.1.4 *Grazing Incidence X-Ray Reflectivity and In-Plane Diffraction*

Grazing incidence X-ray reflectivity (GIXR) is a powerful surface sensitive technique that can be used to probe layer thickness, interface roughness and density of thin films. It is based on the interference of X-rays that are reflected from the film/air and film/substrate interfaces. GIXR experiments can be performed under both specular and non-specular conditions, and use X-rays that are incident on the sample at very shallow angles (< 10°). The refractive index, *n*, of a material is given by:

$$n = 1 - \delta - i\beta \tag{2.7}$$

Here, δ and β are the dispersion and absorption coefficients, respectively. For the X-ray wavelengths used in the experiments, *n* is slightly less than 1. Hence, X-rays experience *total external reflection* at the material surface when the angle of incidence is below a critical angle, θ_c, given by Snell's law:

$$\theta_c = cos^{-1}(1 - \delta) \tag{2.8}$$

When the incident angle exceeds θ_c, part of the beam penetrates into the sample and part of it is reflected, with the reflected beam intensity falling off sharply following the laws of *Fresnel reflectivity* ($R \propto q^{-4}$). In the case of a film deposited on a substrate, X-rays are reflected from both the film/air and film/substrate interfaces. The alternative constructive and destructive interference of these two reflected beams gives rise to Kiessig fringes, which are superimposed on top of the Fresnel reflectivity. The condition for the i^{th} constructive interference is given by:

$$\sin^2\theta_i - \sin^2\theta_c = i^2\frac{\lambda^2}{4t^2} \tag{2.9}$$

Here, *t* denotes the film thickness. The position of the Kiessig fringes can hence be used to accurately determine the film thickness. GIXR of a representative thin film and its thickness estimation using the periodicity of the Kiessig fringes are shown in Fig. 2.11(a) and (b). This procedure of thickness calculation, however, is not sensitive to the interface roughnesses and material density. These effects can be incorporated by the use of software packages like GenX to refine the GIXR data [120]. All GIXR measurements in this study were conducted on the X'Pert Pro diffractometer using slightly different beam optics compared to HRXRD. The hybrid monochromator was replaced by a parabolic mirror module without any monochromator, the divergence slit was reduced to 1/32°, and the triple axis detector module was replaced by a 0.27° parallel plate collimator equipped with a 0.1° slit.

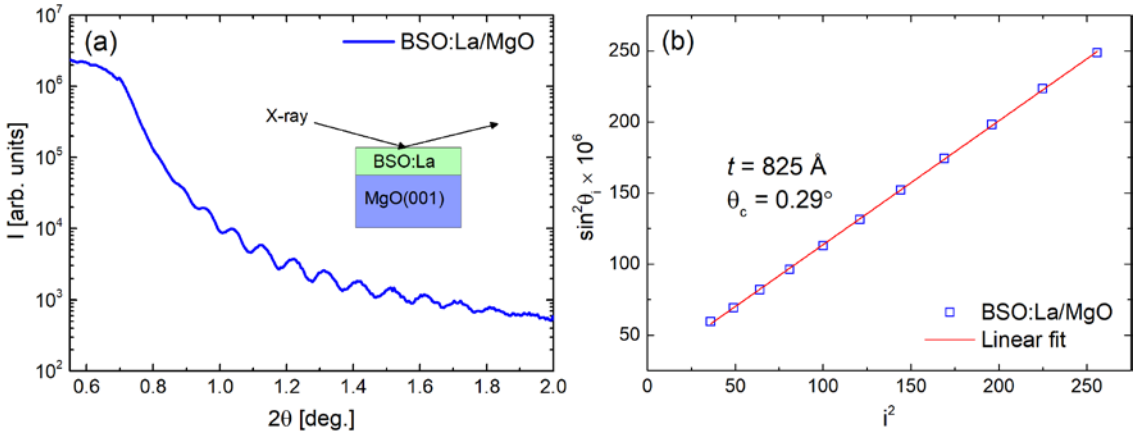

Fig. 2.11: Representative GIXR data of a 2% La-doped BSO film grown on MgO(001) substrate, taken from the present study, showing clear Kiessig fringes. (b) A graph demonstrating the procedure of film thickness calculation based on the periodicity of the Kiessig fringes.

In addition to GIXR, grazing incidence in-plane X-ray diffraction (GIIXD) is another surface sensitive technique that exploits the limited depth penetration of X-rays undergoing total external reflection. As shown in Fig. 2.12, when the sample is oriented in a way that allows specular Bragg diffraction from a crystal plane having only in-plane

components, a strong diffracted beam emerges at the same exact grazing angle as the incident beam. In this orientation, WAXRD and RC measurements can yield information about in-plane lattice parameters, crystallite size, and mosaicity. It is, however, important to note that the Bragg condition is never truly satisfied as ***q*** does not point perfectly along the plane of the sample. In-plane diffraction results discussed in this work were all obtained on the X'Pert Pro. The X-ray source was configured to a point focus mode, with a cross-slit collimator placed in front of the X-ray lens to generate a line focus in the plane of the slightly tilted sample. The 0.27° parallel plate collimator was used on the diffracted beam side.

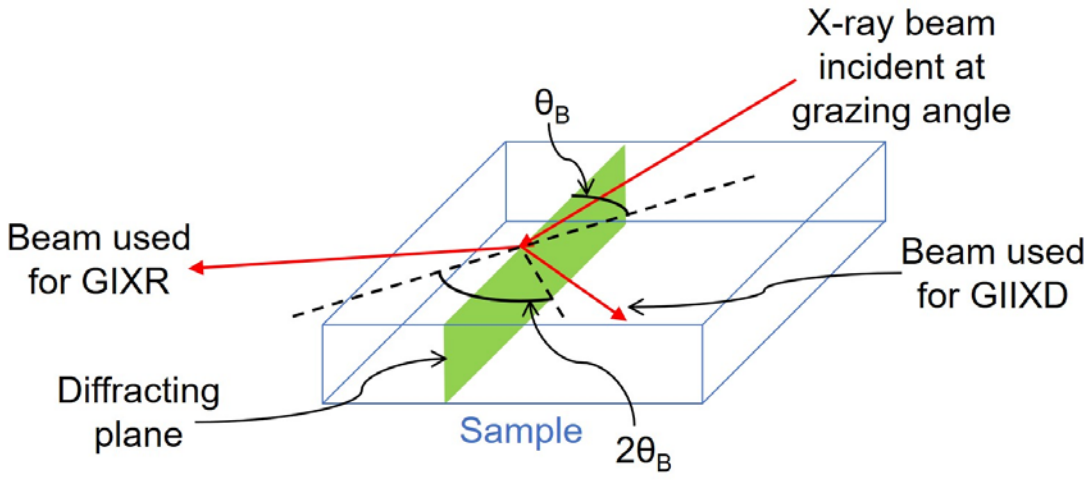

Fig. 2.12: Schematic diagram of the grazing incidence geometry, showing the incident, diffracted (GIIXD), and specularly reflected (GIXR) beams.

2.2.2 Atomic Force Microscopy

Atomic force microscopy (AFM) is a widely employed scanning probe technique used to obtain quantitative information about the surface topography. AFM involves rastering a nanometer scale tip, positioned at the end of a cantilever, across the sample surface at very close range. Changes in the local forces between the atoms of the tip and the surface results in deflections of the cantilever. These deflections are accurately measured and analyzed in real time to generate the topographic map of the sample surface.

The interaction between two atoms is well described by the Lennard-Jones potential, which combines a long-range attraction ($\propto r^{-6}$) and a relatively short-range repulsion ($\propto r^{-12}$), *r* being the separation between the atoms. AFM exploits this sensitive dependence of the interactive force with *r* to maintain the tip at a precise distance from the sample.

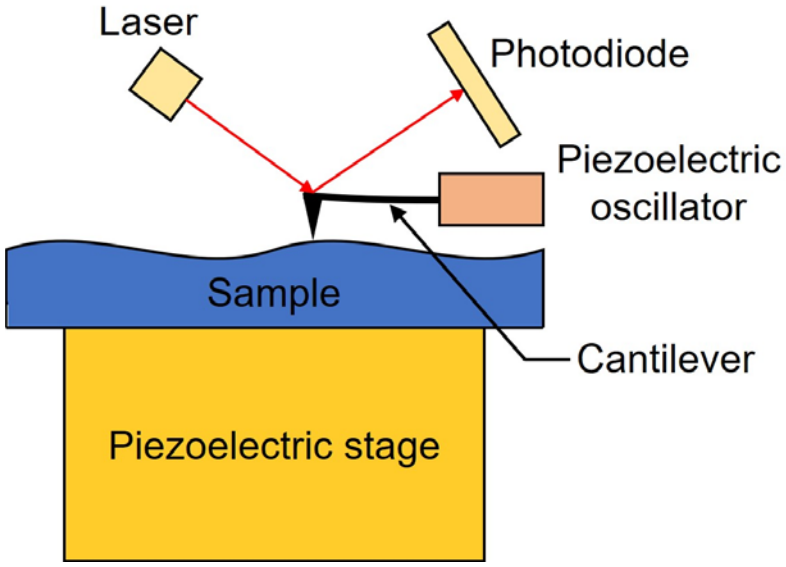

Fig. 2.13: Schematic showing the basic elements of an AFM system.

As shown in Fig. 2.13, the sample is mounted on a piezoelectric stage capable of precise high resolution vertical and lateral movements. The nanometer sharp scanning tip is positioned at the end of a cantilever. A solid-state laser is focused to a spot on the end of the cantilever, and the reflected beam is detected by a four-quadrant position sensitive detector (PSD). During the scan, deflections of the cantilever are detected by changes in the laser spot on the PSD, which is then fed back to the piezo stage through a PID controller. In contact mode AFM, the controller enables the cantilever to always maintain a constant deflection, or in other words, a constant height above the sample surface by adjusting the *z* position of the stage. The adjustments in the *z* position of the piezo stage are recorded during the rastering process to finally yield a two-dimensional map of the sample topography, called the height image. In this study, contact mode AFM images of BSO thin films were acquired with a Bruker Nanoscope V over an area of 4 x 4 μm^2.

2.2.3 Scanning Electron Microscopy

Scanning electron microscopy (SEM) is a characterization technique that uses high energy electrons (0.3 – 30 keV), allowing much greater spatial resolutions compared optical microscopy, to image the surface of a material [121]. Electrons are first generated from a cathode filament, either by thermionic or field emission, and then accelerated towards an anode. Using a series of condenser and objective lenses, the electrons are positioned and focused onto a sample. Energy transfer between the electrons and the atoms in the sample results in the emission of characteristic and continuum X-rays, cathodoluminescence, and release of secondary, Auger, and backscattered electrons. Low energy (< 50 eV) secondary electrons (SEs), released from atoms close to the surface (~10 Å), are used to image the surface morphology. The number of SEs detected by a scintillation detector has a strong dependence on the topographical features of the sample [121].

SEM images were taken with a JEOL-6010PLUS/LA scanning electron microscope equipped with a W-based thermionic emission source (0.5 – 20 kV), SE detector, backscatter electron (BE) detector, and energy dispersive analysis of X-rays (EDAX) detector. At 20 kV excitation voltage, a lateral spatial resolution of ~40 Å could be obtained. Samples were mounted on a brass sample holder using Carbon-tape. Fig. 2.14 shows a representative SEM image of a sintered La-doped BSO pellet collected at 5 kx magnification, using a 20 kV accelerating voltage and 10 mm working distance.

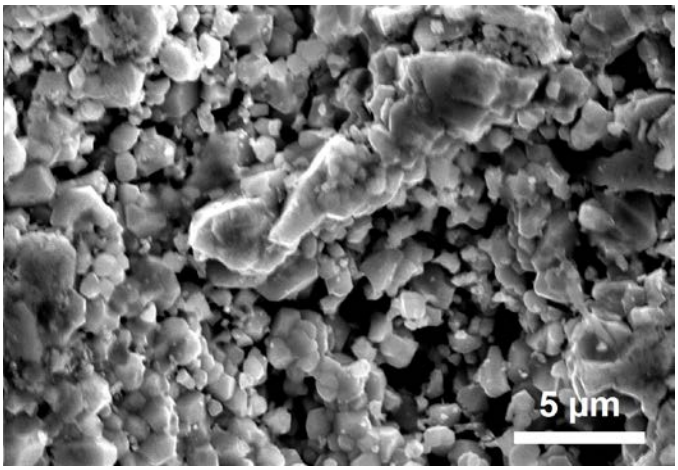

Fig. 2.14: A representative SEM image (5 kx magnification) of a 2% La-doped BSO sintered ceramic pellet.

As discussed above, in addition to the generation of SEs, a significant amount of characteristic X-rays are also generated when accelerating electrons interact with the sample. The high energy electrons can 'knock' core electrons from the atoms in the sample. These atoms can subsequently relax from their excited states by releasing energy in the form of X-ray radiation. The energy of the emitted X-ray photon is characteristic of the element, and measurement of this energy can be used to reveal information about the elemental makeup of the sample. This technique is known as energy dispersive spectroscopy (EDS). EDS was used in the present study to perform elemental composition analysis of undoped and La-doped BSO sputtering targets. The measurement accuracy was estimated to be ~0.75%. A Nd-doped BSO single crystal of known composition was used as a "standard" for all the EDS measurements discussed in this work.

2.2.4 Particle-Induced X-ray Emission

Like EDS, Particle-induced X-ray Emission (PIXE) is another energy-dispersive analytical technique used to determine the elemental composition of a sample. Unlike EDS, however, this technique employs a high-energy beam of α-particles to generate characteristic X-rays from the atoms in the sample. In comparison to EDS, significantly reduced *Bremsstrahlung* results in much better peak-to-noise ratios, thus enabling detection and quantification of trace impurities. Although absolute sensitivity to a given trace element is dependent on factors like detector efficiency and peak overlap, a ~1 ppm level sensitivity is achievable. A schematic depicting the major components of the experimental setup used for PIXE is shown in Fig. 2.15(a), while representative data from a La-doped BSO pellet is shown in Fig. 2.15(b). A finely collimated beam of α-particles (4 MeV), produced by a MAS 1700 pelletron tandem ion accelerator, was directed towards the sample, resulting in a beam spot size of ~0.2 – 1 mm. The sample was mounted on a

stage attached to a goniometer capable of translational and rotational motion. An internal Faraday cup was used to suppress SE emission. X-Ray energy detection was accomplished using a Kevex retractable Si(Li) X-ray detector with a 5 mm Be-window and an energy resolution of 145 eV. An Al filter was placed in front of the detector to attenuate the dominant peaks and allow greater trace element sensitivity. The total charge dosage used in the experiments was 60 μC. An interactive software package, known as GUPIX, was used in the refinement of the raw data to yield elemental concentrations.

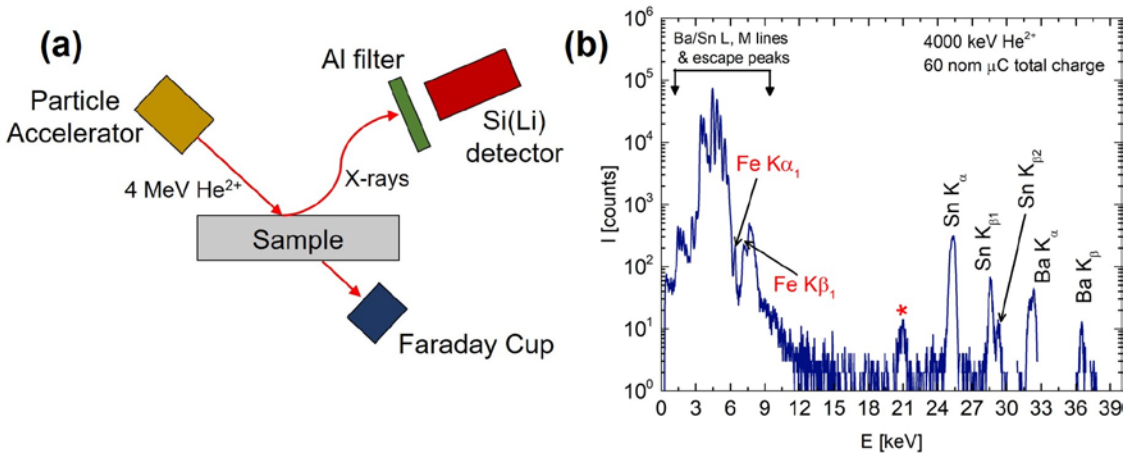

Fig. 2.15: (a) Schematic of the experimental setup for PIXE. (b) Representative PIXE data of a 2% La-doped BSO sintered ceramic pellet. The symbol * marks an unidentified peak.

2.2.5 Scanning Transmission Electron Microscopy

Transmission electron microscopy (TEM) is a high resolution imaging technique that involves analysis of high energy (~60 – 300 keV) electrons transmitted through an ultrathin sample (< 1000 Å). The high energy of the electron beam, in combination with aberration correction, allows imaging with sub-angstrom spatial resolution. Scanning transmission electron microscopy (STEM) is a specialized sub-category of TEM, where the electron beam is first focused to a narrow spot (~0.5 – 2 Å) and then rastered across the sample [122]. Fig. 2.16 shows a schematic of the electron column in a typical STEM. Electrons, generated by a high brightness source, are accelerated down the column,

collimated by a set of condenser lenses and apertures, corrected for aberration, and finally focused on to the sample by a set of objective lenses and apertures. A set of scan coils in the column help to control the position of the beam on the sample and raster the beam across the sample. After interacting with the sample, the transmitted beam is simultaneously detected by a variety of detectors. A bright-field (BF) detector, placed directly in the path of the transmitted beam, detects electrons undergoing minimal scattering from the sample. A complementary mode, known as annular dark-field (ADF) imaging, involves the detection of electrons undergoing elastic scattering (sensitive to atomic number, *Z*) by an annular detector placed outside the angular cone of the transmitted beam.

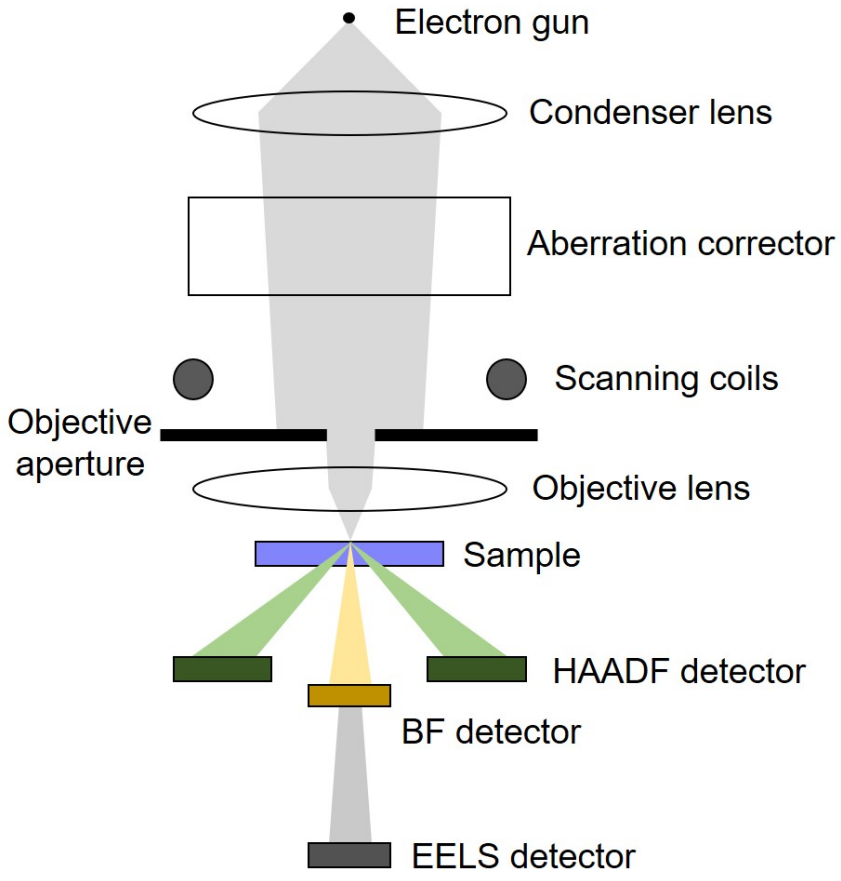

Fig. 2.16: Schematic of the electron column in a typical STEM showing the various components.

The STEM characterization of $BaSnO_3$ thin films was performed by Hwanhui Yun in Prof. Andre Mkhoyan's group in Chemical Engineering and Materials Science. Cross-sectional transmission electron microscopy samples were prepared using a FEI Helios Nanolab G4 dual-beam focused ion beam (FIB), where the samples were thinned using a 30 kV Ga-ion beam and further polished using a 2 kV Ga-ion beam to eliminate damaged layers at the surface. The thickness of the cross-sectional samples was in the range of 400 – 500 Å. Plan-view TEM samples were prepared by mechanical polishing using Multiprep™ (Allied High Tech Products, Inc.). The plan-view sample thickness was estimated to be in the range of 500 – 700 Å *via* the electron energy-loss spectroscopy (EELS) log-ratio method using a calculated mean free path of plasmon excitation in BSO of λ_p = 810 Å [64, 123]. Scanning transmission electron microscope (STEM) imaging was carried out using an aberration-corrected FEI Titan G2 60-300 STEM at 200 keV with ~30 pA beam current. The convergent semi-angle of the incident STEM probe was 17.2 mrad and the ADF detector inner angles were 19 mrad, 55 mrad, and 93 mrad for low-angle ADF (LAADF), medium-angle ADF (MAADF), and high-angle ADF (HAADF) images, respectively.

2.3 Electronic Transport Characterization

Electronic properties of doped BSO thin films and bulk targets were evaluated through temperature (*T*) and magnetic field (*H*) dependent measurements of key parameters such as resistivity (ρ), electron density (*n*), and electron mobility (μ) utilizing a widely used van der Pauw geometry [124, 125]. This is a versatile four terminal measurement technique where the current leads are separated from the voltage leads, thus negating the effect of contact resistance. It even works for arbitrarily shaped samples, provided the following requirements are met:

1. The sample is homogeneous and of uniform thickness
2. The contacts are on the circumference of the sample
3. The contact area does not exceed 10% of the sample area

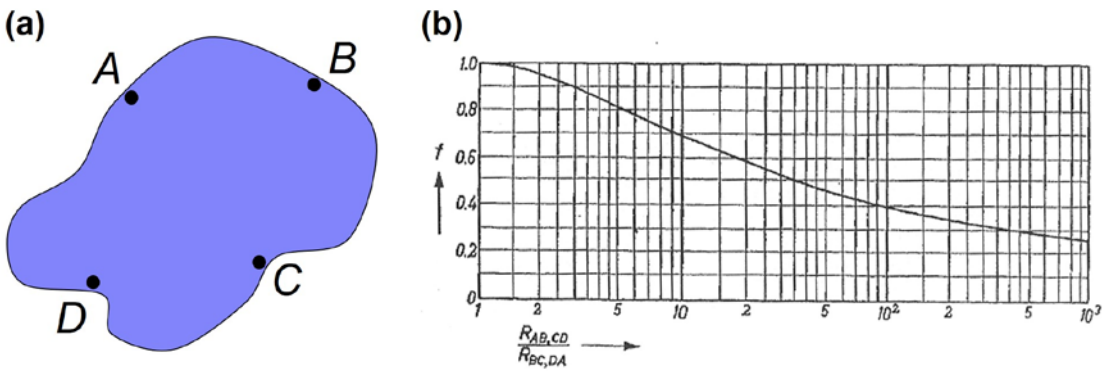

Fig. 2.17: (a) Schematic showing a lamellar sample with four electrical contacts arranged in a van der Pauw geometry. (b) The anisotropy factor, *f*, *vs*. the van der Pauw resistance ratio [125].

Fig. 2.17(a) shows an arbitrarily shaped sample with four electrical contacts *A*, *B*, *C*, and *D*. With all the above-mentioned conditions satisfied, the sample's ρ can be expressed as:

$$\rho = \frac{\pi t}{ln2} \frac{R_{AB,DC} + R_{AD,BC}}{2} f$$

(2.10).

Here, *t* is the sample thickness, *R* is a longitudinal four-terminal resistance for a specific current-voltage pair (the first and second pair of subscripts representing the current and voltage leads, respectively), and *f* is a factor that depends on the resistance ratio $\left(\frac{R_{AB,DC}}{R_{AD,BC}}\right)$, and satisfies the relationship,

$$\cosh\left\{\frac{\left(\frac{R_{AB,DC}}{R_{AD,BC}}\right) - 1}{\left(\frac{R_{AB,DC}}{R_{AD,BC}}\right) + 1} \frac{ln2}{f}\right\} = \frac{1}{2}\exp\left(\frac{ln2}{f}\right)$$

(2.11)

and is graphically represented in Fig. 2.17(b).

Fig. 2.18(a) shows a schematic diagram of the contact geometry used in this study in order to carry out electronic transport measurements. First, indium contacts were soldered on the four corners of the 5 x 5 mm^2 samples. Then the sample was attached to a sample holder using GE varnish, and gold wires were used to form connections between the In contacts on the sample and the contact pads in the holder (Fig. 2.18(b)). Finally, the holder was loaded into a He-cryostat for *T*- (1.8 – 300 K) and *H*- (0 – 9 T) dependent resistance measurements using both AC (Linea Research LR-700 resistance bridge) and DC (Keithley 220 current source and Keithley 2002 digital multimeter for measuring voltage) electronics. Two different He-cryostats built by Quantum Design, Inc, the Physical Property Measurement System (PPMS) Evercool II and PPMS Dynacool, were used to measure the samples discussed in this study. Both positive and negative current biases were used to nullify the effect of thermoelectric voltages. The bias current was chosen to minimize Joule heating, and Ohmic behavior of the contacts was verified down to the lowest *T*.

In the presence of a perpendicular magnetic field, transverse resistance (in a Hall geometry) was also measured along with longitudinal resistance (known as magnetoresistance). The Hall effect is based on the principle of Lorentz force, and the sign and magnitude of the slope of Hall resistance *vs*. field can be used to estimate majority carrier type and density (*n*) according to:

$$R_{xy} = R_H\, B\ ; \qquad R_H = -\frac{1}{e\, n_{2D}}\ ; \qquad n_{3D} = \frac{n_{2D}}{t}\ ; \qquad \mu = \frac{1}{e\, n_{3D}\, \rho}$$

(2.12).

Here, R_{xy} is the transverse resistance, R_H is the Hall coefficient, B is the magnetic flux density, and n_{2D} and n_{3D} are the two and three-dimensional electron density in the sample, respectively.

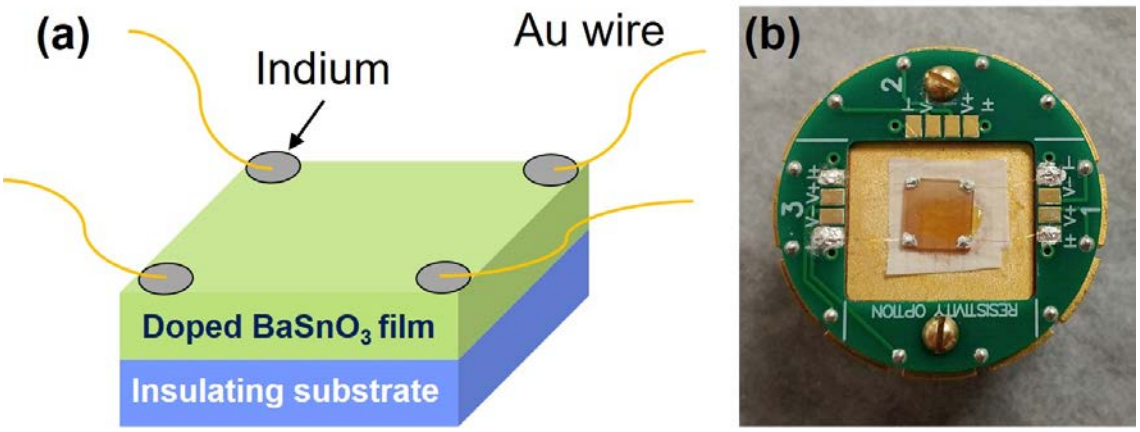

Fig. 2.18: (a) Schematic diagram of the contact geometry used for electronic property measurements of the films. (b) A photo of a BSO on $LaAlO_3$(001) substrate film mounted on the PPMS sample holder. Au wires connect the In contacts on the sample to the contact pads of the sample holder.

Chapter 3: Analysis of $Ba_{1-x}La_xSnO_3$ Polycrystalline Sputtering Targets

3.1 Introduction

As discussed in Sec. 2.1.1, polycrystalline BSO powders were synthesized by solid-state reaction, and subsequently cold-pressed and sintered into bulk sputtering targets. This chapter summarizes the structural and electrical (BSO:La only) characterizations performed on the various undoped and La-doped BSO ceramic targets.

3.2 Structural and Compositional Analysis of Undoped $BaSnO_3$ Targets

Undoped BSO pellets (0.5" diameter), produced following the outline in Sec. 2.1.1, represented the sputtering targets during characterization. Fig. 3.1(a) shows the powder XRD patterns for a batch of undoped BSO powders. By comparing this pattern with the known diffraction data for cubic $BaSnO_3$ (Fig. 3.1(c)) it becomes clear that although cubic $BaSnO_3$ is the primary phase, some additional peaks, ascribed to unreacted SnO_2, are still observed even after a total reaction time of 72 hrs. All XRD peaks corresponding to the SnO_2 secondary phase disappear, however, after sintering at 1400 °C as seen in Fig. 3.1(b). Note that in the standard XRD pattern for cubic $BaSnO_3$, the (410), (331), and (421) peaks are indicated by dashed lines because they were not listed in the databases, possibly due to very low intensities. Their expected peak positions were calculated using the 4.116 Å bulk lattice parameter for BSO. These peaks are included in Fig. 3.1(c) to provide an explanation for the peaks observed at similar 2θ values in the XRD patterns in Figs. 3.1(a) and (b). Following the procedure described in Sec. 2.2.1.2, the bulk lattice parameter, a_{target}, of the BSO powders and pellet were estimated from the diffraction data shown in Fig. 3.1. These were determined to be 4.117 Å for both the powders and pellet, which is in very good agreement with the literature value (4.116 Å) [47]. This suggests that the BSO pellet, and hence the corresponding sputtering target, was phase-pure and nominally stoichiometric (within the detection limits of powder XRD).

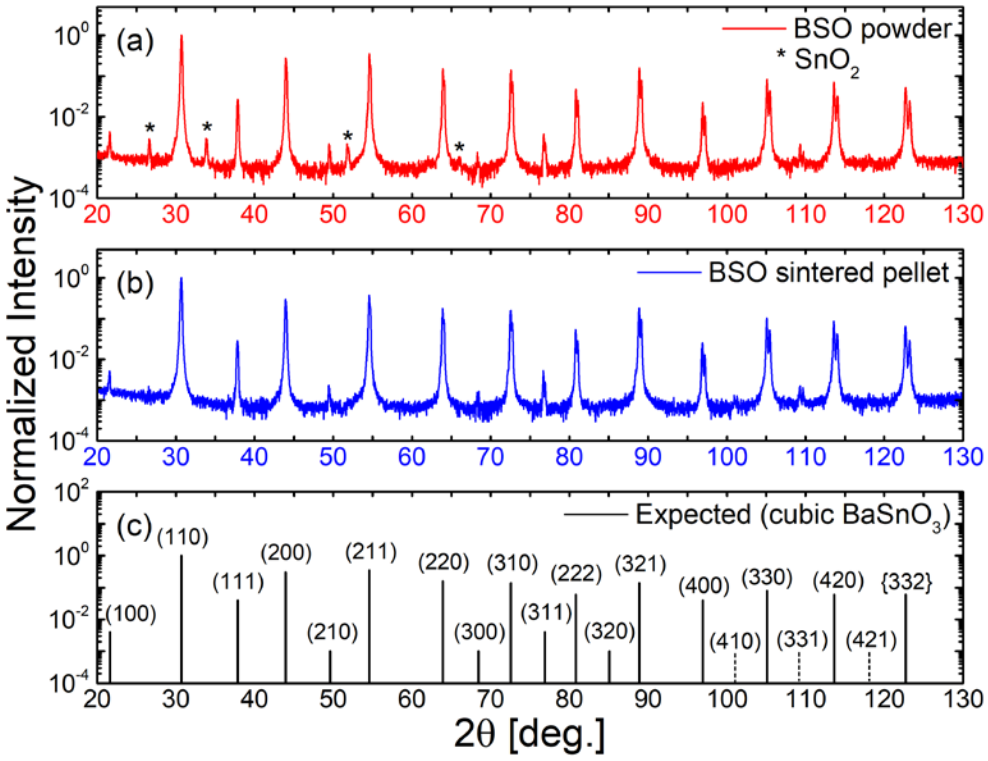

Fig. 3.1: (a) Powder XRD 2θ-ω coupled scans of (a) reacted undoped BSO powders, (b) the corresponding pellet after cold-pressing and sintering at 1400 °C. (c) Diffraction pattern expected for cubic $BaSnO_3$.

After verifying the phase-purity and stoichiometry of the undoped BSO pellet using XRD, EDS was performed in an SEM, operated at an excitation voltage of 20 kV and a working distance of 10 mm, to perform chemical compositional analysis from a sample area of ~0.05 mm^2. Fig. 3.2 shows the EDS spectrum of an undoped BSO sintered pellet. At energies below 0.5 keV, characteristic *K*α peaks of low *Z* elements C, N, and O are observed. C and N are ubiquitous and always present on the surface. In the 0.5 – 2 keV energy range, various peaks corresponding to Ba and Sn M lines can be seen along with the Al and Si *K*α peaks. The Si peak is a detector artifact, whereas the Al peak appears likely from the sample holder. The characteristic peaks observed at energies greater than 3 eV correspond to the *L*-series transitions in Ba and Sn. By analyzing the EDS peak area for each element, a Ba/Sn atomic ratio of 1.01 was obtained.

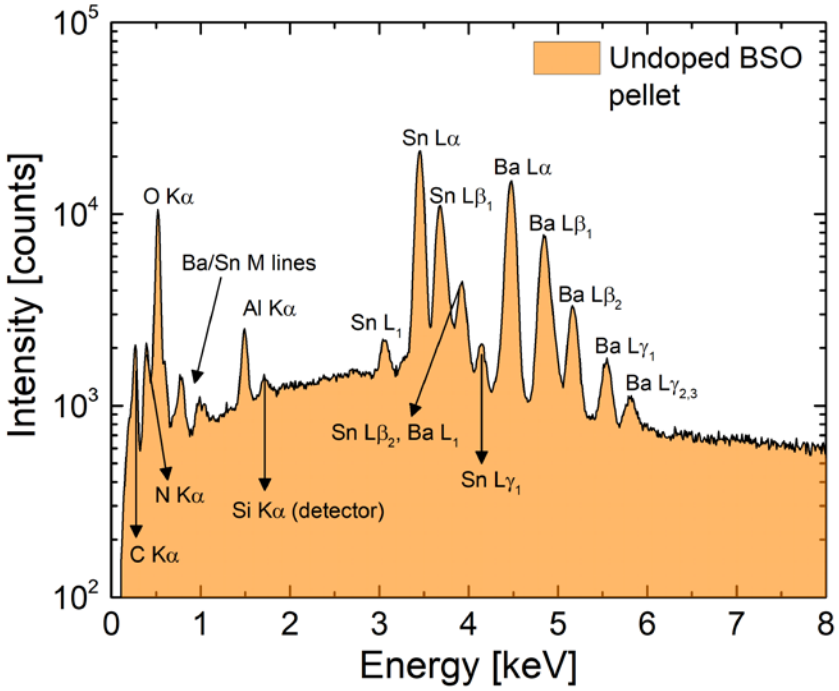

Fig. 3.2: EDS spectrum of an undoped BSO pellet. Peaks are corresponding to characteristic X-ray emissions are clearly labeled.

In conjunction with the EDS spectrum, secondary electron SEM micrographs of the undoped BSO pellet surface were also acquired. Fig. 3.3 shows two secondary electron images acquired at 5 kx (Fig. 3.3(a)) and 10 kx (Fig. 3.3(b)) magnification. It is clear that the pellet has a high degree of residual porosity (density < 70% of the theoretical value), and also shows large variations in particle size even after sintering at 1400 °C for 24 hrs.

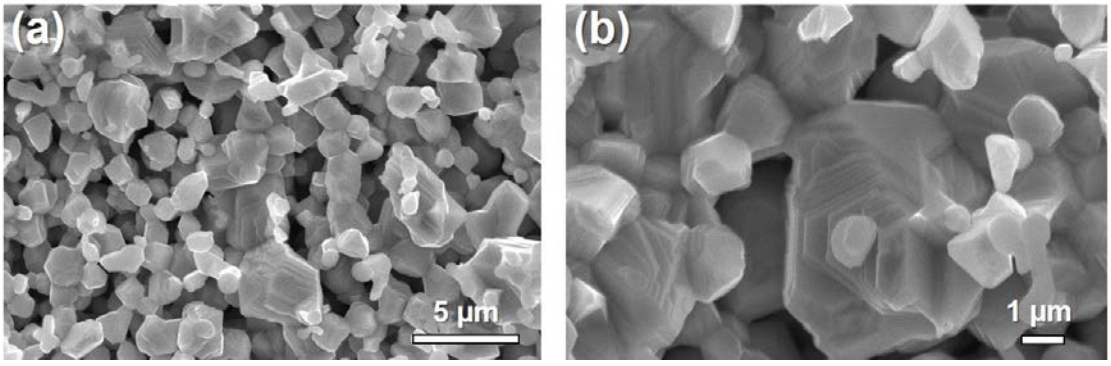

Fig. 3.3: Secondary electron SEM micrographs of the surface of an undoped BSO pellet sintered at 1400 °C. Images were captured at (a) 5 kx, and (b) 10 kx magnifications with 20 kV excitation voltage and 10 mm working distance.

3.3 Impact of La doping

In addition to undoped BSO sputtering targets, La-doped BSO (BSO:La) targets, with La doping concentration, *x*, varying between 0.002 – 0.1, were also produced following a similar procedure (Sec. 2.1.1). Fig. 3.4 shows the powder XRD scans for three pellets with $x = 0.002$ (Fig. 3.4(a)), 0.02 (Fig. 3.4(b)), and 0.1 (Fig. 3.4(c)). All pellets were sintered at 1450 °C for 24 hrs. The XRD patterns for the $x = 0.002$ and 0.02 pellets are nearly identical to that of the $x = 0$ pellet in Fig. 3.1(b), and agree very well with the expected pattern for cubic $BaSnO_3$. However, for the $x = 0.1$ pellet, an additional pyrochlore $La_2Sn_2O_7$ secondary phase was observed along with the $BaSnO_3$ primary phase. The appearance of this second phase is not unexpected given the low solubility of La in BSO, previously determined to be < 5% in bulk [46, 63].

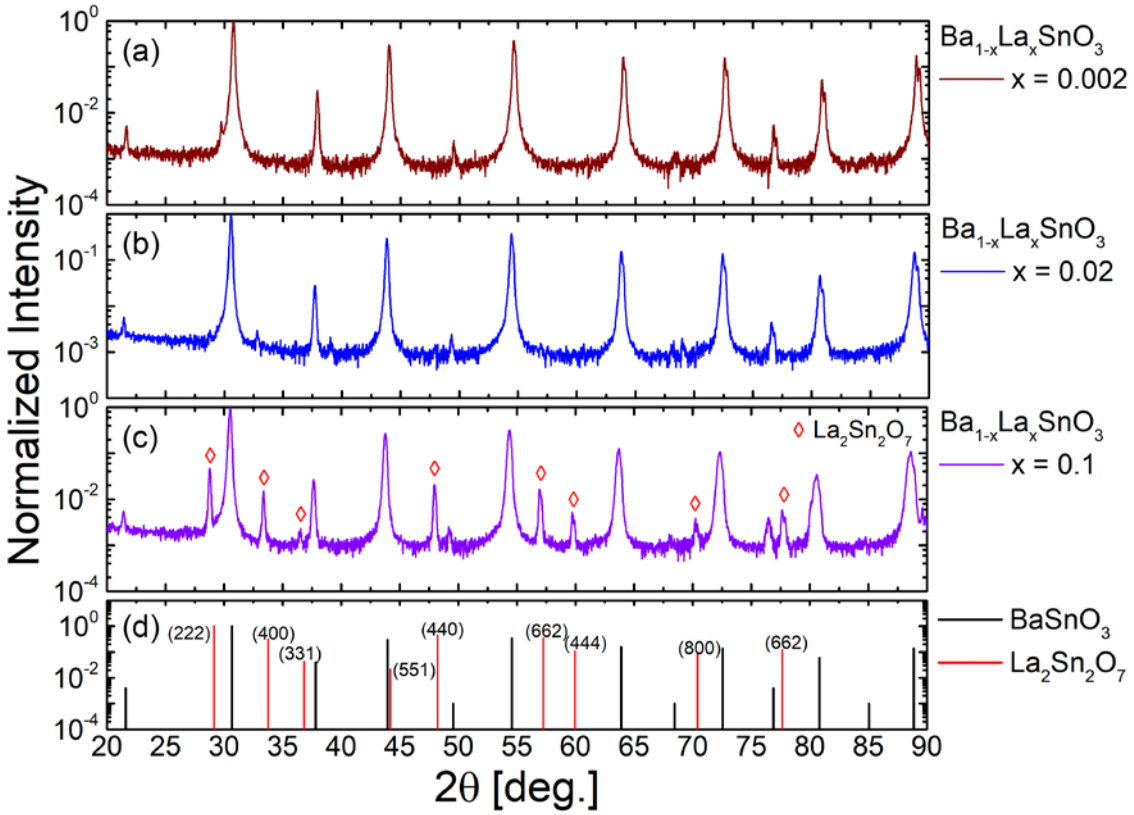

Fig. 3.4: Powder XRD 2θ-ω coupled scans of BSO:La sintered pellets with varying La doping concentrations, *x*. (a) *x* = 0.002, (b) *x* = 0.02, and (c) *x* = 0.1. (d) Diffraction patterns expected for cubic $BaSnO_3$ and pyrochlore $La_2Sn_2O_7$.

Fig. 3.5 shows the experimentally determined lattice parameter, a_{target}, for BSO:La (x = 0 – 0.1) sintered pellets plotted *vs*. *x*. Note that the error bars only express the uncertainty in the linear regression used in the determination of a_{target}, and do not reflect the instrument error. The general increasing trend (from 4.117 – 4.123 Å) with *x* is consistent with other findings in the literature [46, 47]. EDS was also performed on the pellets in order to experimentally estimate *x*. The analysis revealed La concentration to be 0.03 and 0.14 for the *x* = 0.02 and 0.1 BSO:La pellets. Finally, electrical resistivities (ρ) of the sintered pellets were measured in a van der Pauw geometry at 300 K. The undoped BSO pellet had an unmeasurably high ρ. With increasing La doping, however, ρ dropped several orders of magnitude to ~8 kΩcm for *x* = 0.002, and further down to ~10 Ωcm for *x*

= 0.02, finally increasing to ~30 Ωcm for the x = 0.1 pellet. The initial drop in ρ from x = 0 to x = 0.02 is most likely due to an increase in the electron density (n), while the unexpectedly high ρ for x = 0.1 is possibly due to the presence of the insulating $La_2Sn_2O_7$ secondary phase.

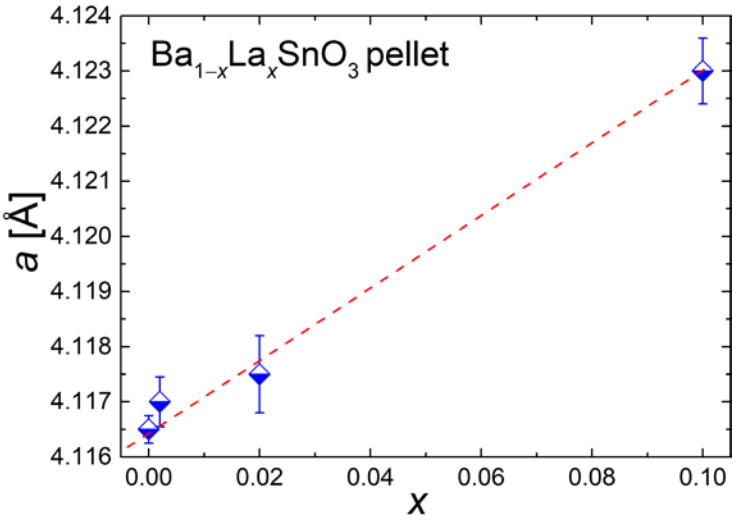

Fig. 3.5: BSO:La pellet lattice parameter plotted *vs*. x. The red dashed line is a guide to the eye.

3.4 Effect of Sintering Temperature

After investigating the effects of La doping in BSO sputtering targets, we studied the influence of sintering temperature, $T_{sintering}$, on their structural and electrical properties. Five BSO:La (x = .02) pellets were synthesized with $T_{sintering}$ varying between 1350 – 1550 °C. This, however, resulted in a corresponding variation in pellet density only between 60 – 70%. Fig. 3.6 shows the powder XRD scans for the reacted powders (for comparison) and the five sintered pellets. It is clear that as $T_{sintering}$ was increased, the peaks corresponding to the precursor oxides, BaO and SnO_2, progressively weakened in intensity, finally vanishing above $T_{sintering}$ = 1500 °C. This demonstrates the benefit of employing higher $T_{sintering}$ to achieve phase pure BSO targets.

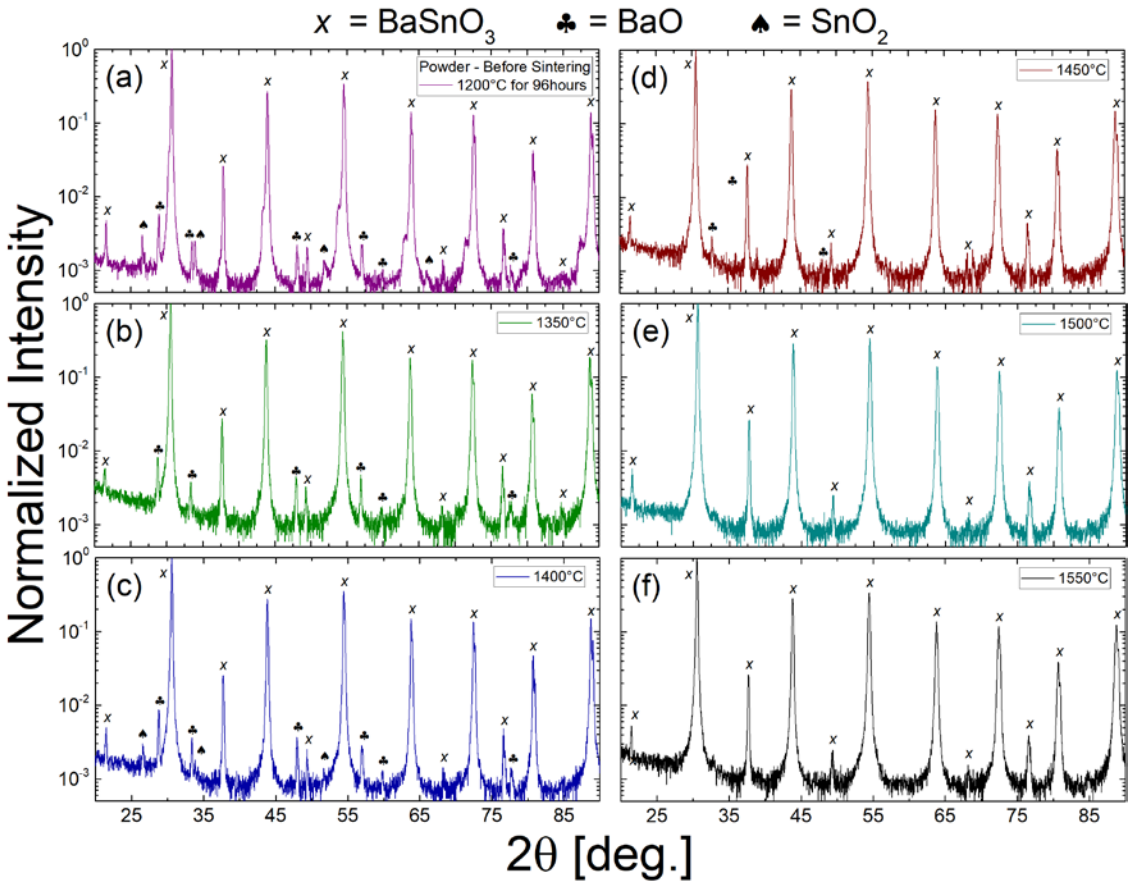

Fig. 3.6: Powder XRD 2θ-ω coupled scans for BSO:La (x = 0.02) (a) reacted powders, and five pellets sintered at $T_{sintering}$: (b) 1350 °C, (c) 1400 °C, (d) 1450 °C, (e) 1500 °C, and (f) 1550 °C. All diffraction peaks are marked by corresponding symbols (legend above plots).

The bulk lattice parameter, a_{target}, was estimated for each of the five pellets and is plotted *vs.* $T_{sintering}$ in Fig. 3.7(a). With the exception of 1550 °C, all other $T_{sintering}$s probed resulted in a_{target} values in good agreement with the literature. In the case of $T_{sintering}$ = 1550 °C, however, a slight expansion (< 0.003 Å) in a_{target} was observed. A possible explanation for this behavior could be related to the formation of cation vacancies resulting in a change in the overall stoichiometry during sintering at 1550 °C. To study this in greater detail, atomic Sn/Ba ratios were estimated in the pellets using EDS as shown in Fig. 3.7(b). Overall, the Sn/Ba ratio shows a decreasing trend with increasing $T_{sintering}$, suggesting a loss

of Sn at higher $T_{sintering}$. In addition to EDS, electrical measurements were also performed on the pellets at 300 K. Fig. 3.7(c) shows that ρ initially remains unchanged close to ~10 Ωcm up to $T_{sintering}$ = 1500 °C, and then increases to ~60 Ωcm for $T_{sintering}$ = 1550 °C. This increase can possibly arise from the loss of Sn, as inferred from EDS. Based on the structural and electrical results, 1450 °C was chosen to be the optimal $T_{sintering}$ for the synthesis of BSO:La targets to be used in the sputtering of thin films.

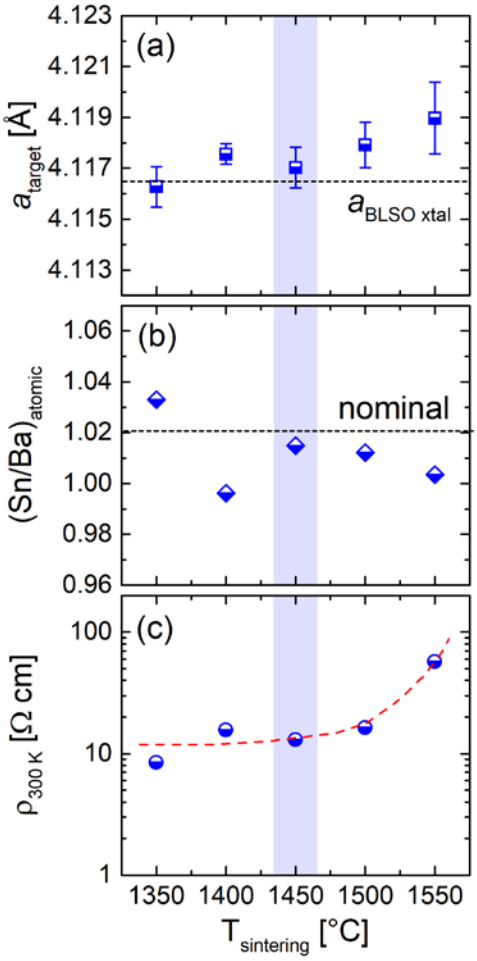

Fig. 3.7: Summary of structural and electrical properties of polycrystalline BSO:La (x = 0.02) targets. (a) Bulk lattice constant *vs*. target sintering temperature ($T_{sintering}$). The dashed line represents the literature value for the bulk lattice parameter of a 2% La-doped BSO single crystal [46, 47]. (b) Atomic Sn/Ba ratio evaluated *via* energy dispersive spectroscopy (EDS) *vs*. $T_{sintering}$. The dashed line represents the nominal Sn/Ba ratio for 2%

La_{Ba}, *i.e.* Sn/(Ba – La) = 1.02. (c) 300 K resistivity, $\rho_{300\ K}$, *vs*. $T_{sintering}$. The blue shaded regions in (a), (b), and (c) indicate the optimal $T_{sintering}$, determined to be 1450 °C.

3.5 Conclusions

In this chapter, we have demonstrated the ability to synthesize phase-pure polycrystalline undoped and La-doped BSO targets, with the exception of $x = 0.1$, where a $La_2Sn_2O_7$ secondary phase is observed. The bulk lattice parameter was shown to increase with increasing La dopant concentration. We also investigated the effects of sintering temperature on the structural and electrical properties of the targets. Above $T_{sintering}$ = 1500 °C, the observed expansion in the lattice parameter of the pellets was accompanied by a reduction in Sn/Ba atomic ratio estimated by EDS and an increase in resistivity. This was suggested to be due to an Sn loss at high $T_{sintering}$.

Chapter 4: Structure and Transport in High Pressure Oxygen Sputter-Deposited $BaSnO_{3-\delta}$

This chapter has been reprinted with permission from K. Ganguly, P. Ambwani, P. Xu, J.S. Jeong, K.A. Mkhoyan, C. Leighton, and B. Jalan, APL Materials **3**, 062509 (2015);

4.1 Chapter Overview

In this chapter, we report on a study of the growth, structure, and stoichiometry of epitaxial $BaSnO_3$ (BSO) deposited *via* high pressure oxygen sputter deposition. This is a proven method for oxides, where a high pressure (*O*(1 Torr)) O_2 plasma provides aggressive oxygenation, thermalized ions, and minimized resputtering. It is shown here to produce single-phase, relaxed, close to stoichiometric BSO, as characterized by high resolution X-ray diffraction (HRXRD), grazing incidence X-ray reflectivity (GIXR), grazing incidence in-plane X-ray diffraction (GIIXD), atomic force microscopy (AFM), and scanning transmission electron microscopy (STEM). This is demonstrated on both STO(001) and MgO(001), the latter providing smaller lattice mismatch (2.3% tensile *vs*. 5.4% compressive) but with symmetry mismatch. Significantly, vacuum annealing of 300-Å-thick films on MgO(001) at 850 °C is shown to readily reduce BSO, the resulting V_O density generating a Hall electron density of 5×10^{19} cm^{-3}, 6 mΩcm resistivity, and 20 $cm^2V^{-1}s^{-1}$ mobility. The transport is degenerate (in fact metallic) with a positive temperature coefficient of resistivity down to 100 K. While this mobility is lower than prior thin film reports with other dopants, there remain numerous promising routes to further mobility optimization.

4.2 Methods

RF sputter deposition was done from 2” undoped BSO targets synthesized by solid-state reaction of $BaCO_3$ and SnO_2 (99.9% purity) in air at 1200 °C, followed by cold-

pressing then sintering at 1400 °C. Prior to growth, the substrates were annealed for 15 min in 1.9 Torr of O_2 at 900 °C. Films were subsequently deposited at 76 W with 550 – 850 °C substrate temperatures (T_{dep}) and 1.5 – 2.2 Torr O_2 pressures (P_{O2}), the rate (0.4 – 1.5 Å/min) being controlled by the source-to-substrate distance. Post-growth cooling was done in 600 Torr of O_2. HRXRD (including wide-angle X-ray diffraction (WAXRD), rocking curves (RCs), and reciprocal space maps (RSMs)), GIIXD, GIXR were performed with Cu *K*α radiation in a Panalytical X'Pert system. GenX [126] was used for GIXR refinement. Contact mode AFM was carried out in a Bruker Nanoscope V Multimode 8, while cross-sectional high-angle annular dark-field (HAADF) STEM was performed on an aberration-corrected monochromated FEI Titan G2 60-300 at 300 kV. The semi-convergent angle of the incident beam was 24.5 mrad, HAADF images were obtained with a detector angle of 50 – 200 mrad and samples were tilted to a [100] zone axis. Vacuum annealing was done at 850 °C for 4 hrs. at pressures < 10^{-7} Torr. Subsequent electronic transport measurements (AC and DC, 2-300 K, 0 – 9 T) utilized indium contacts in a van der Pauw geometry.

4.3 Results and Discussion

4.3.1 Structure

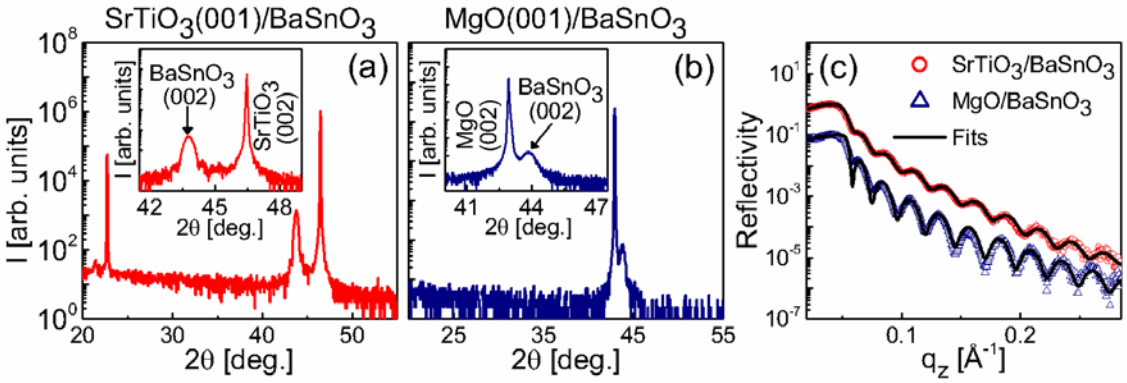

Fig. 4.1: Structural characterization of 230-Å-thick BSO films grown on STO(001) (red) and MgO(001) (blue) at 750 °C and 1.5 Torr O_2 pressure. High resolution WAXRD on (a) STO(001)/BSO, and (b) MgO(001)/BSO. Insets: Close-ups around the 002 film/substrate

peaks. (c) GIXR (reflectivity *vs*. scattering wavevector, q_z) for the same films (points) along with GenX fits (black solid lines). The curves are displaced for clarity. The refined film densities and surface roughnesses are 6.9 g cm^{-3} and 6.8 Å on STO(001), and 7.4 g cm^{-3} and 5.4 Å on MgO(001), respectively. The bulk density of BSO is 7.2 g cm^{-3}.

To illustrate the basic structural features of high pressure oxygen sputter-deposited BSO, WAXRD for 230-Å-thick films on STO(001) and MgO(001) is shown in Figs. 4.1(a) and (b). These films were deposited at 750 °C [127-129], in 1.5 Torr of O_2 (typical for this method). Figs. 4.1(a,b) reveal only the BSO, STO, and MgO 00*l* reflections, establishing phase purity (within detection limits), and out-of-plane epitaxy. As can be seen from the 002 close-ups in the insets to Figs. 4.1(a,b), finite-size fringes are observed on STO(001), but not on MgO(001), indicating that films on STO are smoother on short lateral length scales. As shown in Fig. 4.1(c), however, BSO films on both substrates are smooth on the long lateral scales probed in GIXR; the fits refine the film RMS (root-mean-square) surface roughnesses to 6.8 Å on STO and 5.4 Å on MgO, *i.e*. the 1 – 2 unit cell level. GIIXD (φ scan) for representative 300-Å-thick films on STO(001) and MgO(001) is shown in Figs. 4.2(a) and (b). The film and substrate 200 peaks coincide with each other, thus confirming the in-plane cube-on-cube epitaxial relationship for BSO films on STO(001) and MgO(001).

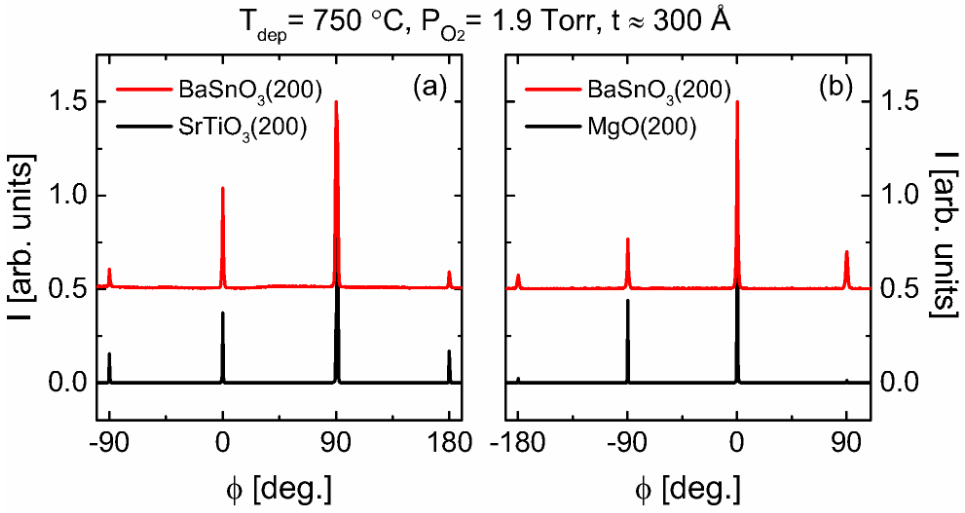

Fig. 4.2: Grazing incidence in-plane X-ray diffraction (GIIXD) of (a) $SrTiO_3$(001)/$BaSnO_3$ and (b) MgO(001)/$BaSnO_3$ films. The data are shown for both the film and substrate reflections (displaced for clarity). The films are 300-Å-thick and were deposited at 750 °C in 1.9 Torr of O_2.

Data of the type shown in Figs. 4.1(a,b) also provide the out-of-plane lattice parameter (a_{op}), a probe of stoichiometry and strain state. In Fig. 4.3 this is plotted *vs*. P_{O2}, deposition rate, and T_{dep}, for films of approximate thickness (t) 100 – 150 Å on both STO(001) and MgO(001). The values of the deposition parameters that were held constant are shown at the top of each panel. There are two notable features in these data. First, a_{op} is similar on STO and MgO, in almost all cases lying between 4.125 and 4.140 Å, despite the very different lattice mismatch. These values are close to but greater than (by 0.01 – 0.02 Å) the bulk lattice parameter [86, 130, 131] (horizontal line). Second, there is remarkable insensitivity to growth conditions over the probed parameter space. One simple interpretation is that, in this thickness range, the films on both substrates are already strain relaxed. The slightly elevated a_{op} could then indicate some level of cation non-stoichiometry (potentially from the ceramic target) or non-negligible defect density.

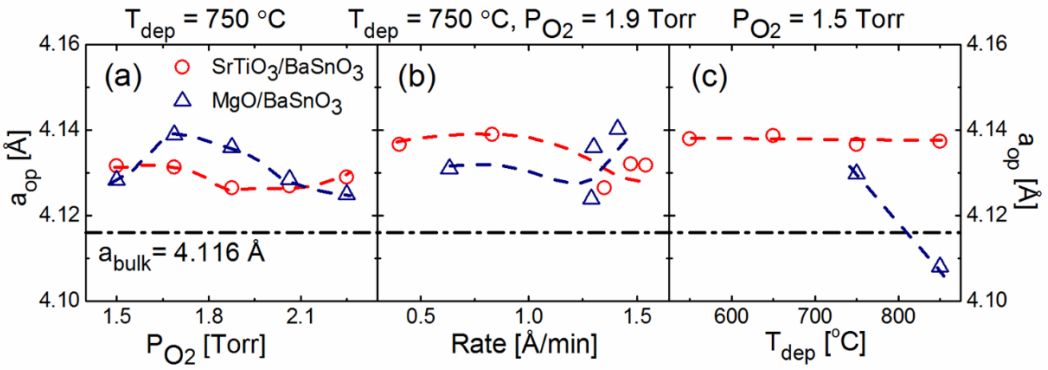

Fig. 4.3: Out-of-plane lattice parameter, a_{op}, *vs*. (a) O_2 growth pressure (P_{O2}), (b) deposition rate, and (c) deposition temperature (T_{dep}), for ~100–150-Å-thick BSO films on STO(001)

(red) and MgO(001) (blue). In each panel, the growth parameter(s) held fixed are labeled at the top. Error bars are comparable to the symbol size. The bulk BSO lattice parameter is shown by the dash-dot line. Dashed lines through the data are guides to the eye.

4.3.2 Strain Relaxation

Thickness-dependent strain relaxation was probed (Fig. 4.4) using BSO deposited on STO(001) at 750 °C in 1.5 Torr of O_2. In this figure, panels (a) through (c) plot a_{op}, the Scherrer length Λ (*i.e.* the 002 WAXRD peak width converted to a length *via* the Scherrer equation), and the 002 film RC full-width at half-maximum (FWHM). Two values of the latter are plotted, as *t*-dependent 002 RCs (See Appendix II Fig. A1) reveal a sharp peak superimposed on a broader one. To facilitate the discussion of strain state, Fig. 4.4(a) also shows the bulk lattice parameter, as well as the critical thickness for strain relaxation (t_{crit}) from the Matthews-Blakeslee formula [90], using literature parameters [132]. Although this t_{crit} is rather approximate for perovskites, it is nevertheless instructive to note that it is as low as 25 Å, due to the large mismatch. The data in Fig. 4.4(a) are indeed consistent with low t_{crit}; a_{op} decreases with increasing *t* from the lowest thicknesses probed, leveling off at $a_{op} \approx 4.13$ Å for $t \geq 150$ Å. It is noted (*i*) that this a_{op} is consistent with Fig. 4.3, and (*ii*) that no reliable lattice parameters could be extracted below 80 Å. That films on STO above $t \approx 150$ Å are indeed relaxed is confirmed by asymmetric (013) RSMs (Fig. 4.4(d), $t = 450$ Å), where the expected reflections from relaxed and fully strained (*i.e.* pseudomorphic) films are marked. The BSO peak is close to the fully relaxed position, but with minor lattice expansion. This is ascribed to minor cation non-stochiometry or defect formation, as returned to below. The *t* dependence of a_{op} was also studied on MgO (See Appendix II Fig. A2), full strain relaxation occurring by ~150 Å.

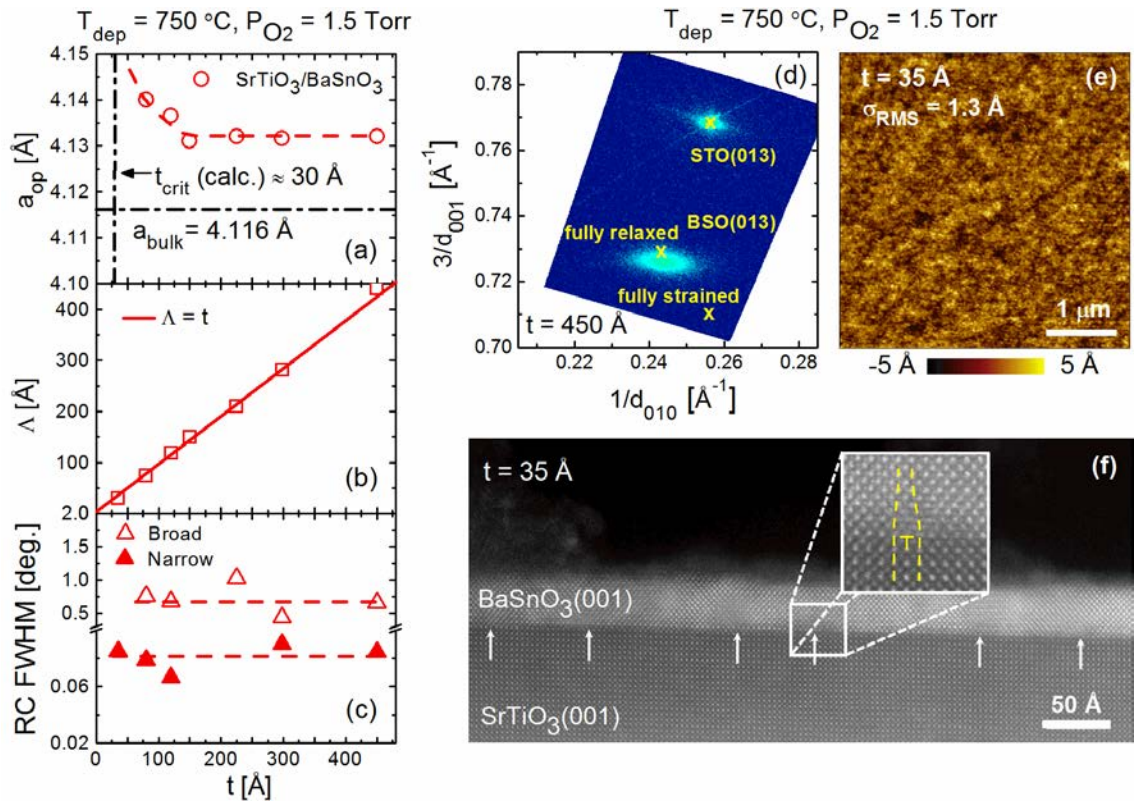

Fig. 4.4: Thickness dependence of (a) the out-of-plane lattice parameter, a_{op} (error bars are comparable to the symbol size), (b) the Scherrer length, Λ (*i.e.* the 002 WAXRD peak width converted to a length scale *via* the Scherrer equation), and (c) the two rocking curve FWHMs. All data are for STO(001)/BSO films deposited at 750 °C and 1.5 Torr. Dashed lines are guides to the eye. The dash-dot lines in (a) mark the bulk lattice parameter and calculated critical thickness, while the solid line in (b) is Λ = *t*. (d) Asymmetric reciprocal space map around the 013 reflection for a 450 Å film. Crosses mark the expected positions of fully strained and fully relaxed BSO. (e) Contact mode AFM image of a 35-Å-thick film. (f) Cross-sectional HAADF STEM image of a 35 Å film. Arrows mark misfit dislocations. Inset: magnified view of a misfit edge dislocation with Burger's vector *a*[100].

The *t*-dependence of the Scherrer length, Λ (Fig. 4.4(b)), further supports very low $t_{crit.}$ on STO(001). Specifically, Λ is found to almost exactly coincide with the thickness

(the solid line in Fig. 4.4(b) is $\Lambda = t$), meaning that the WAXRD widths are finite size dominated, with negligible broadening due to microstrain. This is consistent with the majority of the depth of such films being relaxed, *i.e.* very low t_{crit}. The RC FWHMs in Fig. 4.4(c) are also consistent with this, as they reveal little t dependence, the narrow contribution being barely broadened over the STO(001) substrate. Further work will be required to pin down the origin of the broader RC contribution, which is clearly evident (See Appendix Fig. A1) above $t \approx 100$ Å. This could be related to the expanded a_{op}, potentially reflecting a t-dependent density of defects such as misfit and threading dislocations.

To further probe defects, cross-sectional STEM was performed. Fig. 4.4(f) shows a representative HAADF STEM image of a 35-Å-thick BSO film, again on STO(001). A smooth, continuous film is evident even at this thickness (~8 unit cells), the major feature of interest being the quite evenly spaced dislocations, marked by arrows. A magnified view of one such dislocation is shown, from which it can be seen that these are misfit edge dislocations with Burger's vector along [100]. The spacing of these dislocations, averaged over multiple images, is 70 – 80 Å, close to the spacing expected (75 Å) if such misfit dislocations relax the full 5.4% lattice mismatch. This is again consistent with the diffraction observations of very low t_{crit}. STEM imaging of MgO(001)/BSO, shown in Fig. 4.5, reveals a similar picture, but with larger dislocation spacing due to the smaller mismatch. As a final comment, it is noted that the low surface roughness from STEM (Fig. 4.4(f)) and GIXR (Fig. 4.1(c)), is also corroborated by AFM. As shown in Fig. 4.4(e), a similar 35-Å-thick BSO film on STO(001) has an RMS roughness of only 1.3 Å.

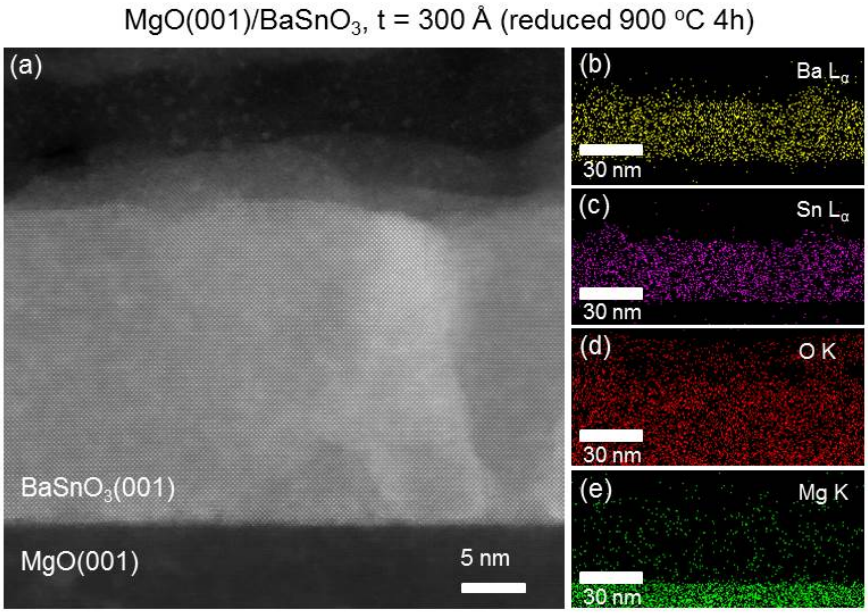

Fig. 4.5: (a) Cross-sectional HAADF STEM image from a 300-Å-thick BSO film on MgO(001) after reduction *via* vacuum annealing at 900 °C for 4 hrs. (b)-(e) Energy dispersive X-ray analysis maps of the Ba Lα peak, Sn Lα peak, O K peak, and Mg K peak. Note the different scales for (a) *vs* (b)-(e). The images are from the same film but are on a different scale. Most importantly, note the absence of any indications of regions with different chemical composition than the $BaSnO_3$ matrix, *i.e.* the absence of secondary phases such as binary oxides.

4.3.3 Oxygen Vacancy Doping

Having established the microstructure of these BSO layers, vacuum annealing was pursued to attempt reduction and *n*-doping. Note that as-deposited films displayed no measurable conduction at any P_{O2} or cooling atmosphere. Vacuum annealing was done for 4 hrs. at temperatures from 600 to 900 °C, using MgO(001)/BSO(t = 300 Å) films; no such experiments were performed on STO, due to anticipated complications with V_O formation in the substrates. Consistent with earlier work [86], no measurable conduction was induced below 600 °C. Above this, finite resistivity was detected, decreasing rapidly with annealing

temperature. We focus here, as an illustrative example, on 850 °C reduction. As shown in Fig. 4.6(a), the WAXRD data are largely unchanged after this vacuum annealing, confirming, within the limits of WAXRD, that no secondary phases form. This is strengthened by analytical STEM using energy dispersive X-ray analysis (Fig. 4.5(b-e)), which also detects no chemical inhomogeneity after annealing. The lattice parameter does change though, increasing by 0.009 Å, consistent with V_O formation.

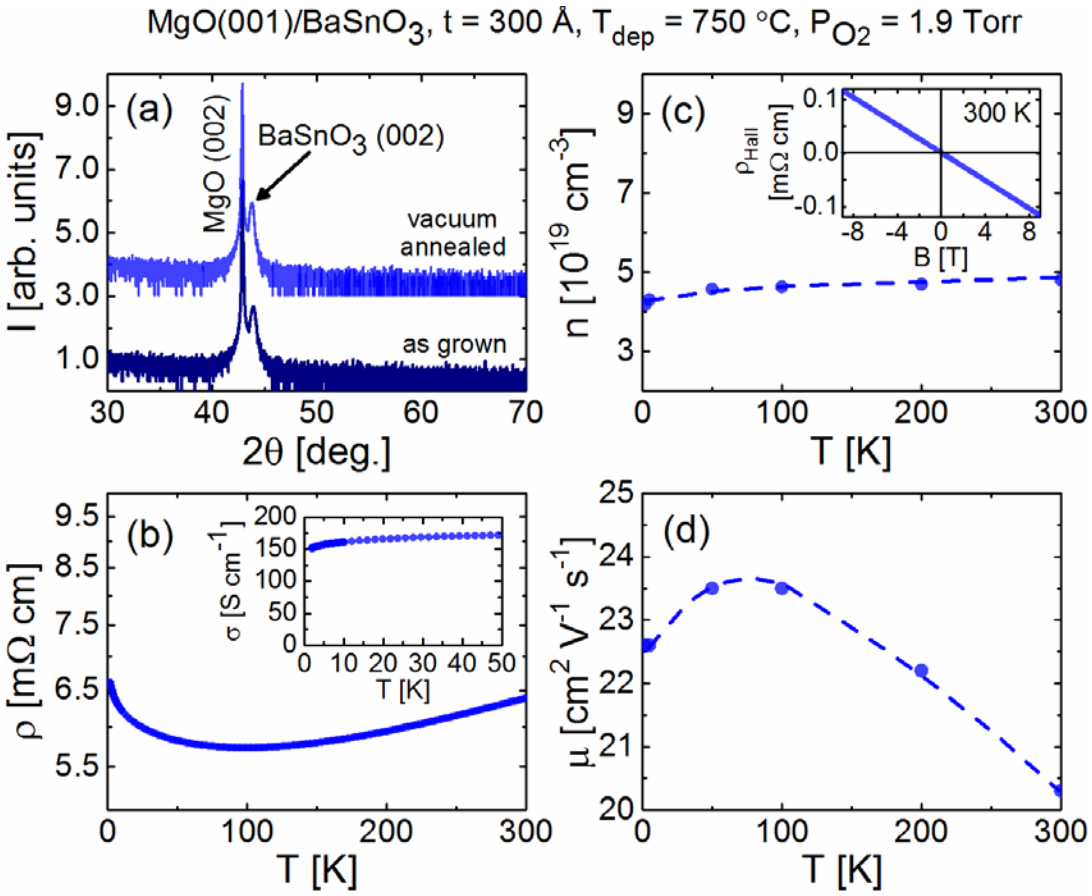

Fig. 4.6: (a) High resolution WAXRD from a 300-Å-thick MgO(001)/BSO film before and after vacuum annealing at 850 °C. Temperature dependence of (b) the (log scale) film resistivity, ρ, (c) the Hall electron density, n, and (d) the Hall electron mobility, μ. Dashed lines are guides to the eye. The insets to (b) show the conductivity, σ, *vs*. temperature below 50 K, and the zero-field-offset-subtracted 300 K Hall resistivity *vs*. magnetic flux density

(*B*), respectively. The growth conditions (750 °C, 1.5 Torr) are labeled at the top. Note that this film was sputtered at 66 W.

Electronic transport, however, reveals large changes in resistivity (ρ) and electron density (*n*) after annealing, implying reduction to $BaSnO_{3-\delta}$ and facile *n*-doping. As shown in Fig. 4.6(b) room temperature ρ values are ~6 mΩcm after 850 °C annealing, in comparison to unmeasurably high values (> 15 kΩcm) as-deposited. ρ decreases on cooling to ~100 K, below which it undergoes a weak upturn, to 6.5 mΩcm at 2 K. The weak temperature (*T*) dependence suggests degenerate doping and in fact the $T \rightarrow 0$ extrapolation of the conductivity, σ, appears finite (Fig. 4.6(b)), implying metallic behavior. Hall effect measurements further elucidate this. A clear, field-linear Hall signal due to electrons is observed (inset to Fig. 4.6(c)), *n* varying only weakly with *T* (Fig. 4.6(c)), consistent with degenerate doping. Additionally, although uncertainty in the effective mass and dielectric constant results in uncertainty in the Mott prediction for the critical electron density in BSO, our upper bound is ~10^{18} cm^{-3}. The observed *n* (5×10^{19} cm^{-3}, Fig. 4.6(c)) exceeds this, consistent with the metallicity deduced from the inset to Fig. 4.6(b). Both this observation and the field-linearity of the Hall voltage suggest relatively low compensation. As shown in Fig. 4.6(d) the deduced mobility (μ) is around 20 $cm^2V^{-1}s^{-1}$ at 300 K, increasing to 23.5 $cm^2V^{-1}s^{-1}$ at 50-100 K, before decreasing to 22.5 $cm^2V^{-1}s^{-1}$ at low *T*. Indications of phonon scattering contributions to the mobility are thus found, although scattering from defects such as dislocations is likely also important. In addition to establishing that V_O formation is facile in BSO and that it enables *n*-doping without impurities, these results point to numerous viable approaches to improve mobility. Substrate choice, thickness, and reduction temperature are obvious optimization variables, with the potential to elucidate the range of *n* obtainable by reduction, the resulting μ variation, the quantitative influence of misfit and threading dislocations, and, ultimately, the relative impact of the various defects on mobility.

4.4 Concluding Remarks

In summary, we have demonstrated the growth of epitaxial, phase pure, relaxed, close to stoichiometric BSO films on STO(001) and MgO(001) using high pressure oxygen sputter deposition. A detailed picture of the microstructure is provided, particularly with respect to strain relaxation *via* misfit dislocations. Importantly, vacuum annealing at 850 °C is found to induce oxygen vacancies at significant densities, without secondary phase formation, enabling facile *n*-doping. Mobilities of 20 $cm^2V^{-1}s^{-1}$ at 5 x 10^{19} cm^{-3} are obtained in films only 300 Å thick, with much scope for improvement. Ultimately this will enable a comparison of electronic properties obtainable by intrinsic *vs*. extrinsic doping in BSO, an important step for room temperature applications.

Chapter 5: Mobility-Electron Density Relation Probed *via* Controlled Oxygen Vacancy Doping in Epitaxial $BaSnO_3$

5.1 Chapter Overview

Critical open issues with $BaSnO_3$ (BSO) epitaxial films include determination of the optimal dopant and understanding the mobility-electron density (μ-n) relation. In this work, we extend the range over which $\mu(n)$ has been probed in BSO epilayers down to 2×10^{17} cm^{-3}, establishing $\mu \propto n^{0.65}$ over more than two orders of magnitude in n. Building on our prior demonstration of facile oxygen vacancy (V_O) doping in BSO films [92], this is achieved by tuning n over a wide range (2×10^{17} to 5×10^{19} cm^{-3}) simply by varying the post-deposition vacuum reduction temperature (T_{red}) from 600 – 900 °C. While V_O doping has been previously established in films [92] and bulk crystals (V_O formation during growth is presumed responsible for conductivity in undoped BSO [75] and the related $CdSnO_3$ [133]), *control* over n *via* T_{red} is demonstrated here, resulting in a 10^4-fold variation in 300 K resistivity, a transition from strong localization (with carrier freeze-out) to weak localization (with degenerate doping), and $\mu \propto n^{0.65}$ scaling. In addition to significantly improving our understanding of V_O doping in BSO, these findings are important for elucidating μ-limiting scattering mechanisms in BSO films.

5.2 Methods

Nominally undoped BSO epilayers of thickness 300 – 330 Å were deposited *via* RF high pressure oxygen sputtering on MgO(001) substrates (+2.3% (tensile) mismatch) at 750 °C. As discussed in Chapter 4, relaxed, single-phase, close to stoichiometric, smooth films were demonstrated by high resolution wide-angle X-ray diffraction, grazing

incidence in-plane diffraction, reciprocal space mapping, X-ray reflectivity, atomic force microscopy, and scanning transmission electron microscopy (STEM) with energy dispersive X-ray spectroscopy (EDX). A summary of structural characterization data/parameters for the current films is provided in Fig. A3 in Appendix III. Such films were annealed post-deposition at a single T_{red} between 600 and 900 °C for 4 hrs., at pressures < 10^{-7} Torr, in order to generate tunable V_O densities. Wide-angle X-ray diffraction and STEM/EDX measurements confirmed that the films remain single phase after vacuum annealing [92]. Temperature- and magnetic field-dependent DC electronic transport measurements were then made between 1.8 and 300 K in fields up to ±9 T, utilizing van der Pauw geometry indium contacts in a Physical Property Measurement System (Quantum Design, Inc.).

5.3 Results and Discussion

5.3.1 Influence of Reduction Temperature

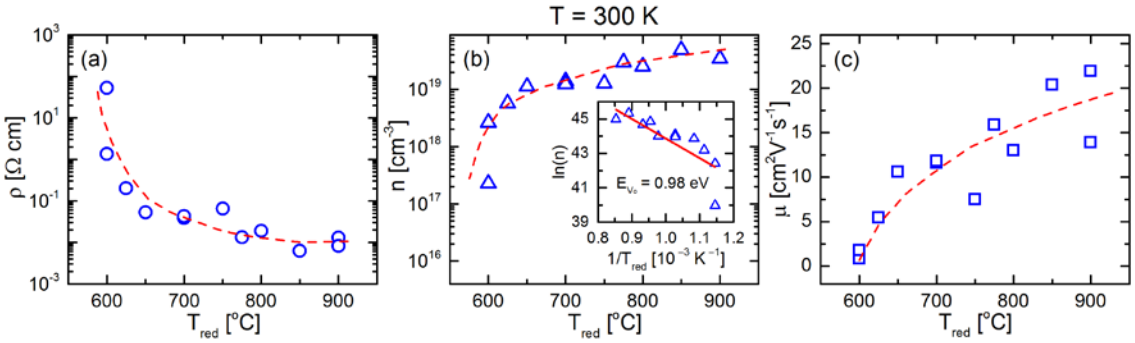

Fig. 5.1: Reduction temperature (T_{red}) dependence of (a) film resistivity, ρ (log scale), (b) Hall electron density, *n* (log scale), and (c) Hall electron mobility, μ, all at 300 K, for 4 hr. vacuum-annealed 300 – 330-Å-thick BSO films grown on MgO(001). Each film was reduced at a single T_{red}, with no sequential reduction; this is true throughout this study. Dashed red lines through the data are guides to the eye. Error bars are comparable to the symbol size. The inset in (b) shows the $n(T_{red})$ data on an Arrhenius plot (ln(*n*) *vs*. $1/T_{red}$),

the red solid line being a straight line fit. The latter yields an activation energy associated with oxygen vacancy formation, E_{V_O}, of 0.98 eV.

The influence of variable temperature vacuum annealing on the electronic properties of these BSO films is illustrated in Figs. 5.1(a-c), where the 300 K ρ, *n*, and μ are plotted *vs.* T_{red}. As can be seen from Fig. 5.1(a), detectable conduction first emerges at T_{red} = 600 °C, ρ decreasing from ~10^2 to <10^{-2} Ωcm (the lowest value in Fig 5.1(a) is 6 mΩcm) as T_{red} is increased to 900 °C. This onset temperature for conduction is roughly consistent with a recent report where *La-doped* BSO films were shown to have O_2-pressure-sensitive transport properties above ~ 500 °C [134]. Fig 5.1(b) shows that the 10^4-fold decrease in ρ(300 K) is driven by an increase in 300 K *n* from 2 × 10^{17} cm^{-3} at T_{red} = 600 °C to 5 × 10^{19} cm^{-3} at 900 °C (Fig. 5.1(b)). We ascribe this largely to an increase in V_O density with increasing T_{red}, although annealing of defects at the highest T_{red} could contribute. The inset to Fig. 5.1(b) shows the natural logarithm of *n*(300 K) *vs*. $1/T_{red}$, where reasonable adherence to Arrhenius behavior is revealed, with an activation energy associated with V_O doping of 0.98 eV. The equivalent for $SrTiO_3$ lies at ~2 eV [15], highlighting the efficacy of V_O doping in $BaSnO_3$. We note, however, that the 0.98 eV determined here is specifically for BSO thin films, and could change for bulk reduction, as in a single crystal for example. The increasing importance of compensating/deep defects at low *n* will also lead to progressively more significant differences between *n* and the donor density (N_d); the activation energy from an N_d *vs*. $1/T_{red}$ plot would thus be lower than determined here from Fig. 5.1(b).

As shown in Fig. 5.1(c), the 300 K mobility also increases substantially with reduction, from 0.8 $cm^2V^{-1}s^{-1}$ at T_{red} = 600 °C to 22 $cm^2V^{-1}s^{-1}$ at 900 °C. Note that no conductivity could be detected below 600 °C, and that the upper limit of 900 °C is purely experimental; reduction at higher temperatures or under more reducing conditions thus has potential to generate even higher *n* and μ. Moreover, while the MgO(001) used here is ideal in terms of eliminating V_O formation in the substrate, this is sub-optimal in terms of lattice

symmetry matching, and there is thus substantial scope for improvement in n and μ in V_O-doped BSO films. What is critical, however, is that by lowering T_{red}, Hall densities as low as 2×10^{17} cm^{-3} are achieved here. These n values are, to our knowledge, the lowest probed to date in BSO. The implications of this for the likely acceptor/deep level density are discussed below, although we note immediately from Figs. 5.1(a,b) that sample-to-sample variations begin to become significant at the lowest T_{red} (*i.e.*, 600 °C), as might be expected in the limit where compensating defects/deep levels become important.

5.3.2 Insulator-Metal Transition

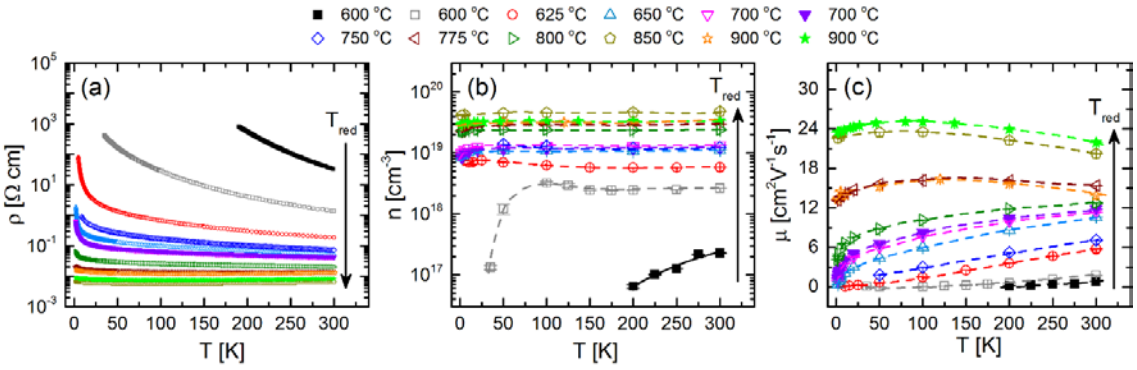

Fig. 5.2: Measurement temperature (T) dependence of (a) film resistivity, ρ (log scale), (b) Hall electron density, n (log scale), and (c) Hall electron mobility, μ, for 4 hr vacuum-annealed 300 – 330-Å-thick BSO films grown on MgO(001). The reduction temperature, T_{red}, was varied between 600 and 900 °C, as indicated in the legend at the top; solid points indicate repeated samples at certain T_{red}. Dashed lines through the data are guides to the eye, whereas the black solid line through the solid black square points in (b) is an Arrhenius fit with an activation energy of 68 meV. Error bars are comparable to the symbol size.

Further insight into the electronic transport properties of these V_O-doped BSO films is provided by Figs. 5.2(a-c) which plot, for 12 films with T_{red} between 600 and 900 °C, the measurement temperature (T) dependence of ρ (log scale), n (log scale), and μ. As can

be seen from Fig. 5.2(a), the 10^4-fold decrease in ρ(300 K) with increasing T_{red} is amplified at low T, an apparent insulator-metal transition (IMT) occurring around T_{red} = 700-800 °C. This is supported by Fig. A2 in Appendix III, where the $T \rightarrow 0$ extrapolation of the conductivity appears finite only for $T_{red} \geq 775$ °C. Even the most conductive films display a small upturn in ρ at the lowest T, however, likely due to weak localization. Plots of ln(ρ) *vs.* T^{-1} (Fig. 5.3(a)) provide a similar picture, the activation energy decreasing with T_{red} and becoming negligible (at least down to 1.8 K) at $T_{red} \approx 775$ °C. Zabrodskii analysis [135] (Fig. 5.3(b)) further corroborates this picture, suggesting an apparent IMT around $T_{red} \approx$ 775 °C. The temperature dependence of ρ for insulating behavior has the functional form $\rho = \rho_0 \exp (T_0/T)^m$, where ρ_0 is the $T \rightarrow \infty$ value of ρ, T_0 is a characteristic temperature, and m is a constant related to the transport mechanism. $\rho(T)$ can be linearized using a logarithmic derivative method (Zabridskii analysis), where a quantity ln(W) [$W = -$ d(lnρ)/d(ln$T$)] is plotted as a function of ln(T) to yield the exponent, m. The most insulating film (T_{red} = 600 °C) in Fig. 5.3(b) displays Efros-Shklovskii variable range hopping with m = 0.5.

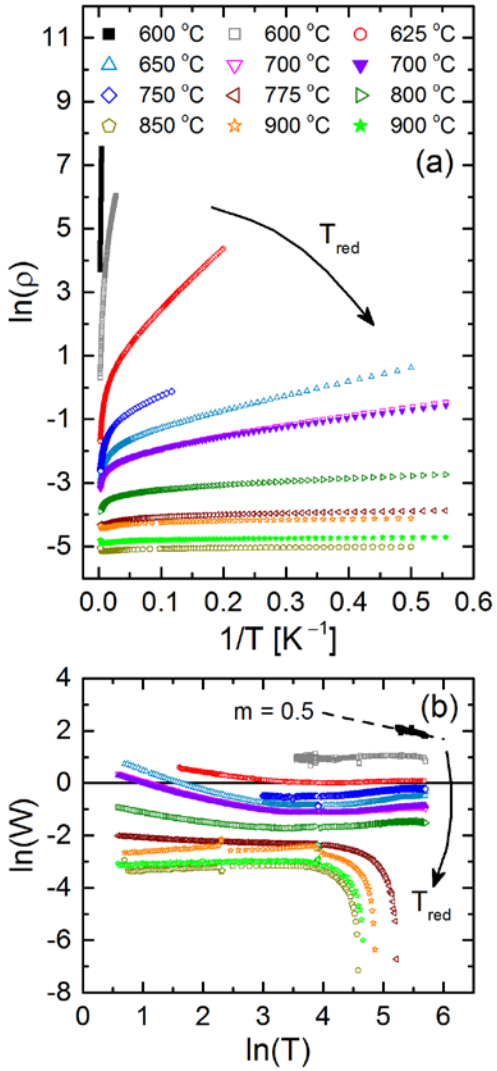

Fig. 5.3: (a) Natural logarithm of the film resistivity (ρ) *vs.* inverse temperature (T^{-1}) for 300 – 330-Å-thick epitaxial BSO films on MgO(001) annealed in vacuum at 600 °C < T_{red} < 900 °C. Note the negligible activation energy (at least down to 1.8 K) for T_{red} values ≳ 775 °C. (b) Zabrodskii plot of the data shown in (a). This is a plot of ln(W) *vs.* ln(T), where $W = -d\ln(\rho)/d\ln(T)$, linearizing $\rho = \rho_o \exp(T_0/T)^m$ and yielding $-m$ as the slope. The most insulating sample (T_{red} = 600 °C) has behavior consistent with m = 0.5 (dashed line) suggesting Efros-Shklovskii variable range hopping. As T_{red} increases, ln(W) changes sign and becomes quite flat at low T, indicating a crossover from strong localization to metallic-like behavior.

Fig. 5.2(b) shows the accompanying trends in $n(T)$ with T_{red}. At $T_{red} \gtrsim 775$ °C, where $\rho(T)$ is metallic-like, n is essentially T-independent, evidencing degenerate doping. At $T_{red} \lesssim 775$ °C, where strongly localized $\rho(T)$ occurs, decreases in n at the lowest T become progressively more obvious. The apparent IMT can be seen in Fig. 2(b) to occur at a critical density in the 10^{18} cm^{-3} range, which can be compared to the Mott prediction for the critical density in *uncompensated* BSO of $\sim 1\times10^{17}$ cm^{-3} (using an electron effective mass of 0.19 [72], and a dielectric constant of 20 [136]). That these critical densities are in even approximate agreement demonstrates that the density of compensating defects/deep levels is relatively low here ($\lesssim 10^{17}$ cm^{-3}), consistent with the measurable conductivity down to $n = 2\times10^{17}$ cm^{-3}. At these lowest n carrier freeze out is substantial, the most insulating film in Fig. 5.2(b) exhibiting an Arrhenius dependence (the black solid line in Fig. 5.2(b) is a fit to $n = n_\infty \exp(-E_A/k_BT)$ where n_∞ and E_A are constants) with activation energy, $E_A = 68$ meV. We interpret this significant energy in terms of the density of compensating defects/background charges becoming significant in comparison to the V_O density at these n values ($\sim10^{17}$-10^{18} cm^{-3}), lowering the Fermi level below the band edge. Surface/interface depletion may also play a role in this regime. As shown in Fig. 5.4, for reasonable values of surface pinning potential the depletion thickness becomes comparable to the film thickness around $n \approx 10^{18}$ cm^{-3}.

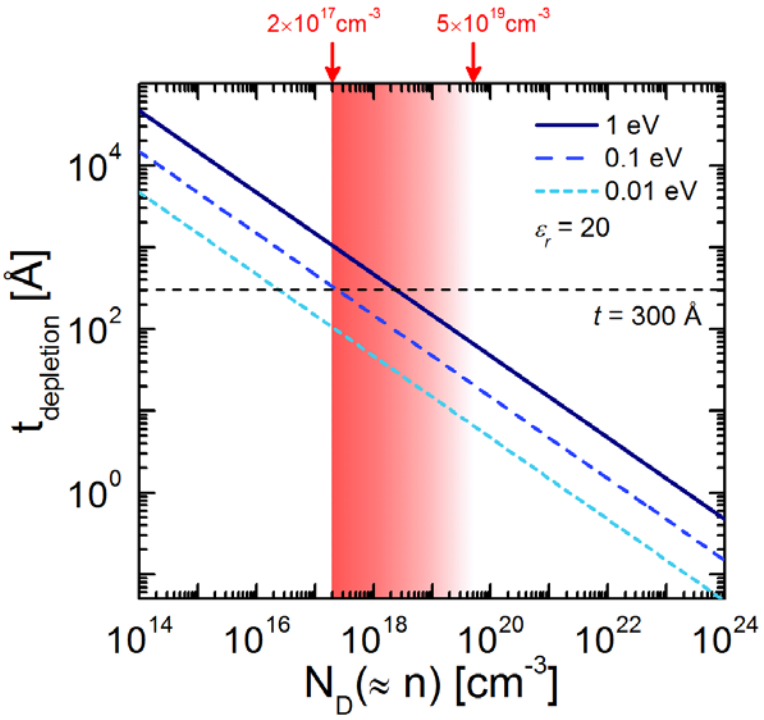

Fig. 5.4: Plot (log-log) of estimated depletion layer thickness, $t_{depletion}$, *vs.* donor density, N_D, for a surface pinning potential, V_{bi}, varying between 0.01 and 1 eV. $t_{depletion} = (2\varepsilon_r\varepsilon_0 V_{bi}/eN_D)^{1/2}$ was used, where ε_r and ε_0 are the relative and vacuum permittivities, and e is the electronic charge. The dielectric constant of BSO was assumed to be 20 [136]. The red shaded region marks the electron density range probed in this work in vacuum-annealed BSO films, *i.e.*, between 2×10^{17} and 5×10^{19} cm^{-3}. The black horizontal dashed line marks the film thickness, t = 300 Å. It can be seen that at densities below about 10^{18} cm^{-3}, $t_{depletion}$ becomes comparable to t.

Fig. 5.2(c) shows the resulting $\mu(T)$. At the highest T_{red}, μ increases on cooling to $T \approx 75$ K, below which it decreases. This evidences the typical competition between phonon scattering (thought to be from longitudinal optical phonons in BSO) [57, 69] and defect scattering (likely from a combination of dislocations and ionized impurities) [57]. As T_{red} is decreased, however, indications of phonon-related mobility are gradually lost, T_{red} values

below ~775 °C resulting in μ that decreases monotonically on cooling, indicating dominant defect scattering. This is qualitatively consistent with prior work on La-doped BSO epilayers [57]. In the 300 – 330 Å films reported here the maximum observed mobility is 25 $cm^2V^{-1}s^{-1}$, although we note again that much scope for improvement exists in V_O-doped films, particularly *via* substrate optimization and/or buffer layer incorporation; the current choice (MgO) rules out artifacts due to V_O formation in the substrate, but is sub-optimal in terms of lattice parameter and symmetry mismatch. Recent work, for example, has established 97 $cm^2V^{-1}s^{-1}$ in La-doped BSO on MgO(001) *via* the use of thick undoped BSO buffer layers[100].

5.3.3 Mobility-Electron Density Relation

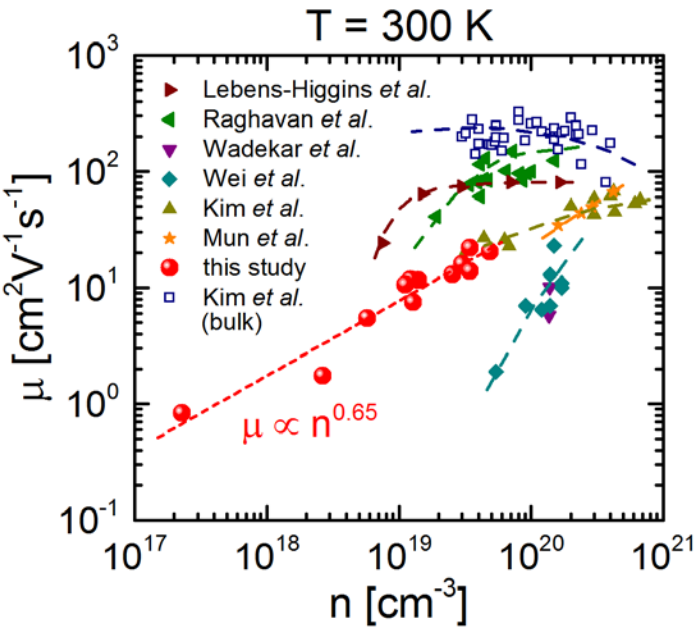

Fig. 5.5: Log-log plot of the 300 K Hall electron mobility, μ, *vs*. the 300 K Hall electron density, *n*, for the oxygen-vacancy-doped BSO films measured in this study (red solid circles), and from other reports of La-doped BSO in the literature [47, 48, 56, 91, 95, 101, 137]. The open square points are for La-doped bulk single crystals, and the solid points are

for La-doped epitaxial films. All error bars are comparable to the symbol size. The linear fit to our data (red dashed line) yields a slope of 0.65, *i.e.*, $\mu \propto n^{0.65}$.

Clearly, from Figs. 5.1 and 5.2 there must exist substantial *n* dependence of μ, tuned in this case *via* T_{red} (and thus V_O density). This is typically the case in BSO, as summarized in Fig. 5.5 which plots μ *vs*. *n* at 300 K, including data from the current work and a spectrum of prior literature. The blue open squares represent La-doped bulk crystals, where μ varies only relatively weakly with *n* in the range $3 \times 10^{19} - 4 \times 10^{20}$ cm^{-3}. Following Krishnaswamy *et al*. [69], this can be understood in terms of ionized impurity and longitudinal optical phonon scattering. The situation is different in La-doped epitaxial films, however (the small solid points are from prior reports[47, 48, 56, 91, 95, 101, 137]), which, although restricted to above ~1×10^{19} cm^{-3}, show μ increasing with *n*. The larger circular red points in Fig. 5.5 show the results from the current study, which, it should be noted uses V_O-doping as opposed to La-doping. As mentioned above, this study spans a much larger range in *n*, decreasing the minimum *n* by a factor of ~35. As shown by the dotted line, $\mu \propto n^{0.65}$ is found to describe the data over the entire *n* range studied. This is close to the $n^{0.5}$ that might be expected from dislocation scattering alone [102], the deviation being perhaps unsurprising given the additional contributions expected from ionized impurities and phonons [57]. Along these lines, the considerable scatter in μ(*n*) among the various La-doped film studies shown in Fig. 5.5 is noteworthy, being consistent with variable densities of dislocations, impurities, non-stoichiometry-related defects, deep levels, *etc*. Fig. 5.5 also underscores the potential of V_O-doping in BSO, the current mobilities apparently being limited *only* by the V_O-controlled electron density, which could be substantially increased with more aggressive reduction.

5.4 Concluding Remarks

In summary, we have demonstrated that the electron density in oxygen-vacancy-doped $BaSnO_3$ epilayers can be readily tuned simply by varying the post-deposition

vacuum annealing temperature. Varying this from 600 to 900 °C in 300-Å-thick high pressure oxygen sputter-deposited films on MgO(001) results in Hall densities between 2 × 10^{17} and 5 × 10^{19} cm^{-3}, resistivity between 10^{2} and $<10^{-2}$ Ωcm, and transport between strongly localized and metallic-like. This work, therefore, accesses a lighter doped regime than prior work on $BaSnO_3$, potentially indicating lower levels of compensating defects/deep traps than some prior studies. We find that the mobility increases as $n^{0.65}$ over the entire doping range studied. This work thus not only elucidates oxygen vacancy doping in $BaSnO_3$, and the mobility-electron density relation that is important to understand scattering mechanisms but also lays the foundation for future work optimizing mobility in vacancy-doped $BaSnO_3$ films. More aggressive reduction, lower mismatch substrates [56, 91, 95], buffer layer systems [57, 98, 99], and modulation doping hold promise in this regard.

Chapter 6: Thickness-Driven Insulator-Metal Transition and Two-Dimensional Weak Localization in Epitaxial $BaSnO_3$ Thin Films

6.1 Chapter Overview

A low temperature resistivity upturn is frequently observed in $BaSnO_3$, suggesting proximity to a disorder-driven metal-insulator transition. Here, we investigate these phenomena *via* detailed temperature- and magnetic field-dependent electronic transport measurements on $BaSnO_3$ films grown on $GdScO_3$(001), $SrTiO_3$(001), and $LaAlO_3$(001) substrates by high pressure oxygen sputter deposition. Structural characterization reveals phase-pure, close to stoichiometric, smooth, epitaxial $BaSnO_3$(001), but with substantial thickness-dependent defect densities related to lattice mismatch. Relatively thick (> 1000 Å) 2%-La-doped films exhibit clearly metallic transport, with degenerate Hall electron density of 3.5×10^{20} cm^{-3}, and low temperature resistivity and mobility of 200 μΩcm and 91 $cm^2V^{-1}s^{-1}$; 300 K mobilities reach 60 $cm^2V^{-1}s^{-1}$. Oxygen-vacancy-doped films, on the other hand, have lower maximum Hall electron density of 5×10^{19} cm^{-3}, and with decreasing thickness show reduced electron density, reduced mobility, and a systematic resistivity upturn at low temperatures. This upturn is approximately logarithmic in temperature and is accompanied by anisotropic negative magnetoresistance. Analysis of the temperature and field dependence reveals generally good agreement with two-dimensional weak localization models, revealing dominant dephasing by electron-electron scattering. It is thus proposed that at reduced thickness compensation and disorder drive a transition from metallic to two-dimensional weakly localized transport, and, for thicknesses below ~100 Å, strong localization is eventually induced.

6.2 Methods

High pressure oxygen sputter deposition was carried out from 2” dia. nominally undoped $BaSnO_3$ (BSO) and 2% La-doped-$BaSnO_3$ (BSO:La) targets synthesized by solid-state reaction of $BaCO_3$, La_2O_3 (for BSO:La), and SnO_2 (> 99.9 % purity) in air at 1200

°C, followed by cold-pressing and sintering at 1400 – 1450 °C. Prior to growth, the substrates were annealed for 15 min in 1.9 Torr of O_2 at 900 °C. Subsequently, BSO films were deposited using RF sputtering carried out at 66 – 76 W, with 750 °C substrate temperature (T_{sub}), 1.9 Torr O_2 pressure (P_{O2}), and a growth rate of 2 Å/min. BSO:La films were DC sputtered at 150 mA, with T_{sub} = 900 °C, P_{O2} = 1.9 Torr, and a growth rate of 7.8 Å/min. Post-growth cooling was done in 600 Torr of O_2. High resolution wide angle X-ray diffraction (WAXRD) and grazing incidence X-ray reflectivity (GIXR) were performed with Cu K_α radiation in a Panalytical X'Pert system. GenX [126] was used for the GIXR refinement. Contact mode atomic force microscopy (AFM) was carried out in a Bruker Nanoscope V Multimode 8. Cross-sectional transmission electron microscopy samples were prepared using FEI Helios Nanolab G4 dual-beam focused ion beam, where the samples were thinned using a 30 kV Ga-ion beam and further polished using a 2 kV Ga-ion beam to eliminate damaged layers at the surface. Scanning transmission electron microscope (STEM) imaging was carried out using an aberration-corrected FEI Titan G2 60-300 STEM at 200 keV with ~30 pA beam current. The convergent semi-angle of the incident STEM probe was 17.2 mrad and the annular dark-field (ADF) detector inner angles were 19 mrad, 55 mrad, and 93 mrad for low-angle ADF (LAADF), medium-angle ADF (MAADF), and high-angle ADF (HAADF) images, respectively. High-magnification ADF-STEM images were filtered using 'HRTEM Filter' in Gatan Digital Micrograph software to remove amorphous components in the images [64]. Undoped BSO films were annealed in vacuum at 900 °C for 4 hrs. at pressures < 10^{-7} Torr, resulting in V_O doping. Temperature and magnetic field dependent electronic transport measurements (DC, 1.8–300 K, 0 – 9 T) were carried out in Quantum Design Physical Property Measurement Systems (PPMSs) using indium contacts in a van der Pauw geometry. All such contacts were ohmic at the current densities used during the measurements.

6.3 Results and Discussion

6.3.1 Structure

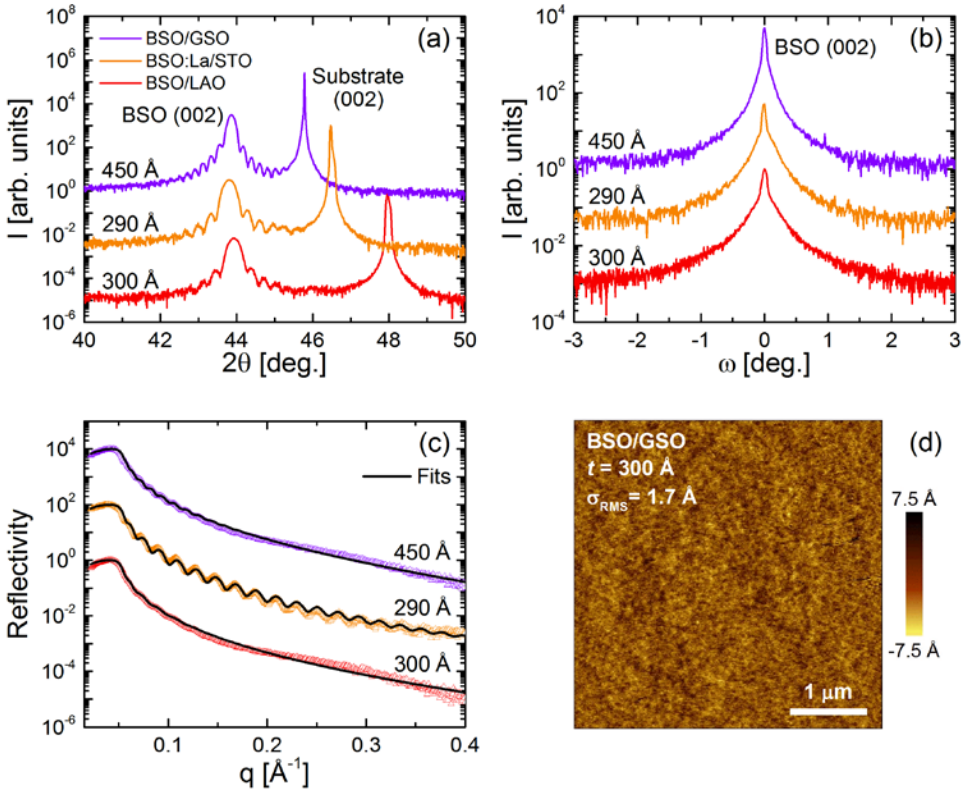

Fig. 6.1: Structural characterization of 290 – 450 Å-thick $BaSnO_3$ (BSO) films on $LaAlO_3$(001) (red), $SrTiO_3$(001) (orange), and $GdScO_3$(001) (violet). Orange curves correspond to 2% La doped BSO films, all others to undoped BSO films. (a) High-resolution wide-angle X-ray diffraction showing the 002 substrate and film reflections. (b) Rocking curves through the 002 film reflection. (c) Grazing incidence X-ray reflectivity with fits (solid black lines). The refined film surface roughnesses are 2–2.5 Å. Film thicknesses are shown aside each curve. (d) Contact mode atomic force microscopy image of a 300-Å-thick undoped BSO film on $GdScO_3$(001), with a root-mean-square roughness of 1.7 Å. Curves in (a), (b), and (d) offset for clarity.

To illustrate the basic structural features of the oxygen sputter-deposited films, WAXRD scans for three films are presented in Figs. 6.1(a,b): 300 Å and 450-Å-thick BSO

films on $LaAlO_3$(001) [LAO, -8.6% mismatch] and $GdScO_3$(001) [GSO, -3.9% mismatch], respectively, and a 290-Å-thick BSO:La on $SrTiO_3$(001) [STO, -5.4% mismatch]. Fig. 6.1(a) reveals only 002 substrate and film reflections, thus establishing phase purity (within detection limits) and epitaxial growth. The presence of finite size fringes indicates that the films grown on all the above-mentioned substrates are smooth on short lateral length scales. The out-of-plane lattice parameters (a_{op}) extracted from the data in Fig. 6.1(a) are 4.121 Å for 300-Å-thick LAO(001)/BSO, 4.125 Å for 450-Å-thick GSO(001)/BSO and 4.13 Å for 290-Å-thick STO(001)/BSO:La, the bulk value for BSO being 4.116 Å. This suggests that the films are nominally stoichiometric, with full strain relaxation occurring only in the LAO(001)/BSO film. The slightly expanded out-of-plane lattice parameter on GSO and STO is possibly due to residual strain in these films. Fig. 6.1(b) shows the rocking curves (RCs) through the 002 BSO reflection, revealing the presence of two peak components in each case. Specifically, a narrow peak (FWHM = 0.05° – 0.07°) superimposed on a broader one (FWHM = 0.3° – 0.5°). The mosaicity of the narrow components coincide roughly with those of the substrates, whereas the broad peak's mosaic spread likely arises due to the presence of line defects in the films. The presence of fringes in the GIXR of the films, presented in Fig. 6.1(c), suggests that all films are smooth on the long lateral length scale probed in GIXR. The refined surface roughnesses of the films lie in the range of 2 – 2.5 Å. This is further corroborated by contact mode AFM as shown in Fig. 6.1(d) for a 300-Å-thick BSO on GSO(001). This film shows an RMS roughness of only 1.7 Å.

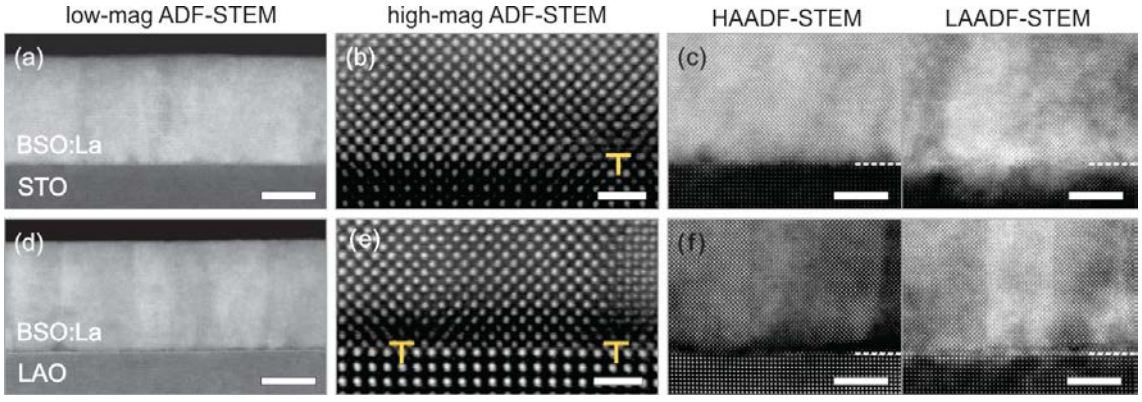

Fig. 6.2: (a–c) Annular dark field scanning transmission electron microscopy (ADF-STEM) images of a 290-Å-thick $Ba_{0.98}La_{0.02}SnO_3$ (BSO:La) film on $SrTiO_3$(001): (a) low

magnification image (scale bar = 150 Å), (b) high magnification image of the substrate/film interface (scale bar = 10 Å), and (c) complementary high-angle ADF (HAADF) (left) and low-angle ADF (LAADF) (right) STEM images (scale bar = 50 Å). (d–f) ADF-STEM images of a 280-Å-thick $Ba_{0.98}La_{0.02}SnO_3$ (BSO:La) film grown on $LaAlO_3$(001): (d) low magnification image (scale bar = 150 Å), (e) high magnification image of the substrate/film interface (scale bar = 10 Å), and (f) complementary HAADF (left) and LAADF (right) STEM images (scale bar = 50 Å). The symbols in (b) and (e) mark misfit dislocations.

To investigate defects and disorder arising from strain relaxation, particularly threading dislocations (TDs) and misfit dislocations (MDs) near the film/substrate interface, cross-sectional STEM images were acquired. The low-magnification MAADF-STEM images in Figs. 6.2(a) and (d) show the overall crystalline morphology of 290 Å and 280-Å-thick BSO:La films deposited on STO(001) and LAO(001), respectively. These images show uniform film thickness and smooth surface over a large lateral length scale, sharp film/substrate interface, and vertical contrast arising from small-angle boundaries (rotational disorder) in both the films. The small-angle boundaries likely arise because of the accumulation of threading dislocations separating two regions that are slightly misoriented in the in-plane directions. Figs. 6.2(b) and (e) are high magnification atomic-resolution HAADF-STEM images showing atomically-sharp interfaces in both the films. The BSO:La/LAO interface, in addition, shows a distinct dark contrast on the BSO:La side of the film/substrate interface. The high density of MDs, as expected for such a high film/substrate lattice mismatch, is most likely responsible for the contrast near the interface. Such MDs, having *a*[100] Burger's vectors, are clearly indicated in both the images with yellow symbols. The spacing of these MDs averaged over multiple images are 75-85 Å and 45-50 Å for the STO(001)/BSO:La and LAO(001)/BSO:La films, respectively, close to the theoretically predicted spacing in both cases. The presence of MDs near the interface results in local atomic displacements from their equilibrium positions, thus resulting in strain. A comparison between the HAADF and LAADF images from the same region helps us to visualize the strain. These images are presented in Fig.

6.2(c) and (f) for the BSO:La films on STO(001) and LAO(001), respectively. HAADF images are highly sensitive to atomic number (*Z*) contrast, whereas LAADF images, in addition to *Z* contrast, show some sensitivity to strain. Clearly, in the LAADF images, the interfaces appear brighter compared to the unstrained bulk region in both the films, suggesting the presence of strain resulting from the bending of atomic planes around the MD cores.

6.3.2 Insulator-Metal Transition

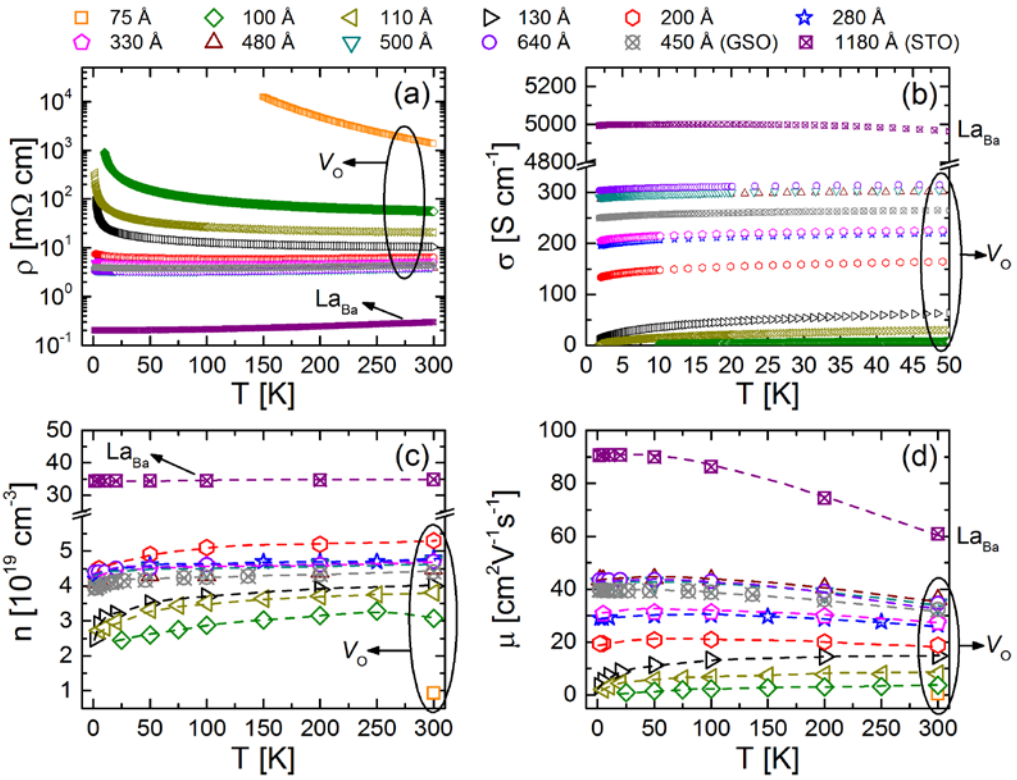

Fig. 6.3: Temperature (*T*) dependence of (a) the film resistivity (log scale), ρ, (b) the film conductivity, σ = 1/ρ, below 50 K, (c) the Hall electron density, *n*, and (d) the Hall electron mobility, μ, for doped $BaSnO_3$ (BSO) films on $LaAlO_3$(001), $SrTiO_3$(001), and $GdScO_3$(001). Thicknesses are shown at the top of the figure. Films on $LaAlO_3$ (75–640-Å-thick) and $GdScO_3$ (450 Å, grey) were annealed in vacuum for 4 hrs at 900 °C to oxygen

vacancy dope (labeled "V_O"), whereas the film on $SrTiO_3$ (1180 Å, purple) is 2% La doped (labeled "La_{Ba}"). Dashed lines are guides to the eye.

Having thoroughly characterized the structural properties of BSO and BSO:La films, detailed temperature and field dependent electronic transport measurements were performed to gain insight into the electronic conduction mechanisms in these films. Similar to our earlier reports [92, 93], in order to dope BSO films grown on LAO(001) and GSO(001) with oxygen vacancies (V_O) vacuum annealing was carried out at 900 °C for 4 hrs. Figs. 6.3(a–d) plot the measurement temperature (T) dependence of film resistivity, ρ (log scale), conductivity, σ, Hall electron density, n (log scale), and Hall electron mobility, μ, for ten 75 – 640 Å-thick LAO(001)/V_O-doped BSO films, a 450 Å-thick GSO(001)/V_O-doped film (grey), and a 1180 Å-thick STO(001)/BSO:La film (purple). The results on the 2% La-doped film is presented here as a "standard" for comparison. As can be seen in Fig. 6.3(a), for the films on LAO(001), a 10^3-fold decrease in ρ(300 K) from ~1 Ωcm (75 Å film) to ~3 mΩcm (640 Å film) occurs systematically with an increase in film thickness (t). This decrease in ρ, which is amplified at low T, is accompanied by an apparent insulator-metal transition (IMT) occurring around t = 130-200 Å. Not surprisingly, both the 450 Å-thick GSO(001)/V_O-doped BSO film and the 1180 Å-thick STO(001)/BSO:La film lie on the metallic side ($d\rho/dT > 0$) of the transition. The IMT is also supported by Fig. 6.3(b), where the $T \rightarrow 0$ extrapolation of σ appears finite only for $t \geq 200$ Å. Furthermore, ln(ρ) *vs.* T^{-1} plots in Fig. A5 in Appendix IV suggests a similar story, where the activation energy decreases continuously with t and becomes negligible above t = 130 Å.

Figs. 6.3(c) and (d) show the trends of $n(T)$ and $\mu(T)$ with t, respectively. For $t \geq$ 200 Å, where $\rho(T)$ is metallic, n is essentially independent of T, the signature of degenerate doping. For the V_O-doped BSO films, this value of n is about 4.5×10^{19} cm^{-3}, whereas for the STO(001)/BSO:La film it is 3.5×10^{20} cm^{-3} (100% La dopant activation). $\mu(T)$ in these films increases upon cooling, down to ~50 K, below which it either shows saturation or a small decrease, thus indicating a competition between phonon scattering and defect scattering (both dislocations and ionized impurities). As t is decreased below 200 Å, freeze

out (lowering *n* values) at low *T* becomes increasingly apparent, with the overall *n* showing a systematic decrease with *t* due to compensation and/or surface/interface depletion of electrons. μ(*T*) monotonically decreases on cooling in these films, suggesting the dominance of defect scattering. It is evident that with decreasing *t*, electronic disorder increases in the films, resulting in a decrease in *n* and μ. For the V_O-doped films on LAO(001) and GSO(001) reported here, the maximum observed mobility is ~45 $cm^2V^{-1}s^{-1}$, an improvement over the 25 $cm^2V^{-1}s^{-1}$ achieved in V_O-doped films on MgO(001). This emphasizes the positive influence of symmetry matching on electron mobility. The maximum μ(*T*) for the BSO:La film is ~90 $cm^2V^{-1}s^{-1}$, suggesting that there still exists a scope for further improvement in μ if parameters like *n*, *t*, lattice mismatch, buffer layers, *etc*. are optimized.

6.3.3 Two-Dimensional Weak Localization

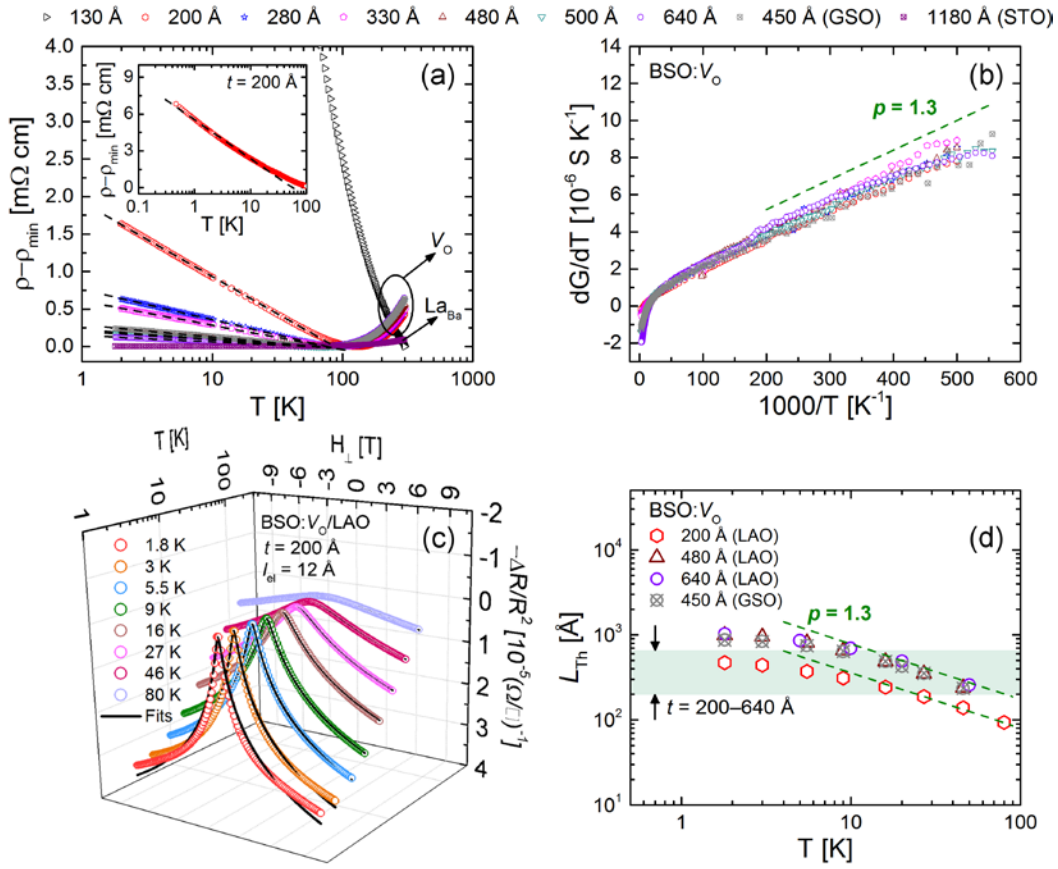

Fig. 6.4: (a) Temperature (T) dependence (log scale) of the film resistivity, plotted as $\rho - \rho_{min}$ where ρ_{min} is the minimum resistivity, for doped $BaSnO_3$ (BSO) films on $LaAlO_3(001)$, $SrTiO_3(001)$, and $GdScO_3(001)$. Inset: $\rho - \rho_{min}$ on a log scale for a 200-Å-thick BSO film on $LaAlO_3(001)$ plotted down to 500 mK. Thicknesses are shown at the top of the figure. Films on $LaAlO_3$ (75 – 640-Å-thick) and $GdScO_3$ (450 Å, grey) were annealed in vacuum for 4 hrs. at 900 °C to oxygen vacancy dope (labeled "V_O"), whereas the film on $SrTiO_3$ (1180 Å, purple) is 2% La doped (labeled "La_{Ba}"). Dashed lines through the data are fits to a 2D weak localization model. (b) The temperature derivative of sheet conductance, dG/dT, *vs*. inverse temperature, plotted as $1000/T$, for V_O-doped BSO on $LaAlO_3$ (200–640-Å-thick), and $GdScO_3$(450 Å, grey). The green dashed line corresponding to p =1.3 is shown for comparison. (c) Magnetic field (H) dependence of $-\Delta R/R^2$ (scale reversed), where R is the film sheet resistance, at various T for a 200-Å-thick BSO film on $LaAlO_3(001)$. H is along the [001] direction, perpendicular to the film surface. Solid black lines through the data points are fits to a 2D weak localization model. (d) Temperature dependence of the Thouless length, L_{Th}, extracted from fits similar to those in (c) for 200–640-Å-thick V_O-doped BSO films on $LaAlO_3(001)$ and $GdScO_3(001)$. The elastic scattering lengths, l_{el}, for these films are estimated at 10–30 Å. The green dashed lines are guides to the eye, corresponding to p = 1.3.

Even the most conductive V_O-doped BSO films ($t \geq 200$ Å) display a small upturn in ρ at the lowest T, with the upturn temperature systematically varying from 50–125 K with increasing t. To understand the origin of this low T upturn, the data in Fig. 6.3(a) has been replotted in Fig. 6.4(a) as $\rho - \rho_{min}$ *vs*. $\log(T)$, and is seen to scale linearly at low T, even down to 500 mK. This is the expected T dependence for a 2D quantum correction governed by either weak localization or electron-electron coulombic interactions. Note that the 130 Å-thick film on LAO(001) is strongly localized, showing $d\rho/dT < 0$ at all T, and is added to the data set in Fig. 6.4(a) just for comparison. Following Lee and Ramakrishnan [138], the zero field sheet conductance, $G(T)$, of such a system, taking into account both the 2D weak localization (WL) and electron-electron coulombic interaction corrections, is given by:

$$G(T) = G_0 + \frac{e^2}{2\pi^2\hbar}\left[p + \left(1 - \frac{3}{4}\widetilde{F_\sigma}\right)\right] ln\left(\frac{T}{T_0}\right)$$

(6.1).

Here, G_0 and T_0 are constants, $p/2$ is the temperature exponent of the Thouless length, and $\widetilde{F_\sigma}$ is the conductivity Fermi liquid interaction parameter. The Thouless length, L_{Th}, denotes the average distance an electron diffuses before encountering a dephasing inelastic collision. For a 2D system $L_{Th} = \left(\frac{1}{2} l_{el}\ l_{in}\right)^{1/2}$, where l_{el} and l_{in} are the elastic and inelastic scattering lengths, respectively. Although l_{el} is relatively insensitive to T, l_{in} shows a strong dependence given by: $l_{in} \propto T^{-p}$. Eq. 6.1 can be differentiated with respect to T yielding:

$$\frac{dG(T)}{dT} = \frac{e^2}{2\pi^2\hbar}\left[p + \left(1 - \frac{3}{4}\widetilde{F_\sigma}\right)\right]\frac{1}{T}$$

(6.2).

Fig. 6.4(b) plots dG(T)/dT *vs*. 1000/T for 200–640 Å-thick V_O-doped BSO films on LAO(001) and GSO(001). The overall linear dependence suggests that the data is in reasonable agreement with Eq. 6.1. Ignoring the electron-electron interaction term (*i.e*., assuming 2D WL to be the dominant effect) yields p = 1.2–1.4, reasonably close to 1.5, an expected value when the dephasing occurs by electron-electron scattering in the 'dirty' limit. This further suggests that our assumption of 2D WL being the dominant mechanism is reasonable. At low T, l_{in} can exceed l_{el} by several orders of magnitude, and an electron then undergoes multiple elastic collisions before encountering an inelastic collision that results in loss of phase coherence. The superimposition of the elastically scattered electron wave leads to backscattering as long as phase coherence persists. The resulting destructively interfering electron pathways causes an increase in ρ [138, 139].

In a system where WL dominates, a negative magnetoresistance (*MR*) is expected *vs*. out-of-plane magnetic field (H), arising from H induced suppression of backscattering. Furthermore, the rate at which *MR* changes with H depends on the magnitude of the characteristic phase coherence length scale (L_{Th} in case of WL). The functional form of the sheet conductance ($-\Delta R/R^2$) *vs*. H according to the 2D WL model is given by [138]:

$$\frac{-\Delta R}{R^2} = \frac{e^2}{2\pi^2\hbar}\left[\Psi\left(\frac{1}{2}+\frac{\hbar/4e}{L_{\mathrm{Th}}^2 H}\right) - \ln\left(\frac{\hbar/4e}{L_{\mathrm{Th}}^2 H}\right)\right] = \frac{e^2}{2\pi^2\hbar}\left[\Psi\left(\frac{1}{2}+\frac{\hbar/2e}{l_{\mathrm{el}} l_{\mathrm{in}} H}\right) - \ln\left(\frac{\hbar/2e}{l_{\mathrm{el}} l_{\mathrm{in}} H}\right)\right] \quad (6.3)$$

where Ψ is the digamma function. It is noteworthy that there is only one fitting parameter, L_{Th}, in Eqn. 6.3. On the other hand, if electron-electron coulombic interaction is the dominating mechanism, an overall positive *MR* vs. *H* is expected, the functional form being parabolic ($\propto H^2$) at low *H* and linear *vs*. *ln*(*H*) at high *H*. Fig. 6.4(c) shows the *H* dependence of the sheet conductance, expressed as $-\Delta R/R^2$, at different measurement temperatures for a 200-Å-thick V_{O}-doped BSO film on LAO(001). Note that the y-axis scale is reversed and *H* is parallel to the [001] direction. The negative *MR* values observed in the *T* range of 1.8–80 K suggests that WL is indeed the dominant mechanism. It is clear that the decrease in magnitude of the *MR* (becoming almost negligible close to T_{up} = 130 K) with increasing *T* is accompanied by broadening of the peak. Data similar to that in Fig. 6.4(c) for other films are presented in Fig. A6 of Appendix IV. Fits to these data sets in accordance with Eq. 6.3 yield the *T* dependence of L_{Th}. The 2D WL fits and the data in Fig. 6.4(c) match exceptionally well down to ~5.5 K, below which, a mismatch, that can only be corrected by a small positive *MR*, can be observed at high *H*. This positive contribution likely arises because of coulombic interactions prevailing over 2D WL at high *H*. The *T* dependence of the extracted L_{Th} values is shown in a log-log plot in Fig. 6.4(d) for four different 200–640 Å-thick V_{O}-doped BSO films. In the *T* range of 5.5–80 K, the dependences appear to be linear with a slope matching the p = 1.3 extracted in Fig. 6.4(b) from the zero field ρ *vs. T*. Below 5.5 K, where coulombic interactions become non-negligible at high *H*, a deviation from linearity is observed. Moreover, the L_{Th} values can be seen to be ≥ *t*, confirming the 2D nature of the WL. Further insight into this can be obtained through careful comparison between *MR vs*. out-of-plane and in-plane *H*. This is shown in Fig. 6.5, where *MR*(*T* = 1.8 K) *vs*. the two *H* orientations is plotted at for a 200 Å-thick V_{O}-doped BSO film on LAO(001). In the case of 2D WL, a relatively high anisotropy between the two *MR*s is expected, as an in-plane *H* is unable to suppress any backscattering of electron waves along in-plane directions. Fig. 6.5 does show a relatively

high anisotropy in *MR* between the two orientations at low fields, but this progressively weakens at high *H* as electron-electron coulombic interactions begin to contribute more.

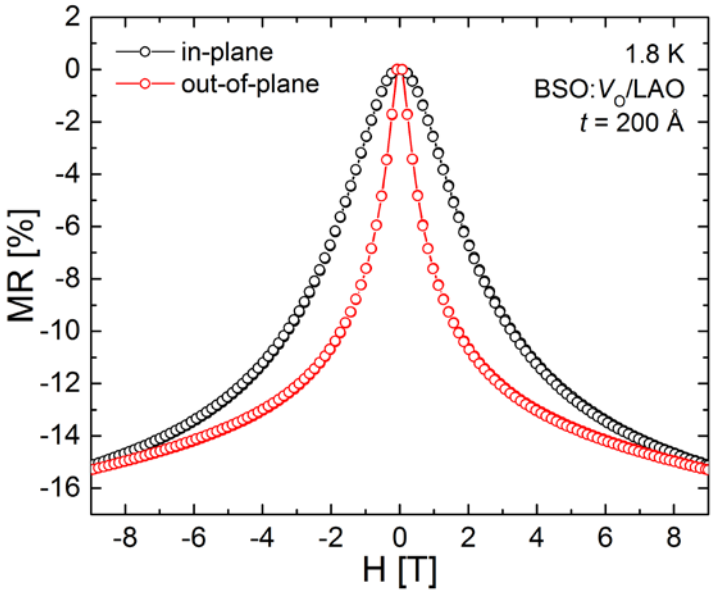

Fig. 6.5: Magnetic field (*H*) dependence of the magnetoresistance (MR), defined as $\frac{R(H)-R(H=0)}{R(H=0)} \times 100\%$, at 1.8 K for a 200 Å-thick oxygen-vacancy-doped BSO film on $LaAlO_3$(001) with field along both out-of-plane (red) and in-plane (black) directions. The data show relatively high anisotropy in MR between the two orientations at low fields, but this progressively weakens at high *H* as electron-electron coulombic interactions start dominating.

6.4 Concluding Remarks

In summary, we have studied film thickness induced insulator-metal transition (IMT) in epitaxial, phase pure, nominally stoichiometric BSO films deposited *via* high pressure oxygen sputtering on LAO(001) and GSO(001) substrates. A detailed picture of the film microstructure, including the presence of extended defects, is provided using WAXRD, GIXR, AFM, and STEM. We also present extensive temperature and field dependent transport measurements on doped BSO to probe IMT as a function of thickness and understand the mechanism responsible for low *T* upturn in resistivity of metallic-like

films. 2D weak localization has been identified as the quantum anomaly responsible for this upturn. The results provide significant insight into the crossover between dominant conduction mechanisms in BSO thin films with varying film thickness.

Chapter 7: Structure and Mobility Optimization of High-Pressure-Oxygen-Sputtered $Ba_{0.98}La_{0.02}SnO_3$ Thin Films

7.1 Chapter Overview

Here we investigate structure-electronic property correlations in 2% La-doped $BaSnO_3$ films with the goal of optimizing electron mobility. Single-phase, stoichiometric, smooth, epitaxial $Ba_{0.98}La_{0.02}SnO_3$ films were deposited on $LaAlO_3$ (LAO, -8.6% (compressive) mismatch), LSAT (-6.4% mismatch), $SrTiO_3$ (STO, -5.4% mismatch), $GdScO_3$ (GSO, -3.9% mismatch), $PrScO_3$ (PSO, -2.2% mismatch) and MgO (+2.2 (tensile) mismatch) substrates with (001) orientation. The impact of deposition temperature, growth rate, film thickness and substrate mismatch on structure and mobility was systematically studied. 300 K mobilities up to 70 $cm^2V^{-1}s^{-1}$ at $n = 2 \times 10^{20}$ cm^{-3} are obtained, even in 380-Å-thick films without any buffer layer. Important findings include a monotonic increase in mobility with deposition temperature (over the range of temperatures probed), carrier freeze-out and decreased mobility at low thickness, and, surprisingly, insensitivity to the substrate mismatch. These trends are discussed in terms of accompanying structural characterization data, particularly misfit and threading dislocation densities quantified using transmission electron microscopy.

7.2 Methods

High pressure oxygen sputter deposition was carried out from 2” dia. 2% La-doped-$BaSnO_3$ (BSO:La) targets synthesized by solid-state reaction of $BaCO_3$, La_2O_3, and SnO_2 (> 99.9 % purity) in air at 1200 °C, followed by cold-pressing and sintering at 1450 °C. Prior to growth, the substrates were annealed for 15 min in 1.9 Torr of O_2 at 900 °C. Subsequently, BSO:La films were DC sputtered with 75 – 190 mA limiting current, at deposition temperatures 750 – 900 °C, and in 1.9 Torr O_2 pressure (P_{O2}). The growth rate (2 – 10 Å/min) was controlled through changes in the DC current. Post-growth cooling was done in 600 Torr of O_2. High-resolution wide-angle X-ray diffraction (WAXRD) and

rocking curve (RC) scans were performed with Cu *K*α radiation in a Panalytical X'Pert Pro system. Cross-sectional transmission electron microscopy samples were prepared using FEI Helios Nanolab G4 dual-beam focused ion beam (FIB), where the samples were thinned using a 30 kV Ga-ion beam and further polished using a 2 kV Ga-ion beam to eliminate damaged layers at the surface. The thickness of the cross-sectional samples was in the range of 400 – 500 Å. Plan-view TEM samples were prepared by mechanical polishing using Multiprep^{TM} (Allied High Tech Products, Inc.). The plan-view sample thickness was estimated to be in the range of 500 – 700 Å *via* the electron energy-loss spectroscopy (EELS) log-ratio method using a calculated mean free path of plasmon excitation in BSO of λ_p = 810 Å [64, 123]. Scanning transmission electron microscope (STEM) imaging was carried out using an aberration-corrected FEI Titan G2 60-300 STEM at 200 keV with ~30 pA beam current. The convergent semi-angle of the incident STEM probe was 17.2 mrad and the annular dark-field (ADF) detector inner angles were 19 mrad, 55 mrad, and 93 mrad for low-angle ADF (LAADF), medium-angle ADF (MAADF), and high-angle ADF (HAADF) images, respectively. High-magnification ADF-STEM images were filtered using 'HRTEM Filter' in Gatan Digital Micrograph software to remove amorphous components in the images [64]. Temperature and magnetic field dependent electronic transport measurements (DC, 1.8–300 K, 0 – 9 T) were carried out in Quantum Design Physical Property Measurement Systems (PPMSs) using indium contacts in a van der Pauw geometry. All such contacts were Ohmic at the current densities used during the measurements.

7.3 **Results and Discussion**

7.3.1 **Influence of Deposition Temperature**

To investigate the influence of deposition temperature (T_{dep}) on the structural and electronic transport properties of BSO:La (x = 0.02) films, we performed growths at 750 °C, 800 °C, 850 °C, and 900 °C. During each growth, films were simultaneously deposited onto LAO(001), LSAT(001), STO(001), and MgO(001) substrates. Figs. 7.1(a,c,e,g) show

the WAXRD scans around the 002 reflections for all the ~840-Å-thick BSO:La films in this series. During these depositions, the DC current (I_{dc}) and P_{O2} were held constant at 150 mA and 1.9 Torr, respectively, resulting in a growth rate of ~7.3 Å/min. Only 002 substrate and film peaks are observed in Figs. 7.1(a,c,e,g), suggesting phase-pure and epitaxial (out-of-plane) BSO:La films on all substrates. Note that the small peak appearing sporadically in between the film and substrate peaks in Figs. 7.1(c,e,g) is actually a hybrid reflection from multiple X-ray scattering events in the film and/or substrate [140]. WAXRD in conjunction with asymmetric non-specular reciprocal space maps (see Fig. A7 in Appendix V) confirms cube-on-cube epitaxy. Based on the 002 film peak intensity (relative to the substrate) and observation of finite size fringes around the film peak it is clear that the film structural quality is superior for BSO:La films grown on perovskite substrates: STO, LSAT, and LAO compared to those on MgO for all deposition temperatures. Films deposited on MgO (rock salt crystal structure) show broader, lower intensity peaks, indicating poorer crystallinity. This finding emphasizes the importance of symmetry matching in perovskite oxide epitaxy. While the 002 BSO peak (normalized to the substrate) intensifies with increasing T_{dep} in films deposited on MgO (suggesting an improvement in crystallinity), no such improvement is apparent for films grown on perovskite substrates.

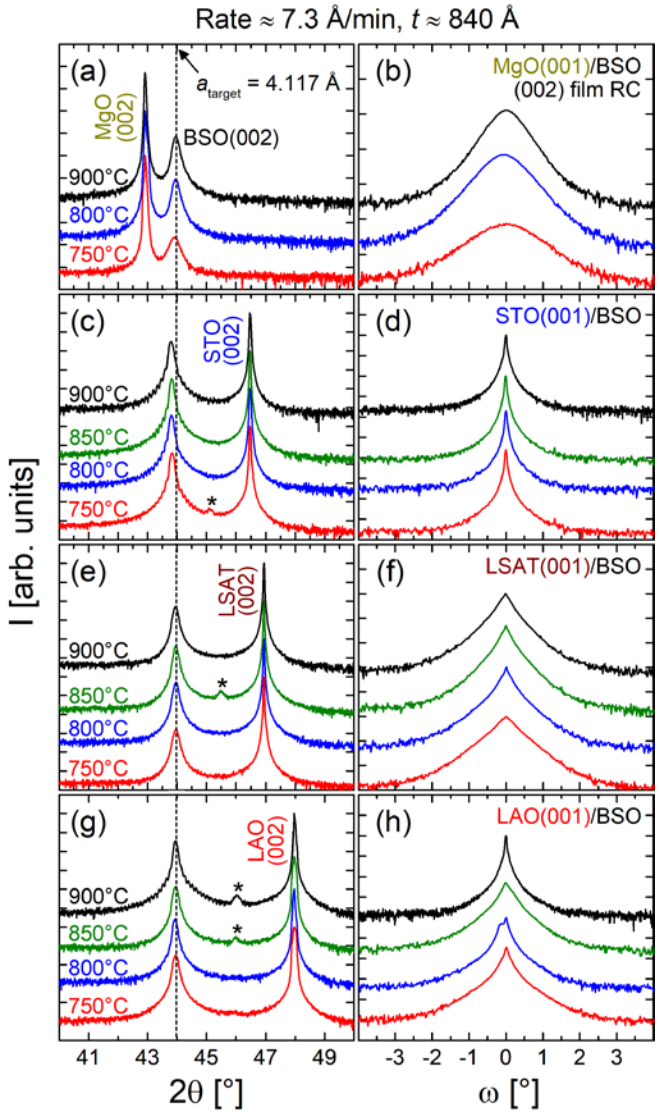

Fig. 7.1: High-resolution WAXRD of ~840-Å-thick BSO:La films sputtered at 750 – 900°C deposition temperature. Shown are θ-2θ coupled scans around the 002 substrate and film reflections (left panels) and complimentary rocking curves through the 002 film reflection (right panels) for films grown on (a, b) MgO(001), (c, d) STO(001), (e, f) LSAT(001), and (g, h) LAO(001). All figures are plotted on a semi-log scale. Deposition temperatures are shown aside each curve on the left panels. The dashed line indicates the bulk lattice parameter of the sputtering target. The peaks marked with an asterisk (only observed in some cases) are due to hybrid reflections [140]. All films were deposited at ~7.3 Å

Figs. 7.1(b,d,f,h) plot the RCs (ω scans) through the 002 BSO reflections of each film shown in Figs. 7.1(a,c,e,g). Note, all these RCs appear wide in general because of the semi-log nature of these plots. For STO(001)/BSO:La films, the RCs appear nearly identical to each other across all deposition temperatures and readily fit to a single Lorentzian function with full-width at half-maximum (FWHM) ~0.04°, similar to that of the substrate. In contrast, MgO(001)/BSO:La films, and to a lesser extent LSAT(001)/BSO:La and LAO(001)/BSO:La films, display broader RCs, but the peaks progressively become narrower with increasing T_{dep}. This signifies a reduction in the out-of-plane mosaicity possibly due to a reduction in line defect density.

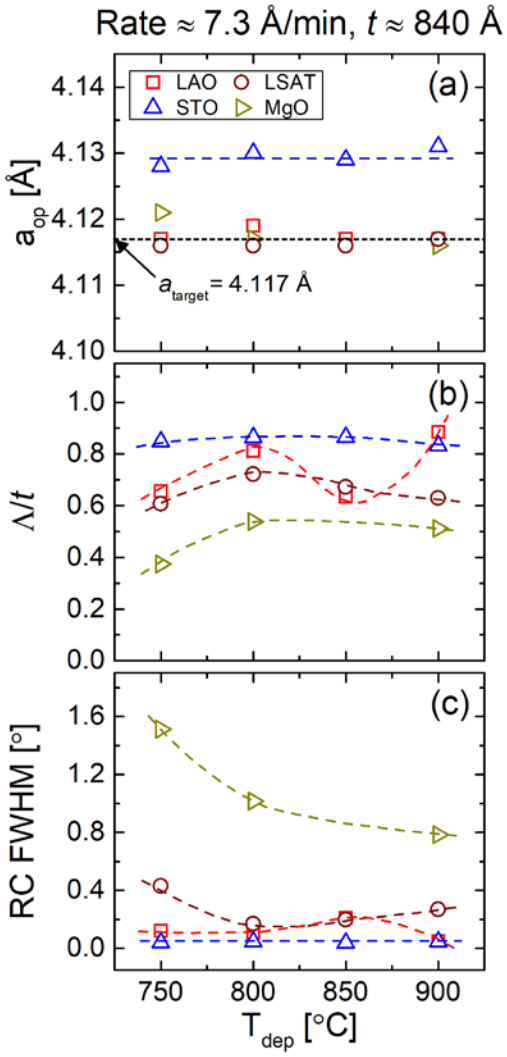

Fig. 7.2: Deposition temperature (T_{dep}) dependence of structural parameters determined from WAXRD and RC scans. (a) Out-of-plane lattice parameter, a_{op}, (b) Scherrer length-to-film-thickness ratio, Λ/t, and (c) film 002 RC FWHM for BSO:La films on four different substrates (see legend). The dashed black line in (a) indicates the bulk lattice parameter of the sputtering target, while all other dashed lines are guides to the eye. All films are ~840 Å thick and grown at ~7.3 Å/min.

Figs. 7.2(a–c) summarize the T_{dep} dependence of the structural parameters: out-of-plane lattice parameter (a_{op}), Scherrer length-to-film-thickness ratio (Λ/t), and RC FWHM extracted for all the films shown in Fig. 7.1. Λ was estimated from the FWHM of the 002 WAXRD film peak *via* the Scherrer equation (Eq. 2.3 in Chapter 2). For BSO:La films grown on LSAT, LAO, and MgO the determined values for a_{op} are in good agreement with the 4.117 Å bulk lattice parameter of the sputtering target (see Chapter 3). However, for the films grown on STO, a_{op} values are slightly expanded (by ~0.01 Å). This expansion in a_{op}, observed in all films deposited on STO in this work as well as in some other reports [94, 96], is possibly due to a small amount of residual strain. For all T_{dep}, the films on STO show greater Λ/t ratios (~0.85) than on any of the other substrates (Fig. 7.2(b)). The films on MgO, on the other hand, show Λ/t ratios ≤ 0.5, indicating significant microstrain from defects. Fig. 7.2(c) shows the trends in (002) RC FWHM of the films as a function of T_{dep}. It is clear that the RC FWHM for MgO(001)/BSO:La films decreases significantly with increasing T_{dep}. Even at the highest T_{dep}, however, films on MgO still exhibit much broader RCs than for the films on the perovskite substrates. RC FWHM for LSAT(001)/BSO:La films also shows an initial decrease with increasing T_{dep} from 750 – 800 °C, but remains fairly constant above 800 °C. This decrease in 002 RC FWHM corresponds to a reduction of the out-of-plane mosaicity in the films deposited at higher temperatures. RC FWHMs for films grown on STO and LAO are ~0.04° and ~0.12°, respectively, and do not vary much with T_{dep}.

Fig. 7.3 presents a summary of the 300 K transport properties: resistivity (ρ), Hall electron density (n), and Hall electron mobility (μ) *vs.* T_{dep} for the ~840-Å-thick BSO:La

films in this series. Fig. 7.3(a) shows that ρ in all films drops monotonically with increasing T_{dep}, before apparently saturating at ~0.4 mΩcm at T_{dep} = 900 °C regardless of the substrate. The most significant improvements with T_{dep} occur in MgO(001)/BSO:La films, where an almost 10^3-fold decrease in ρ is observed with increasing T_{dep} from 750 °C to 900 °C. The decrease in ρ with increasing T_{dep} is concurrent with an increase in both n (Fig. 7.3(b)) and μ (Fig. 7.3(c)). Above T_{dep} = 800 °C, n for all films is around 3×10^{20} cm^{-3}, indicating near 100% La dopant activation (theoretically, 2.86×10^{20} cm^{-3} for 2% La substitution) and negligible compensation. At deposition temperatures below 800 °C, however, n drops to $1.3 – 2.2 \times 10^{20}$ cm^{-3}, significantly below the expected value, indicating insufficient dopant activation or compensation from defects. Like n, μ also shows an increasing trend *vs*. T_{dep}, either due to improvement in the structural quality of the films or reduction in dislocation scattering due to screening (μ increases with n, as discussed in Chapter 5). At T_{dep} = 900 °C, however, all μ values converge to ~50 $cm^2V^{-1}s^{-1}$, irrespective of any mismatch (in both lattice size and symmetry). Fig. 7.3(c) also suggests that there is scope for further improvement in μ at higher deposition temperatures, or possibly by post-growth thermal annealing.

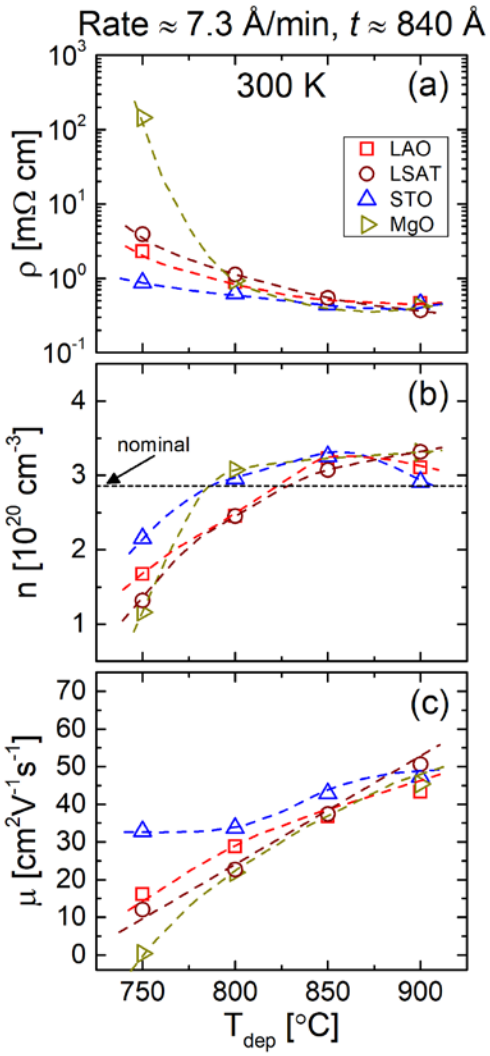

Fig. 7.3: Dependence of electronic transport properties, (a) resistivity, ρ, (b) Hall electron density, *n*, and (c) Hall electron mobility, μ, on deposition temperature (T_{dep}) for BSO:La films grown on four different substrates (see legend). All measurements were conducted at 300 K. The black dashed line in (b) represents the nominal electron density, corresponding to 100% La_{Ba} dopant activation, while all other dashed lines are guides to the eye. All films are ~ 840 Å thick and grown at ~7.3 Å/min.

The findings in this section demonstrate the positive influence of higher deposition temperature on the structural and electronic transport properties of BSO:La epitaxial films.

For films deposited on symmetry mismatched MgO significant improvement in crystallinity was observed at higher T_{dep}. Electronic transport properties were seen to significantly improve for films across all four substrates with an increase in T_{dep}. Additionally, our data suggest that further improvement of μ is possible by utilizing deposition temperatures above 900 °C. Due to instrument limitations, this was not possible in the present work. Therefore, a deposition temperature of 900 °C was adopted for growing BSO:La films throughout the rest of this study. Finally, the positive trends for film ρ, *n*, and μ with increasing growth temperature support the idea that post-growth thermal annealing may prove to be useful in further improvement of mobility in doped BSO epitaxial films.

7.3.2 **Influence of Film Thickness**

After the results of the last section established 900 °C as the optimal deposition temperature for BSO:La films, probing the influence of epilayer thickness (*t*) was the next logical step in the optimization of μ. In this series, 100 – 2000-Å-thick BSO:La (x = 0.02) films were grown with T_{dep} = 900 °C on LAO(001), STO(001), GSO(001), and PSO(001) substrates, thus spanning a wide range in mismatch from -2.2% (PSO) to -8.7% (LAO). Two separate thickness series of films, deposited at 8 Å/min and 2.5 Å/min, will be discussed in this section. Figs. 7.4(a,c,e,g) shows the high resolution WAXRD around the 002 reflections for all films deposited at ~8 Å/min. The different colored curves represent films of different thickness, grouped by the average thickness recorded for each growth. As expected, with an increase in *t*, the 002 BSO peaks for films on all substrates become narrower and more intense, and the spacing of the Kiessig fringes decreases. The films grown on the scandate substrates (GSO and PSO) show slight shifts in the film peak position toward higher angles with increasing *t*, consistent with strain relaxation. This trend is most clear in films deposited on PSO, where the lattice mismatch is only 2.2%. Figs. 7.4(b,d,f,h) show the corresponding RCs through the 002 film WAXRD peaks for all the films shown in Figs. 7.4(a,c,e,g). At low thicknesses (≤ 300 Å) the RC peak closely fits to a convolution of two peaks: one broad and one narrow. This phenomenon can be seen

across all four substrates at low *t*. As *t* is increased, however, the RC shapes evolve to fit a single narrow peak on all the substrates except LAO. For films grown on LAO, the transition at high thickness appears to favor a single broad peak rather than a narrow one.

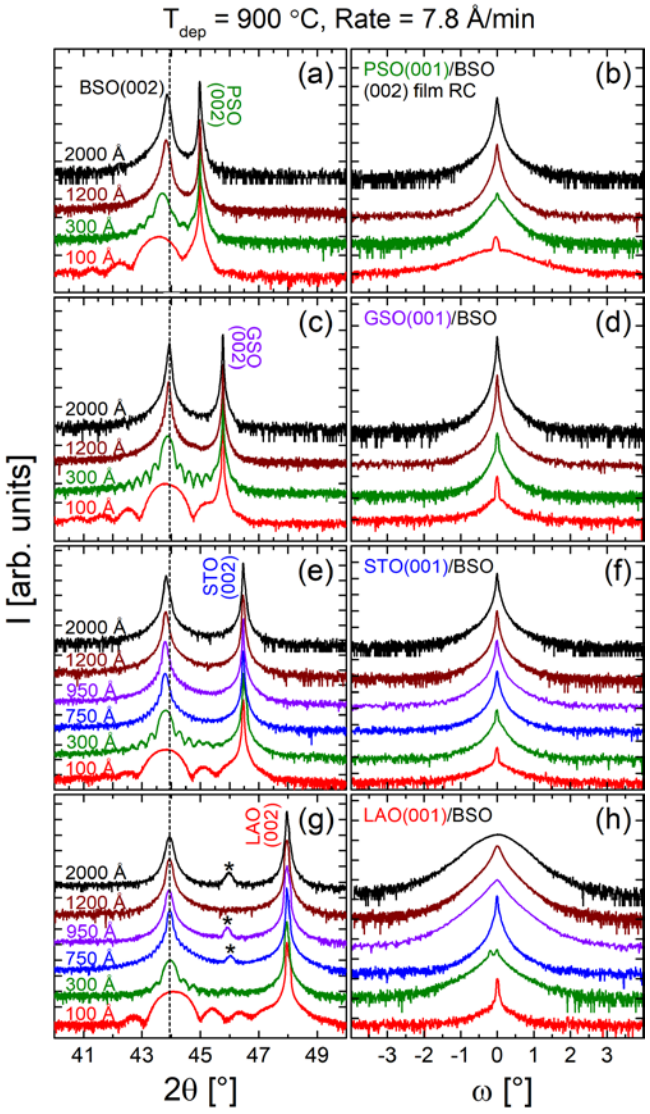

Fig. 7.4: High resolution WAXRD of 100–2000-Å-thick BSO:La films deposited at 900°C and ~7.8 Å/min. Shown are θ–2θ coupled scans of the film/substrate 002 peaks (left panels) and complimentary 002 film rocking curves (right panels) for films grown on (a, b) PSO(001), (c, d) GSO(001), (e, f) STO(001), and (g, h) LAO(001). Peaks marked with an

asterisk arise from hybrid reflections [140]. The dashed line indicates the bulk lattice parameter of the sputtering target.

Fig. 7.5 shows the t dependence of the film structural parameters: a_{op}, Λ/t, RC FWHM, and the normalized intensity of the narrow RC component (I_{narrow} / I_{total}) for all the films in this thickness study that were deposited at 8 Å/min. A similar dataset for the films deposited at 2.5 Å/min can be found in Fig. A8 of Appendix V. The overall trends in both the datasets are quite similar, although the range of t probed at 2.5 Å/min was comparatively smaller because of concerns over long growth times. The out-of-plane lattice parameter, shown in Fig. 7.5(a) for BSO:La films grown on LAO and STO, does not show any variation with increasing t. Films on LAO exhibit a_{op} close to the bulk value for BSO consistent with fully relaxed films, whereas films on STO show a_{op} around 4.130 Å, regardless of thickness. The expanded a_{op} on STO is likely due to some residual strain, as can be inferred from an asymmetric non-specular reciprocal space map (RSM) of the thickest (2000 Å) film grown on STO. The RSM around the 013 reflection yields an a_{op} of ~4.127 Å, but a compressed in-plane lattice parameter ~4.107 Å. For the films grown on lower mismatched scandate substrates, however, the t dependence of a_{op} is clearly indicative of strain relaxation. The out-of-plane lattice parameters in these films show a decrease with t; a_{op} is expanded at low t but appears to relax toward the bulk value with increasing t. Fig. 7.5(b) shows that the extracted value for Λ/t decreases for films on all substrates, from close to 1 for very thin films, to < 0.6 for films around 2000 Å. This behavior is due to the increasing dominance of microstrain on the Scherrer broadening with increasing t.

In Figs. 7.5(c,d), the trends that can be seen in the RCs have been quantified and presented in the form of the FWHM (broad and narrow component where applicable) and normalized intensity of the RC narrow component (I_{narrow} / I_{total}), plotted *vs*. t. From Figs. 7.5(c) and (d), it is clear that the broad RC component is no longer discernible above 300 Å for all films except those grown on LAO. Moreover, the FWHM values of the narrow RC component are consistently around 0.05°, close to the substrate RC, for all thicknesses

and across all substrates (excluding thick, >1200 Å films on LAO). For films grown on LAO, the trend observed in the RCs is quite the opposite to that of the other substrates, where the narrow component progressively diminishes in intensity at high t, eventually disappearing above 1200 Å. This dichotomy in the RC behavior is more clearly seen in Fig. 7.5(d), where I_{narrow} / I_{total} vanishes for films with $t \geq 1200$ Å on LAO. At the highest thickness probed, ~2000 Å, the film on LAO, in fact, exhibited a very broad RC peak, with FWHM of 0.92°, whereas for the films on the other three substrates the average RC FWHM was only 0.04°. This peculiar observation suggests the presence of some defect only in thick films deposited in LAO, which vastly increases the out-of-plane mosaicity.

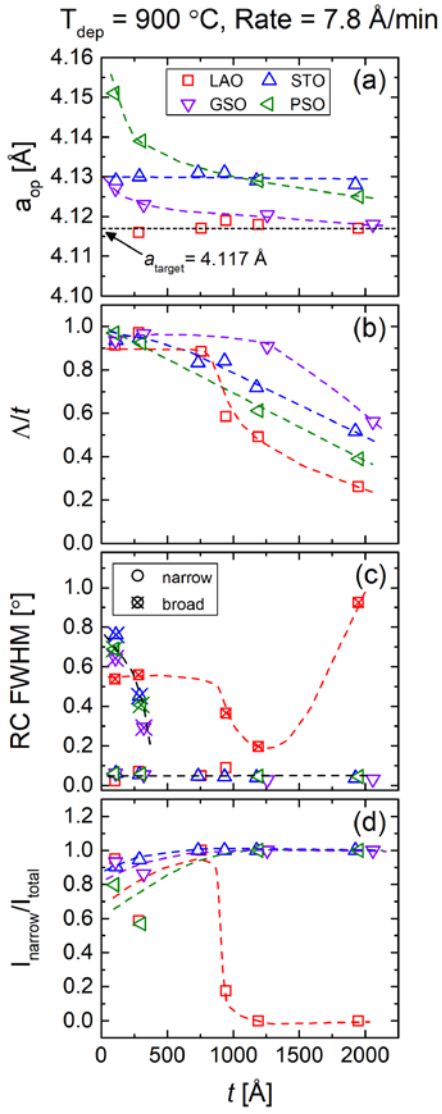

Fig. 7.5: Thickness (t) dependence of structural parameters determined from WAXRD. (a) The out-of-plane lattice constant, a_{op}, (b) Scherrer length-to-film-thickness ratio, Λ/t, (c) film 002 RC FWHM, and (d) intensity ratio, I_{narrow}/I_{total}, of 002 film RC (RCs exhibit both broad and narrow components). The dashed line in (a) indicates the bulk lattice parameter of the sputtering target, while all other dashed lines are guides to the eye. All films were deposited at 900°C and ~7.3 Å/min.

To investigate the defect structure in BSO:La films, cross-sectional and plan-view STEM were performed. Fig. 7.6 presents the cross-sectional HAADF and LAADF images of 2000-Å-thick BSO:La films deposited at 8 Å/min on LAO (Figs. 7.6(a–c)), STO (Figs. 7.6(d–f)), GSO (Figs. 7.6(g–i)), and PSO (Figs. 7.6(j–l)). The low magnification HAADF-STEM images in Figs. 7.6(a,d,g,j) show uniform film thickness and smooth surfaces over a large lateral length scale, sharp film/substrate interfaces, and vertical contrast arising from small-angle boundaries (between slightly misoriented grains) in all the films. The LAADF images shown in Figs. 7.6(b,e,h,k) also show similar but much more pronounced vertical contrast from small-angle boundaries. This is because, compared to HAADF, LAADF imaging is more sensitive to the strain arising from the accumulation of threading dislocations at these small-angle boundaries. The columnar grain structures (~300 Å in size) in the films show in-plane twists (~1.6°) for all four films but out-of-plane tilt only in the film grown on LAO [141]. Figs. 7.6(c,f,i,l) are high magnification atomic resolution HAADF-STEM images acquired from regions close to the film/substrate interface for the film on LAO (Fig. 7.6(c)), STO (Fig. 7.6(f)), GSO (Fig. 7.6(i)), and PSO (Fig. 7.6(l)). These images show atomically sharp interfaces as well as quite evenly spaced misfit edge dislocations (yellow symbols) with Burgers vector $\boldsymbol{b} = a_{BSO}[100]$ or $a_{BSO}[010]$ in all films. The spacing between these misfit dislocations (MDs) averaged over multiple images is in good agreement with theoretically predicted spacing for all the shown film-substrate combinations, as can be seen in Table 7.1.

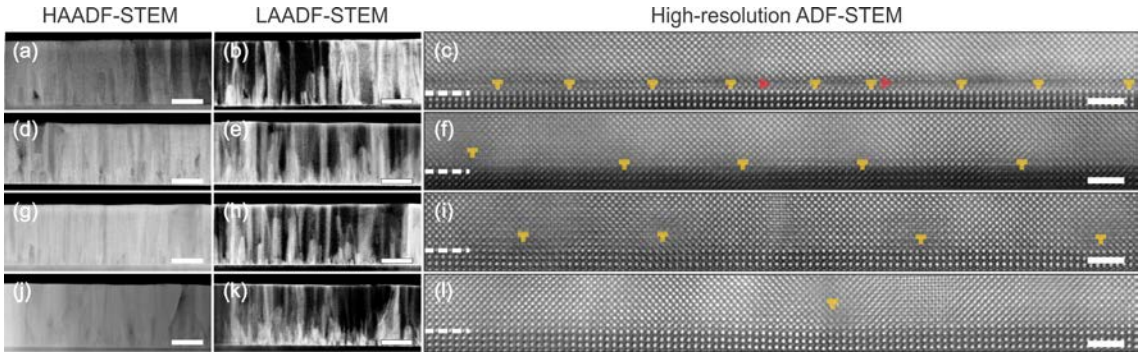

Fig. 7.6: Cross-sectional HAADF- and LAADF-STEM images of 2000 Å-thick BSO:La films grown on (a,b) $LaAlO_3$(001), (d,e) $SrTiO_3$(001), (g,h) $GdScO_3$(001), and (j,k) $PrScO_3$(001). High-resolution ADF-STEM images of the film/substrate interface for 2000 Å-thick BSO:La films on (c) $LaAlO_3$, (f) $SrTiO_3$, (i) $GdScO_3$, and (l) $PrScO_3$. MDs with an in-plane burgers vector are marked with yellow symbols and MDs with an out-of-plane burgers vector are marked with red symbols. Scale bars in (c), (f), (i), and (l) are 20 Å. All other scale bars are 1000 Å.

The BSO:La/LAO interface shows a distinct dark contrast on the BSO side, immediately above the atomically sharp interface. A high density of MDs formed at this interface is most likely the origin of this contrast. In addition to the MDs with $\boldsymbol{b} = a_{BSO}[100]$ or $a_{BSO}[010]$, this interface also shows the unusual presence of dislocations with Burgers vector along the [001] direction (red symbols). These dislocations are responsible for the out of plane tilt in the grains, resulting in an overall increase in the out-of-plane mosaicity. It can quantitatively be shown that the presence of one such dislocation in a ~300 Å grain can result in an out-of-plane tilt of ~0.8° [141]. This value is remarkably close to the RC FWHM for this film (shown in Fig. 7.5(d)). However, the presence of these $a_{BSO}[001]$ dislocations is quite puzzling, and further work is necessary to understand their origin in thick films grown on LAO.

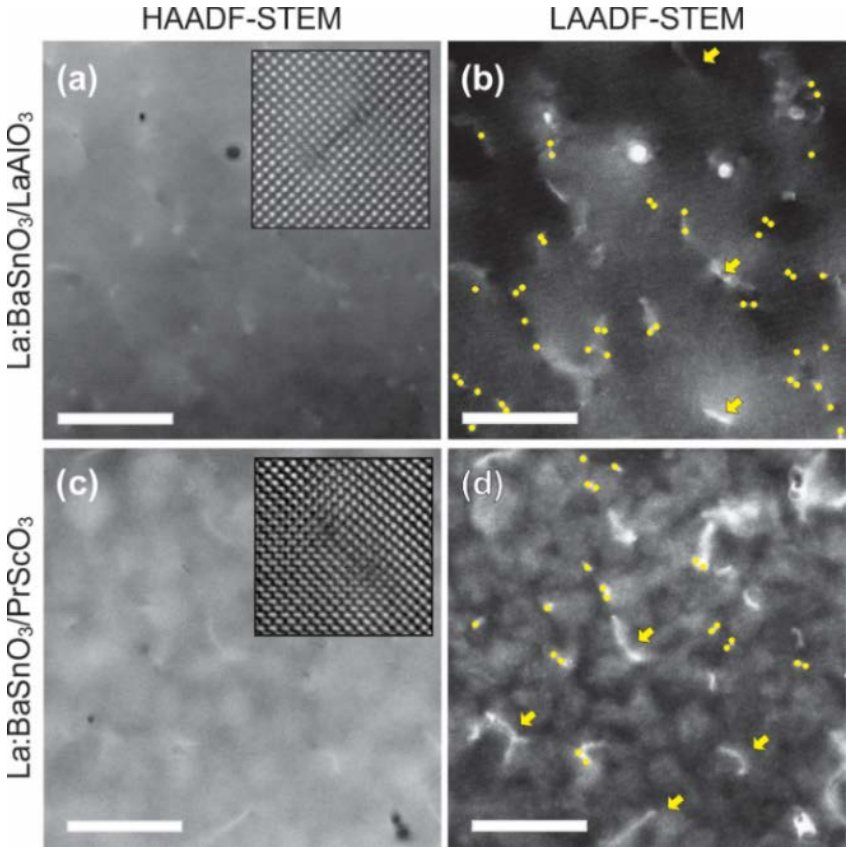

Fig. 7.7: Plan-view HAADF- and LAADF-STEM images of 2000 Å-thick BSO:La films grown on (a,b) $LaAlO_3$(001) and (c,d) $PrScO_3$(001). (Inset: magnified HAADF-STEM images of TDs connected *via* a short stacking fault.) TDs are marked with small dots in LAADF-STEM images. Yellow arrows in LAADF-STEM images are bright contrast from misoriented grains. All scale bars are 500 Å.

Plan-view STEM was done to image the threading dislocations (TDs) and estimate their densities in these films. Fig. 7.7 shows plan-view HAADF (Fig. 7.7(a,c)) and LAADF (Fig. 7.7(b,d)) images of 2000-Å-thick BSO:La films deposited on LAO and PSO. HAADF-STEM images show arrays of TDs (near the small-angle grain boundaries) with in-plane Burgers vectors. These dislocations are responsible for the in-plane mosaicity (twist) in the films [57]. The TDs show bright strain contrast in the LAADF images highlighted by the yellow dots in Figs. 7.7(b) and (d). We estimated the TD density in the

films grown on LAO (-8.4% mismatch) and PSO (-2.2% mismatch) by counting the number of bright point-contrasts in LAADF images acquired from multiple different regions in the films. The estimated TD densities, listed in Table 7.1, are surprisingly close for both the films: within a factor of 2, despite there being an order of magnitude difference in MD density. Despite the large difference in lattice mismatch in the two cases, the TD densities are observed to be very similar, suggesting that there is no one-to-one correlation between the MD and TD dislocation densities in BSO:La films. So, contradictory to common belief, the TDs in BSO do not necessarily nucleate from the MDs.

Table 7.1: Spacing and density of MDs and TDs in BSO:La films. The average spacing between MDs is represented by the number of BSO unit cells ($u.c._{BSO}$). The total distance used to evaluate experimental spacing and density of MDs were 260 nm, 80 nm, 400 nm, and 50 nm for BSO:La films deposited on $LaAlO_3$(001), $SrTiO_3$(001), $GdScO_3$(001), and $PrScO_3$(001), respectively. TD densities were estimated from plan-view ADF-STEM images. The total areas used for estimation were 0.4 μm^2 and 0.1 μm^2 for $LaAlO_3$(001)/BSO:La and $PrScO_3$(001)/BSO:La, respectively.

	LAO/BSO:La	STO/BSO:La	GSO/BSO:La	PSO/BSO:La
MD spacing (theo.) ($u.c._{BSO}$)	11.5	18.2	26.5	41.0
MD spacing (expt.) ($u.c._{BSO}$)	11.3 ± 0.6	19.4 ± 1.17	25.4 ± 2.6	48.5 ± 14.5
MD density (theo.) (10^{11} cm^{-2})	44	17	8.5	3.5
MD density (expt.) (10^{11} cm^{-2})	47 ± 5.2	15.8 ± 1.8	9.3 ± 1.7	3.1 ± 1.8
TD density (expt.) (10^{11} cm^{-2})	1.8	--	--	0.87

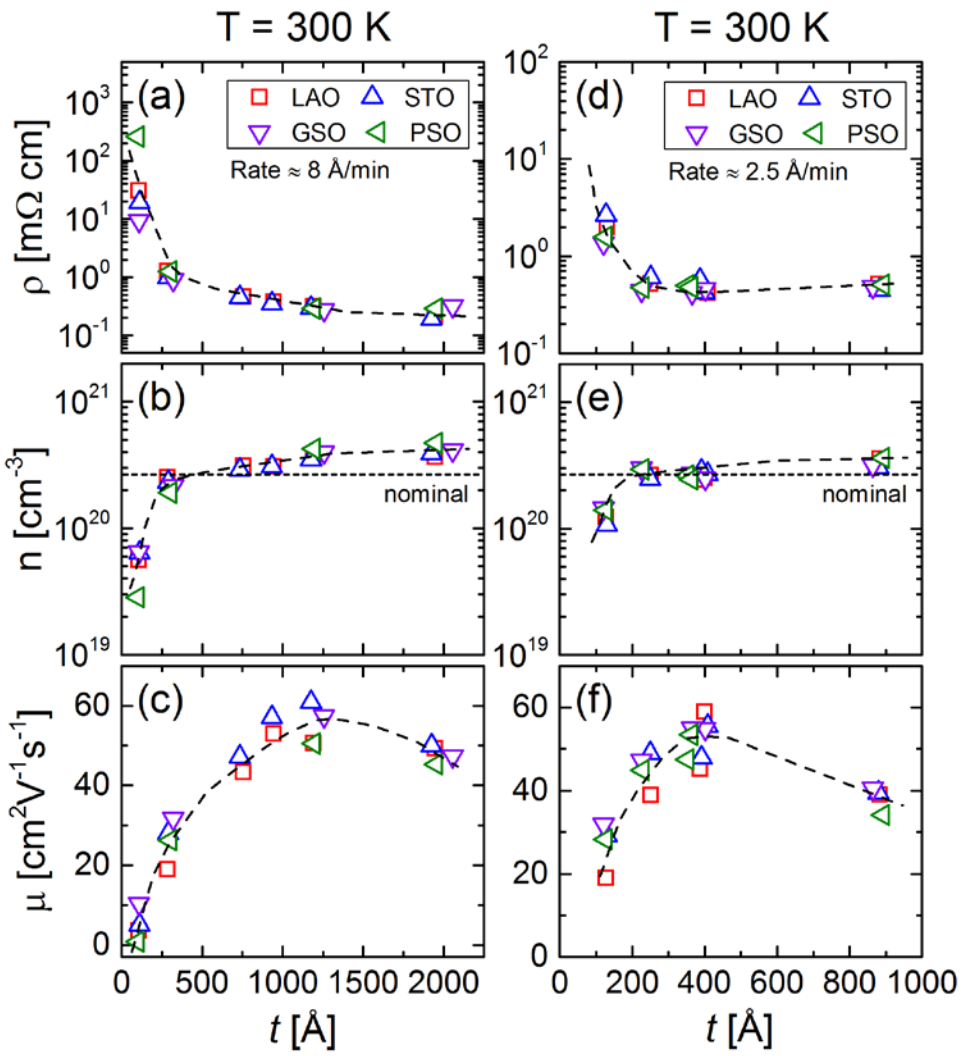

Fig. 7.8: Thickness (*t*) dependence of transport properties for BSO:La films deposited at two growth rates (T_{dep} = 900 °C). In the left panels, (a) resistivity, ρ, (b) Hall electron density, *n*, and (c) Hall electron mobility, μ, *vs*. *t* are shown for rates ~8 Å/min, and in the right panels (d) ρ, (e) *n*, and (f) μ *vs*. *t* are shown for rates ~2 Å/min. All measurements were conducted at 300 K. Films were deposited on $LaAlO_3$, $SrTiO_3$, $GdScO_3$, and $PrScO_3$ (001) oriented substrates (see legend). The black dashed line in (b) and (e) represent the nominal electron density, corresponding to 100% La_{Ba} dopant activation. All other dashed lines serve as guides to the eye.

Having thoroughly characterized the structural properties, we performed detailed temperature and field dependent transport measurements on these films. Fig. 7.8 shows the *t* dependence of the 300 K electronic transport properties (ρ, *n*, and μ) for BSO:La films deposited at two different growth rates: 8 Å/min (Figs. 7.8(a–c) and 2.5 Å/min (Figs. 7.8(d–e). Figs. 7.8(a) and (d) show a monotonic decrease in ρ with increasing *t*, for films deposited at both growth rates on all four substrates. While films deposited at 8 Å/min display a reduction in ρ of at least 2 orders of magnitude as *t* increases from 100 Å to 2000 Å, films deposited at 2.5 Å/min only show a ~3-5 fold decrease as *t* increases from 100 Å to 900 Å. When *t* is ≥ 300 Å, the ρ values in films deposited at 8 Å/min are strikingly similar on all four substrates and saturate to a value of ~0.2 mΩcm above a film thickness of 1200 Å. However, when *t* is < 300 Å, a significant variation in ρ is observed in these films depending on the substrate. Films deposited at 2.5 Å/min, on the other hand, display ρ values that are similar across all four substrates. In these films, increasing *t* results in a small initial decrease in ρ values, followed by saturation at ~0.5 mΩcm above $t \approx 250$ Å. The origin of the trends in ρ can be better understood by inspecting the trends in *n* and μ *vs*. *t*, as shown in Figs. 7.8(b,e) and (c,f), respectively. When $t \geq 250$ Å, the electron densities measured for the BSO:La films (both growth rates) are very close to the value predicted for 100% La dopant activation. For film thicknesses below 250 Å, *n* decreases rapidly with decreasing *t*. For *t* = 100 Å, *n* is roughly a factor of 3 (2.5 Å/min) or 5 (8 Å/min) below the La doping level, indicating significant electron compensation by defects or depletion from the surface/interface. Figs. 7.8(c) and (f) plot the 300 K electron mobility *vs*. *t* for films deposited at 8 Å/min and 2 Å/min, respectively. The mobility steadily increases with increasing *t* up to an apparent maximum around 50-60 $cm^2V^{-1}s^{-1}$ occurring at ~400 Å (2.5 Å/min) and ~1200 Å (8 Å/min), and then shows a downward trend. Again, all the films appear to follow the same curve regardless of which substrate they were grown on. This is likely because of similar TD densities in these films. Through careful analysis of TEM images, we found that although the MD density varies by a factor of ~10 moving from films grown on LAO to that of PSO, the TD density only var

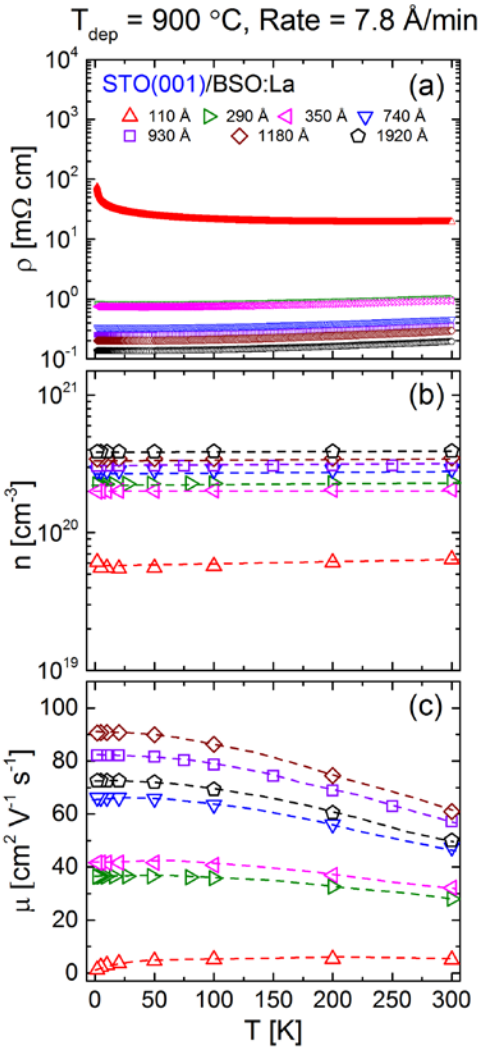

Fig. 7.9: Measurement temperature (*T*) dependence of transport properties (a) resistivity, ρ, (b) Hall electron density, *n*, and (c) Hall electron mobility, μ, for 100–1920-Å-thick BSO:La films grown on STO(001) substrates. All films were deposited at ~8 Å/min.

Detailed temperature (*T*) dependence of ρ (log scale), *n* (log scale), and μ for five BSO:La films with *t* between 100 Å and 1920 Å deposited at 8 Å/min on STO(001) substrates are exclusively shown in Fig 7.9. Similar plots for films deposited at 8 Å/min on LAO, GSO, and PSO can be found in Figs. A9, A10, A11 of Appendix V, respectively. The data for films on STO are discussed here as a representative example. Fig. 7.9(a) shows

that the 10^2-fold decrease in ρ(300 K) with increasing *t* is amplified (becomes ~10^3 fold) at low *T*. Although all films show metallic behavior (dρ/d*T* > 0) upon cooling from 300 K, for $t \leq 350$ Å, upturns in ρ(*T*) occur at low temperatures. The upturn temperature (T_{up}) is as high as 240 K in the 100-Å-thick film. This is attributed to weak localization effects as discussed in the last chapter. Figs. 7.9(b) and (c) show the trends in *n*(*T*) and μ(*T*) *vs*. *t*, respectively. For all film thicknesses, *n* is essentially independent of *T*, indicating degenerate doping in the films. However, the 100-Å-thick film shows a significantly low *n*(*T*) compared to the rest, possibly due to compensation or surface/interface depletion of electrons. For $t > 100$ Å, μ(*T*) increases upon cooling, down to ~50 K, below which it either shows saturation ($t > 350$ Å) or a small decrease (100 Å $< t \leq 350$ Å), indicating a competition between phonon scattering and defect scattering. As *t* is decreased to 100 Å, μ(*T*) shows a monotonic decrease upon cooldown, suggesting the dominance of defect scattering. It is possible that the electronic disorder in the films increases with decreasing *t*, leading to decrease in μ. The maximum (low *T*) value of μ(*T*) observed in these films is 90 $cm^2V^{-1}s^{-1}$.

7.3.3 **Influence of Growth Rate**

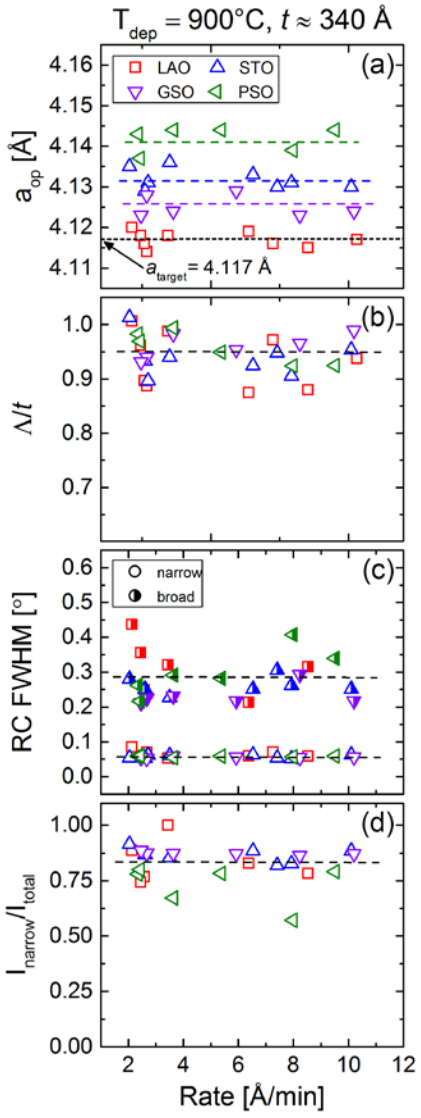

Fig. 7.10: Rate dependence of XRD determined structural parameters: (a) out-of-plane lattice constant, a_{op}, (b) Scherrer length-to-film-thickness ratio, Λ/t, (c) film 002 RC FWHM, and (d) intensity ratio, I_{narrow} / I_{total}, of 002 film RC (RC's exhibited both broad and narrow components). The dashed line in (a) indicates the bulk lattice parameter of the sputtering target, while all other dashed lines are guides to the eye. All films were deposited at 900°C and are ~ 330 Å thick.

Finally, he impact of varying deposition rate on film structural parameters, a_{op}, Λ/t, RC FWHM, and I_{narrow} / I_{total}, is summarized in Fig. 7.10. The raw data used to extract these parameters can be found in Fig. A12 in Appendix V. As in the previous results of this chapter, a_{op} for BSO:La films on LAO is consistently found to be near the bulk value of the sputtering target, as indicated by the dashed line in Fig. 7.10(a). On the other hand, films on the other three substrates again show slightly expanded out-of-plane lattice parameter. As can be clearly seen in Fig. 7.10(a), the rate of film deposition was found to have no observable impact on the film's out-of-plane lattice parameter. Figs. 7.10(b,c,d) show that the parameters Λ/t, RC FWHM, and I_{narrow} / I_{total} also lack any dependence on the deposition rate and show no significant differences between films on different substrates (hence the single flat dashed lines). In these 340-Å-thick films the amount of microstrain is minimal and the RCs, although composed of two components, are dominated mostly by the narrow component.

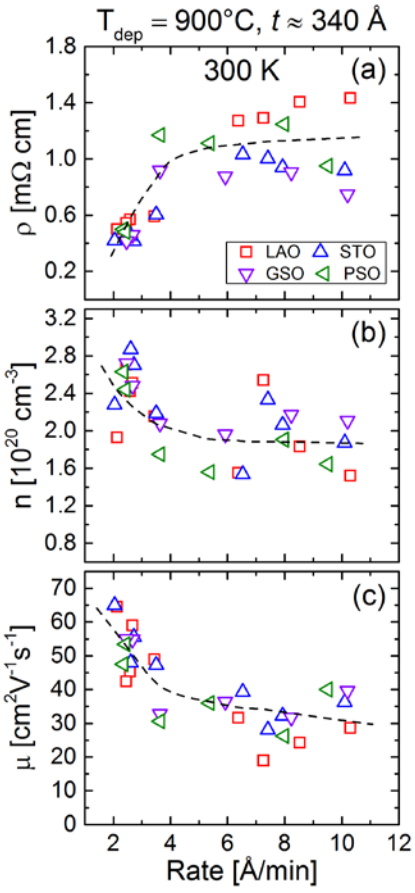

Fig. 7.11: Dependence of transport properties, (a) resistivity, ρ, (b) Hall electron density, *n*, and (c) Hall electron mobility, μ, on deposition rate for BSO:La films grown on four different substrates (see legend). All measurements were conducted at 300 K. All films were deposited at 900°C and ~ 340 Å thick. Dashed lines are guides to the eye.

While characterization *via* XRD (Fig. 7.10) showed no obvious trends in structure with deposition rate, the transport properties, on the other hand, clearly show increasing trends in conductivity (1/ρ), *n*, and μ with decreasing rate. As can be seen from Fig. 7.11(a), ρ decreases with decreasing rate for BSO:La films on all four substrates. At higher rates, ≥ 5 Å/min, relatively little change is seen in ρ for films on each substrate, albeit with different starting points (films on GSO and STO show the lowest ρ). However, at lower rates, < 5 Å/min, ρ begins to decrease, and eventually converges to a value close to 0.4 mΩcm for films on all four substrates. This decrease in ρ at low rates is accompanied by an increase in Hall electron density, *n*, and Hall electron mobility, μ, shown in Fig. 7.11(b) and 7.11(c), respectively. This observation is likely due to a reduced concentration of compensating defects in the sputtered BSO:La films at lower deposition rates. Although significant structural changes were not observed in WAXRD and RC (Fig. 7.10), lower compensating defect density would theoretically lead to an increase in *n* (up to the nominal doping level) as well as reduced scattering, potentially explaining the observed trends in Fig. 7.11. Regardless, the result is an increased 300 K electron mobility for our sputtered BSO:La films at low deposition rates, reaching roughly 60 $cm^2V^{-1}s^{-1}$ at ~2 Å/min. In addition, as may have been expected from the previous thickness dependence results of section 7.3.2, the trends in transport properties with rate show little substrate dependence.

7.3.4 **Concluding Remarks**

In summary, we conducted a detailed study of structural and electron mobility optimization in $Ba_{0.98}La_{0.02}SnO_3$ epitaxial films deposited by high pressure oxygen sputtering. Variation of the deposition temperature resulted in 100% La dopant activation

only above 800 °C. The results also suggest a possibility of further improvement in mobility with post-growth thermal annealing treatments. Mobility as a function of film thickness showed an initial increase to a maximum, followed by a decreasing trend, irrespective of mismatch with the substrate. The thickness at which this maximum mobility was observed is dependent on the film deposition rate (shifts towards higher *t* with increasing rate). The relative insensitivity of the electronic properties to the lattice mismatch with the substrate was explained by the similar TD densities observed in these films (~10^{11} cm^{-2}). With a reduction in deposition rate, although no changes in the structural properties were observed, electronic properties, especially mobility, showed an increasing trend. Fig. 7.12 shows the temperature-dependent electronic transport properties of the outstanding film in this study grown on PSO(001). This film exhibits an excellent room temperature electron mobility of 70 $cm^2V^{-1}s^{-1}$, increasing to 105 $cm^2V^{-1}s^{-1}$ at low temperatures. The mobility values obtained are fairly comparable to those for PLD grown films in the literature and are record values for those obtained by sputtering.

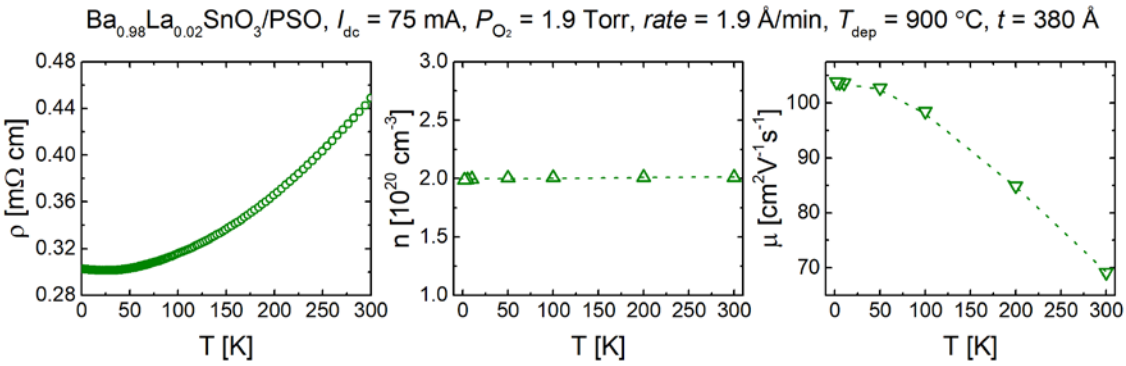

Fig. 7.12: Temperature dependence of transport properties, (a) resistivity, ρ, (b) Hall electron density, *n*, and (c) Hall electron mobility, μ, for a 380-Å-thick BSO:La film grown on PSO(001) at a rate of 2 Å/min. Dashed lines are guides to the eye.

Chapter 8: Summary and Outlook

Semiconducting oxides with *s*-orbital-derived conduction bands are attractive due to their potential for low electron effective mass and high room temperature mobility. While a lot of effort has gone into optimizing mobilities in binary wide band gap semiconducting oxides, relatively little has been done with perovskite oxides. Realizing high room temperature mobility in perovskites will be an important step towards translating the extraordinary diversity in functionality, common in this group of oxides, to room temperature. A high room temperature mobility perovskite semiconductor could enable, for instance, ambient temperature high mobility oxide two-dimensional electron systems, oxide transistors, and all-perovskite spintronic devices. In this context, the recent discovery of room temperature mobility (μ) up to 320 $cm^2V^{-1}s^{-1}$ in *n*-doped cubic perovskite ($Pm\bar{3}m$) $BaSnO_3$ (BSO) single crystals with a band gap of 3 eV is significant. This is the highest reported 300 K mobility in perovskite oxides. The origin of this high electron mobility is attributed to a small electron effective mass (0.2 m_e) in the Sn-5s-derived conduction band and low phonon scattering rates. Although single crystals are attractive from the standpoint of understanding fundamental properties of BSO, thin films are required in heterostructures for applications. However, the dearth of commercially available substrates around the 4.116 Å cubic lattice parameter of BSO results in the use of substrates with significant lattice mismatch, and consequently a low critical thickness for strain relaxation and high density of misfit and threading dislocations in the BSO films. Through recent advances in growth techniques for BSO thin films, including the use of lower mismatch substrates, undoped buffer layers, and high purity methods, μ(300 K) up to 183 $cm^2V^{-1}s^{-1}$ has been achieved. These μ values, however, still lag those in single crystals, the mismatch being widely ascribed to the high density of dislocations in the films. In addition, thin film mobilities demonstrate high sensitivity to growth technique, dopant site, and electron density (*n*). While progress with mobility optimization in heteroepitaxial BSO films has been rapid, open questions still remain regarding mobility-limiting scattering rates and conduction mechanisms in general. Against this background, this dissertation has

attempted to extend the understanding of the influence of structural defects on the electron mobility in BSO thin films.

We have demonstrated the growth of epitaxial, phase pure, relaxed, close to stoichiometric BSO films using high pressure oxygen sputter deposition. In chapter 4, we show that oxygen vacancy doping is a facile route to induce electrons in BSO. This was previously considered to be extremely difficult. Although the formation energy for an oxygen vacancy (V_O) in BSO is as low as ~1 eV (as demonstrated in chapter 5), the V_O diffusivity is only ~10^{-16} cm^2s^{-1} at 500 °C [134], orders of magnitude smaller than other perovskite oxides (typically ~10^{-7} ─ 10^{-6} cm^2s^{-1}) [142, 143], thus resulting in very small diffusion distances even at elevated temperatures. This makes it near impossible to reduce bulk crystals of BSO, but works for thin films as diffusion distances need not be large. Vacuum annealing at 850 °C is found to induce oxygen vacancies at significant densities, without secondary phase formation, enabling facile *n*-doping. Mobilities of 20 $cm^2V^{-1}s^{-1}$ at 5 x 10^{19} cm^{-3} are obtained in films only 300 Å thick, with much scope for improvement.

As discussed in chapter 5, we were able to tune the electron density in oxygen-vacancy-doped BSO epilayers simply by varying the post-deposition vacuum annealing temperature. Varying this from 600 to 900 °C in 300-Å-thick high pressure oxygen sputter-deposited films results in Hall densities between 2 × 10^{17} and 5 × 10^{19} cm^{-3}, resistivity between 10^2 and <10^{-2} Ωcm, and transport between strongly localized and metallic-like. We access a lighter doped regime compared to any prior work on BSO, potentially indicating lower levels of compensating defects/deep traps than some prior studies. We find that the mobility increases as $n^{0.65}$ over the entire doping range studied, indicating the predominance of dislocation scattering in these films. The maximum observed mobility is 25 $cm^2V^{-1}s^{-1}$, although there exists much scope for mobility improvement in V_O-doped films. Although the current choice (MgO) rules out artifacts due to V_O formation in the substrate, it is sub-optimal in terms of lattice parameter and symmetry mismatch.

In chapter 6, we studied a film thickness driven insulator-metal transition in BSO. Oxygen-vacancy-doped films show decreasing electron density and mobility, and a

systematic resistivity upturn at low temperatures with decreasing film thickness before becoming strongly localized below 200 Å. This low *T* upturn is approximately logarithmic in temperature and is accompanied by anisotropic negative magnetoresistance. Detailed analysis of the temperature and field dependence reveals generally good agreement with a two-dimensional weak localization (2D WL) model, revealing dominant dephasing by electron-electron scattering. We demostrate that WL is the cause of the commonly observed low *T* upturn in $\rho(T)$ in BSO thin films and bulk single crystals.

Chapter 7 consisted of a detailed study of structural and electron mobility optimization in $Ba_{0.98}La_{0.02}SnO_3$ (BSO:La) epitaxial films. 2% La doping allows us to probe electron densities about a magnitude higher than that possible with V_O doping (due to limitations of the annealing chamber). Mobility as a function of film thickness showed an initial increase to a maximum, followed by a decreasing trend, irrespective of mismatch with the substrate. The relative insensitivity of the electronic properties to the lattice mismatch with the substrate was explained by the similar TD densities observed in these films (~10^{11} cm^{-2}). With a reduction in deposition rate, electronic properties, especially mobility, showed an increasing trend. We were able to optimize the mobility in these BSO:La films to 70 $cm^2V^{-1}s^{-1}$, increasing to 105 $cm^2V^{-1}s^{-1}$ at low temperatures, which are record values for sputtered films.

Overall, the results of this thesis demonstrate high pressure oxygen sputtering as a viable growth technique to produce high quality BSO films. Although the mobilities found fell well short of those obtained in single crystals and thin films grown by MBE, they are comparable with the values reported on films grown by PLD. There is scope, however, for further improvement in mobility in these BSO films through the insertion of buffer layers, post-growth thermal annealing, modulation doping, δ-doping, *etc*. Reports in the literature do highlight the importance of thick buffer layers of undoped BSO in improving the electron mobility in the doped active channel. In chapter 7, we see an increase in mobility with increase in deposition temperature, which suggests that post-growth high temperature annealing might be an effective tool in improving mobility. A recent report explored the

potential of $BaSn_{1-x}Hf_xO_3$ as the doped buffer layer in modulation-doped BSO heterostructures [144].

There also has been a recent push for fabrication of field-effect devices using BSO as a channel material [53-55, 99]. Several gate oxides such as Al_2O_3, $LaInO_3$, and HfO_2 have been used in these devices. A very recent report used an ionic liquid as the gate electrolyte in order to induce a very high electron density (~10^{14} cm^{-2}) at the surface of an undoped BSO film, leading to a mobility of ~200 $cm^2V^{-1}s^{-1}$ at 150 K [145]. Helin Wang and Jeff Walter (in Chris Leighton's lab) have also found success with electrostatic gating of BSO thin films. The data indicates reversible electrostatic control of electron density over an unprecedented gate bias window, leading to, for instance, insulator-metal transitions and enhancement of mobility in these thin films (Fig. 8.1) [146]. The work on external field controlled modulation of electronic mobility is still in its early stages and requires further investigation.

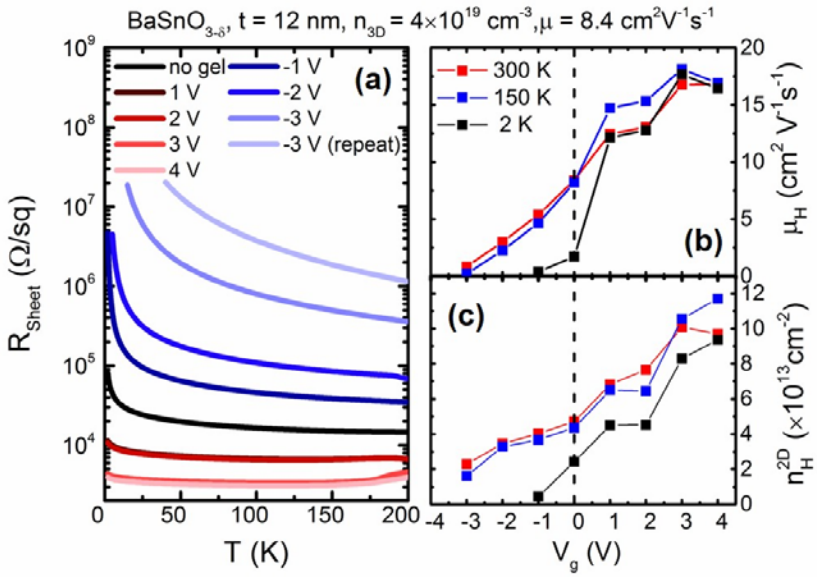

Fig. 8.1: Electronic transport properties of an ion-gel gated 120-Å-thick oxygen vacancy-doped BSO film grown on LAO(001). (a) Temperature dependence of the sheet resistance, R_{sheet} for different applied gate biases. Gate bias dependence of (b) Hall electron mobility, μ, and (c) 2D Hall electron density, n_{2D}, at 300 K (red), 150 K (blue), 2 K (black).

It would be also interesting to explore the lightly doped regime with La-doping of BSO. 0.2% La-doped BSO films should ideally (100% dopant activation) similar electron densities as the V_O-doped films discussed in this thesis, and would allow us to compare doping in different sites. Furthermore, there are almost no reports on *p*-type doping of BSO, possibly because of a very limited choice of cations available for substitution at the *A* site. On the *B* site, however, Ga is an attractive option given the similarity between the ionic radius of Ga^{3+} (0.62 Å) and $Sn4^{+}$ (0.69 Å). If successful, it will allow us to fabricate BSO p-n junctions and study vertical transport.

The abovementioned ideas are some of the many exciting avenues that can be pursued. Research on BSO is still in its early stages and more experiments are required to clearly understand its structural, chemical, and electronic properties.

9 Bibliography

[1] M. Johnsson and P. Lemmens, J. Phys. **20**, 264001 (2008).
[2] J. M. Rondinelli, S. J. May, and J. W. Freeland, MRS Bull. **37**, 261 (2012).
[3] J. M. D. Coey, M. Viret, and S. von Molnár, Adv. Phys. **48**, 167 (1999).
[4] R. E. Cohen, Nature **358**, 136 (1992).
[5] R. Guo, L. E. Cross, S. E. Park, B. Noheda, D. E. Cox, and G. Shirane, Phys. Rev. Lett. **84**, 5423 (2000).
[6] P. M. Grant, R. B. Beyers, E. M. Engler, G. Lim, S. S. P. Parkin, M. L. Ramirez, V. Y. Lee, A. Nazzal, J. E. Vazquez, and R. J. Savoy, Phys. Rev. B **35**, 7242 (1987).
[7] S. Jin, T. H. Tiefel, M. McCormack, R. A. Fastnacht, R. Ramesh, and L. H. Chen, Science **264**, 413 (1994).
[8] A. Ohtomo and H. Y. Hwang, Nature **427**, 423 (2004).
[9] J. B. Goodenough, Localized to Itinerant Electronic Transitions in Perovskite Oxides (Springer, New York, 2001).
[10] J. A. Sulpizio, S. Ilani, P. Irvin, and J. Levy, Ann. Rev. Mater. Res. **44**, 117 (2014).
[11] K. A. Müller and H. Burkard, Phys. Rev. B **19**, 3593 (1979).
[12] J. Hemberger, P. Lunkenheimer, R. Viana, R. Böhmer, and A. Loidl, Phys. Rev. B **52**, 13159 (1995).
[13] H. Uwe and T. Sakudo, Phys. Rev. B **13**, 271 (1976).
[14] K. van Benthem, C. Elsässer, and R. H. French, J. Appl. Phys. **90**, 6156 (2001).
[15] A. Spinelli, M. A. Torija, C. Liu, C. Jan, and C. Leighton, Phys. Rev. B **81**, 155110 (2010).
[16] C. Lee, J. Destry, and J. L. Brebner, Phys. Rev. B **11**, 2299 (1975).
[17] O. N. Tufte and E. L. Stelzer, Phys. Rev. **173**, 775 (1968).
[18] O. N. Tufte and P. W. Chapman, Phys. Rev. **155**, 796 (1967).
[19] J. Son, P. Moetakef, B. Jalan, O. Bierwagen, N. J. Wright, R. Engel-Herbert, and S. Stemmer, Nat. Mater. **9**, 482 (2010).
[20] T. A. Cain, A. P. Kajdos, and S. Stemmer, Appl. Phys. Lett. **102**, 182101 (2013).
[21] B. Jalan, S. J. Allen, G. E. Beltz, P. Moetakef, and S. Stemmer, Appl. Phys. Lett. **98**, 132102 (2011).
[22] R. Ramesh, Curr. Sci. **105**, 1107 (2013).
[23] P. Zubko, S. Gariglio, M. Gabay, P. Ghosez, and J-M. Triscone, Annu. Rev. Condens. Matter Phys. **2**, 141 (2011).
[24] D. G. Schlom, L.-Q. Chen, X. Pan, A. Schmehl, and M. A. Zurbuchen, J. Am. Ceram. Soc. **91**, 2429 (2008).
[25] L. Qiao, T. C. Droubay, T. C. Kaspar, P. V. Sushko, and S. A. Chambers, Surf. Sci. **605**, 1381 (2011).
[26] W. Siemons, G. Koster, H. Yamamoto, W. A. Harrison, G. Lucovsky, T. H. Geballe, D. H. A. Blank, and M. R. Beasley, Phys. Rev. Lett. **98**, 196802 (2007).
[27] A. Kalabukhov, R. Gunnarsson, J. Börjesson, E. Olsson, T. Claeson, and D. Winkler, Phys. Rev. B **75**, 121404 (2007).
[28] N. Nakagawa, H. Y. Hwang, and D. A. Muller, Nat. Mater. **5**, 204 (2006).

[29] P. Xu, T. C. Droubay, J. S. Jeong, K. A. Mkhoyan, P. V. Sushko, S. A. Chambers, and B. Jalan, Adv. Mater. Interfaces **3**, 1500432 (2016).
[30] P. Xu, D. Phelan, J. S. Jeong, K. A. Mkhoyan, and B. Jalan, Appl. Phys. Lett. **104**, 082109 (2014).
[31] T. A. Cain, P. Moetakef, C. A. Jackson, and S. Stemmer, Appl. Phys. Lett. **101**, 111604 (2012).
[32] P. Moetakef, T. A. Cain, D. G. Ouellette, J. Y. Zhang, D. O. Klenov, A. Janotti, C. G. Van de Walle, S. Rajan, S. J. Allen, and S. Stemmer, Appl. Phys. Lett. **99**, 232116 (2011).
[33] R. Ohtsuka, M. Matvejeff, K. Nishio, R. Takahashi, and M. Lippmaa, Appl. Phys. Lett. **96**, 192111 (2010).
[34] J. S. Kim, S. S. A. Seo, M. F. Chisholm, R. K. Kremer, H. U. Habermeier, B. Keimer, and H. N. Lee, Phys. Rev. B **82**, 201407 (2010).
[35] B. Jalan, S. Stemmer, S. Mack, and S. J. Allen, Phys. Rev. B **82**, 081103 (2010).
[36] Y. Kozuka, M. Kim, C. Bell, B. G. Kim, Y. Hikita, and H. Y. Hwang, Nature **462**, 487 (2009).
[37] H. R. Liu, J. H. Yang, H. J. Xiang, X. G. Gong, and S. H. Wei, Appl. Phys. Lett. **102**, 112109 (2013).
[38] T. Makino, Y. Segawa, A. Tsukazaki, A. Ohtomo, and M. Kawasaki, Appl. Phys. Lett. **87**, 022101 (2005).
[39] A. Tsukazaki, A. Ohtomo, T. Kita, Y. Ohno, H. Ohno, and M. Kawasaki, Science **315**, 1388 (2007).
[40] J. Falson, D. Maryenko, Y. Kozuka, A. Tsukazaki, and M. Kawasaki, Appl. Phys. Exp. **4**, 091101 (2011).
[41] A. Tsukazaki, S. Akasaka, K. Nakahara, Y. Ohno, H. Ohno, D. Maryenko, A. Ohtomo, and M. Kawasaki, Nat. Mater. **9**, 889 (2010).
[42] P. D. C. King and T. D. Veal, J. Phys. **23**, 334214 (2011).
[43] R. Ramesh and D. G. Schlom, MRS Bull. **33**, 1006 (2011).
[44] H. Y. Hwang, Y. Iwasa, M. Kawasaki, B. Keimer, N. Nagaosa, and Y. Tokura, Nat. Mater. **11**, 103 (2012).
[45] L. Bjaalie, B. Himmetoglu, L. Weston, A. Janotti, and C. G. Van de Walle, New J. Phys. **16**, 025005 (2014).
[46] X. Luo, Y. S. Oh, A. Sirenko, P. Gao, T. A. Tyson, K. Char, and S. W. Cheong, Appl. Phys. Lett. **100**, 172112 (2012).
[47] H. J. Kim, U. Kim, T. H. Kim, J. Kim, H. M. Kim, B. G. Jeon, W. J. Lee, H. S. Mun, K. T. Hong, J. Yu, K. Char, and K. H. Kim, Phys. Rev. B **86**, 165205 (2012).
[48] H. J. Kim, U. Kim, H. M. Kim, T. H. Kim, H. S. Mun, B. G. Jeon, K. T. Hong, W. J. Lee, C. Ju, K. H. Kim, and K. Char, Appl. Phys. Express **5**, 061102 (2012).
[49] D. O. Scanlon, Physical Review B **87**, 161201 (2013).
[50] X. F. Fan, W. T. Zheng, X. Chen, and D. J. Singh, Plos One **9**, e91423 (2014).
[51] S. A. Chambers, T. C. Kaspar, A. Prakash, G. Haugstad, and B. Jalan, Appl. Phys. Lett. **108** (15), 152104 (2016).
[52] K. Krishnaswamy, L. Bjaalie, B. Himmetoglu, A. Janotti, L. Gordon, and C. G. Van de Walle, Appl. Phys. Lett. **108**, 083501 (2016).

[53] Y. M. Kim, C. Park, U. Kim, C. Ju, and K. Char, Appl. Phys. Express **9**, 011201 (2016).
[54] U. Kim, C. Park, T. Ha, Y. M. Kim, N. Kim, C. Ju, J. Park, J. Yu, J. H. Kim, and K. Char, APL Mater. **3**, 036101 (2015).
[55] C. Park, U. Kim, C. J. Ju, J. S. Park, Y. M. Kim, and K. Char, Appl. Phys. Lett. **105**, 203503 (2014).
[56] S. Raghavan, T. Schumann, H. Kim, J. Y. Zhang, T. A. Cain, and S. Stemmer, APL Mater. **4**, 016106 (2016).
[57] A. Prakash, P. Xu, A. Faghaninia, S. Shukla, J. W. Ager III, C. S. Lo, and B. Jalan, Nat. Commun. **8**, 15167 (2017).
[58] W.-J. Lee, H. J. Kim, J. Kang, D. H. Jang, T. H. Kim, J. H. Lee, and K. H. Kim, Annu. Rev. Mater. Res. **47**, 391 (2017).
[59] Qinzhuang Liu, Jianming Dai, Zhongliang Liu, Xiaobo Zhang, Guangping Zhu, and Guohua Ding, J. Phys. D: Appl. Phys. **43**, 455401 (2010).
[60] H. Mizoguchi, H. W. Eng, and P. M. Woodward, Inorg. Chem. **43**, 1667 (2004).
[61] R. J. Cava, P. Gammel, B. Batlogg, J. J. Krajewski, W. F. Peck, L. W. Rupp, R. Felder, and R. B. van Dover, Phys. Rev. B **42**, 4815 (1990).
[62] S. Yasuhiro, F. Yoshiki, N. Tomoki, A. Hiromichi, and S. Tetsuro, Chem. Lett. **14**, 377 (1985).
[63] S. Upadhyay, O. Parkash, and D. Kumar, J. Phys. D **37**, 1483 (2004).
[64] H. Yun, M. Topsakal, A. Prakash, K. Ganguly, C. Leighton, B. Jalan, R. M. Wentzcovitch, K. A. Mkhoyan, and J. S. Jeong, J. Vac. Sci. Technol. A **36**, 031503 (2018).
[65] Y. Li, L. Zhang, Y. Ma, and D. J. Singh, APL Mater. **3**, 011102 (2015).
[66] D. J. Singh, Q. Xu, and K. P. Ong, Appl. Phys. Lett. **104**, 011910 (2014).
[67] B. G. Kim, J. Y. Jo, and S. W. Cheong, J. Solid State Chem. **197**, 134 (2013).
[68] S. Soleimanpour and F. Kanjouri, Physica B **432**, 16 (2014).
[69] K. Krishnaswamy, B. Himmetoglu, Y. Kang, A. Janotti, and C. G. Van de Walle, Phys. Rev. B **95**, 205202 (2017).
[70] S. Dabaghmanesh, R. Saniz, M. N. Amini, D. Lamoen, and B. Partoens, J. Phys. Condens. Matter. **25**, 415503 (2013).
[71] E. Moreira, J. M. Henriques, D. L. Azevedo, E. W. S. Caetano, V. N. Freire, and E. L. Albuquerque, J. Solid State Chem. **187**, 186 (2012).
[72] S. J. Allen, S. Raghavan, T. Schumann, K. M. Law, and S. Stemmer, Appl. Phys. Lett. **108**, 252107 (2016).
[73] C. A. Niedermeier, S. Rhode, K. Ide, H. Hiramatsu, H. Hosono, T. Kamiya, and M. A. Moram, Phys. Rev. B **95**, 161202 (2017).
[74] C. A. Niedermeier, S. Rhode, S. Fearn, K. Ide, M. A. Moram, H. Hiramatsu, H. Hosono, and T. Kamiya, Appl. Phys. Lett. **108**, 172101 (2016).
[75] H. J. Kim, J. Kim, T. H. Kim, W. J. Lee, B. G. Jeon, J. Y. Park, W. S. Choi, D. W. Jeong, S. H. Lee, J. Yu, T. W. Noh, and K. H. Kim, Phys. Rev. B **88**, 125204 (2013).
[76] U. Kim, C. Park, T. Ha, R. Kim, H. S. Mun, H. M. Kim, H. J. Kim, T. H. Kim, N. Kim, J. Yu, K. H. Kim, J. H. Kim, and K. Char, APL Mater. **2**, 056107 (2014).

[77] D. Seo, K. Yu, Y. J. Chang, E. Sohn, K. H. Kim, and E. J. Choi, Appl. Phys. Lett. **104**, 022102 (2014).
[78] C. Shan, T. Huang, J. Zhang, M. Han, Y. Li, Z. Hu, and J. Chu, J. Phys. Chem. C **118**, 6994 (2014).
[79] P. Zhang, F. Su, J. Dai, K. Zhang, C. Zhang, W. Zhou, Q. Liu, and L. Pi, EPL **106**, 67005 (2014).
[80] R. D. Shannon, Acta Crystallogr. A **32**, 751 (1976).
[81] H. Paik, Z. Chen, E. Lochocki, A. Seidner H., A. Verma, N. Tanen, J. Park, M. Uchida, S. Shang, B.-C. Zhou, M. Brützam, R. Uecker, Z.-K. Liu, D. Jena, K. M. Shen, D. A. Muller, and D. G. Schlom, APL Mater. **5**, 116107 (2017).
[82] U. S. Alaan, P. Shafer, A. T. N'Diaye, E. Arenholz, and Y. Suzuki, Appl. Phys. Lett. **108**, 042106 (2016).
[83] E. McCalla, D. Phelan, M. J. Krogstad, B. Dabrowski, and C. Leighton, submitted to Phys. Rev. Mater. (2018).
[84] T. Huang, T. Nakamura, M. Itoh, Y. Inaguma, and O. Ishiyama, J. Mater. Sci. **30**, 1556 (1995).
[85] D. O. Scanlon, Phys. Rev. B **87**, 161201 (2013).
[86] H. J. Kim, U. Kim, H. M. Kim, T. H. Kim, H. S. Mun, B. G. Jeon, K. T. Hong, W. J. Lee, C. Ju, K. H. Kim, and K. Char, Appl. Phys. Exp. **5**, 061102 (2012).
[87] J. Gazquez, S. Bose, M. Sharma, M. A. Torija, S. J. Pennycook, C. Leighton, and M. Varela, APL Mater. **1**, 012105 (2013).
[88] Y. S. Kim, D. J. Kim, T. H. Kim, T. W. Noh, J. S. Choi, B. H. Park, and J.-G. Yoon, Appl. Phys. Lett. **91**, 042908 (2007).
[89] N. A. Pertsev, A. K. Tagantsev, and N. Setter, Phys. Rev. B **61**, R825 (2000).
[90] J. W. Matthews and A. E. Blakeslee, J. Cryst. Growth **27**, 118 (1974).
[91] P. V. Wadekar, J. Alaria, M. O'Sullivan, N. L. O. Flack, T. D. Manning, L. J. Phillips, K. Durose, O. Lozano, S. Lucas, J. B. Claridge, and M. J. Rosseinsky, Appl. Phys. Lett. **105**, 052104 (2014).
[92] K. Ganguly, P. Ambwani, P. Xu, J. S. Jeong, K. A. Mkhoyan, C. Leighton, and B. Jalan, APL Mater. **3**, 062509 (2015).
[93] K. Ganguly, A. Prakash, B. Jalan, and C. Leighton, APL Mater. **5**, 056102 (2017).
[94] A. Prakash, P. Xu, X. Wu, G. Haugstad, X. Wang, and B. Jalan, J. Mater. Chem. C **5**, 5730 (2017).
[95] Z. Lebens-Higgins, D. O. Scanlon, H. Paik, S. Sallis, Y. Nie, M. Uchida, N. F. Quackenbush, M. J. Wahila, G. E. Sterbinsky, D. A. Arena, J. C. Woicik, D. G. Schlom, and L. F. J. Piper, Phys. Rev. Lett. **116**, 027602 (2016).
[96] A. Prakash, J. Dewey, H. Yun, J. S. Jeong, K. A. Mkhoyan, and B. Jalan, J. Vac. Sci. Technol. A **33**, 060608 (2015).
[97] S. Strite and H. Morkoç, J. Vac. Sci. Technol. B **10**, 1237 (1992).
[98] J. Shiogai, K. Nishihara, K. Sato, and A. Tsukazaki, AIP Advances **6**, 065305 (2016).
[99] J. Shin, Y. M. Kim, Y. Kim, C. Park, and K. Char, Appl. Phys. Lett. **109**, 262102 (2016).

[100] J. Shin, Y. M. Kim, Y. Kim, C. Park, and K. Char, Appl. Phys. Lett. **109** (26), 262102 (2016).
[101] R. H. Wei, X. W. Tang, Z. Z. Hui, X. Luo, J. M. Dai, J. Yang, W. H. Song, L. Chen, X. G. Zhu, X. B. Zhu, and Y. P. Sun, Appl. Phys. Lett. **106**, 101906 (2015).
[102] H. M. Ng, D. Doppalapudi, T. D. Moustakas, N. G. Weimann, and L. F. Eastman, Appl. Phys. Lett. **73**, 821 (1998).
[103] M. W. Barsoum, Fundaments of Ceramics (CRC Press, 2002).
[104] H. Chou, P. I. Lin, C. C. Hsu, T. C. Chow, M. T. Hong, Y. C. Chen, J. R. Liu, and T. P. Tsai, J. Vac. Sci. Technol. A **20**, 441 (2002).
[105] D. J. Kester and R. Messier, J. Mater. Res. **8**, 1938 (2011).
[106] U. Poppe, N. Klein, U. Dähne, H. Soltner, C. L. Jia, B. Kabius, K. Urban, A. Lubig, K. Schmidt, S. Hensen, S. Orbach, G. Müller, and H. Piel, J. Appl. Phys. **71**, 5572 (1992).
[107] U. Poppe, J. Schubert, R. R. Arons, W. Evers, C. H. Freiburg, W. Reichert, K. Schmidt, W. Sybertz, and K. Urban, Solid State Communications **66** (6), 661 (1988).
[108] F. Y. Bruno, J. Garcia-Barriocanal, M. Varela, N. M. Nemes, P. Thakur, J. C. Cezar, N. B. Brookes, A. Rivera-Calzada, M. Garcia-Hernandez, C. Leon, S. Okamoto, S. J. Pennycook, and J. Santamaria, Phys. Rev. Lett. **106**, 147205 (2011).
[109] N. A. Pertsev, A. Petraru, H. Kohlstedt, R. Waser, I. K. Bdikin, D. Kiselev, and A. L. Kholkin, Nanotechnology **19**, 375703 (2008).
[110] M. Grizalez, E. Delgado, M. E. Gómez, and P. Prieto, Phys. Stat. C **4**, 4203 (2007).
[111] P. Ambwani, P. Xu, G. Haugstad, J. S. Jeong, R. Deng, K. A. Mkhoyan, B. Jalan, and C. Leighton, J. Appl. Phys. **120**, 055704 (2016).
[112] J. E. Ayers, Heteroepitaxy of Semiconductors (CRC Press, 2007).
[113] G. H. Stout and L. H. Jensen, X-ray Structure Determination: A Practical Guide (Wiley, Hoboken, 1989).
[114] D. K. Bowen and B. K. Tanner, High Resolution X-ray Diffractometry and Topography (Taylor & Francis, London, 1998).
[115] B. D. Cullity and S. R. Stock, Elements of X-ray Diffraction (Prentice Hall, 2001).
[116] C. Kittel, Introduction to Solid State Physics (John Wiley & Sons, Inc., 2005).
[117] PANalytical, X'Pert Pro MRD User's Guide (2002).
[118] V. Holy, U. Pietsch, and T. Baumbach, High-Resolution X-ray Scattering from Thin Films and Multilayers, Springer Tracts in Modern Physics **149** (Springer, 1999).
[119] P. F. Fewster, Rep. Prog. Phys. **59**, 1339 (1996).
[120] M. Bjorck and G. Andersson, J. Appl. Cryst. **40**, 1174 (2007).
[121] D. Brandon and W. D. Kaplan, Microstructural Characterization of Materials (John Wiley & Sons, Ltd., UK, 2008).
[122] S. J. Pennycook and P. D. Nellist, Scanning Transmission Electron Microscopy: Imaging and Analysis (Springer, 2011).
[123] R. F. Egerton, Micron **34**, 127 (2003).
[124] L. J. van der Pauw, Philips Tech. Rev. **20**, 220 (1958).
[125] L. J. van der Pauw, Philips Res. Rep. **13**, 1 (1958).

[126] M. Bjorck and G. Andersson, J. Appl. Crystallogr. **40**, 1174 (2007).
[127] H. J. Kim, U. Kim, T. H. Kim, J. Kim, H. M. Kim, B.-G. Jeon, W.-J. Lee, H. S. Mun, K. T. Hong, J. Yu, K. Char, and K. H. Kim, Phys. Rev. B **86**, 165205 (2012).
[128] H. F. Wang, Q. Z. Liu, F. Chen, G. Y. Gao, Wenbin Wu, and X. H. Chen, J. Appl. Phys. **101**, 106105 (2007).
[129] H. Mun, U. Kim, H. M. Kim, C. Park, T. H. Kim, H. J. Kim, K. H. Kim, and K. Char, Appl. Phys. Lett. **102**, 252105 (2013).
[130] X. Luo, Y. S. Oh, A. Sirenko, P. Gao, T. A. Tyson, K. Char, and S.-W. Cheong, Appl. Phys. Lett. **100**, 172112 (2012).
[131] R. J. Cava, P. Gammel, B. Batlogg, J. J. Krajewski, W. F. Peck, L. W. Rupp, R. Felder, and R. B. van Dover, Phys. Rev. B **42**, 4815 (1990).
[132] E. Moreira, J. M. Henriques, D. L. Azevedo, E. W. S. Caetano, V. N. Freire, and E. L. Albuquerque, J. Solid State Chem. **187**, 186 (2012).
[133] R. D. Shannon, J. L. Gillson, and R. J. Bouchard, J. Phys. Chem. Solids **38**, 877 (1977).
[134] W. J. Lee, H. J. Kim, E. Sohn, H. M. Kim, T. H. Kim, K. Char, J. H. Kim, and K. H. Kim, Phys. Status Solidi A **212** (7), 1487 (2015).
[135] A. G. Zabrodskii, Philos. Mag. B **81** (9), 1131 (2001).
[136] P. Singh, B. J. Brandenburg, C. P. Sebastian, P. Singh, S. Singh, D. Kumar, and O. Parkash, Jpn. J. Appl. Phys. **47**, 3540 (2008).
[137] Hyosik Mun, Useong Kim, Hoon Min Kim, Chulkwon Park, Tai Hoon Kim, Hyung Joon Kim, Kee Hoon Kim, and Kookrin Char, Appl. Phys. Lett. **102**, 252105 (2013).
[138] Patrick A. Lee and T. V. Ramakrishnan, Reviews of Modern Physics **57** (2), 287 (1985).
[139] Gerd Bergmann, Physical Review B **28** (6), 2914 (1983).
[140] E. H. Smith, P. D. C. King, A. Soukiassian, D. G. Ast, and D. G. Schlom, Appl. Phys. Lett. **111**, 131903 (2017).
[141] H. Yun, K. Ganguly, W. M. Postiglione, B. Jalan, C. Leighton, K. A. Mkhoyan, and J. S. Jeong, Sci. Rep **8**, 10245 (2018).
[142] R. A. De Souza, V. Metlenko, D. Park, and T. E. Weirich, Phys. Rev. B **85**, 174109 (2012).
[143] M. Kessel, R. A. De Souza, and M. Martin, Phys. Chem. Chem. Phys. **17**, 12587 (2015).
[144] J. Shin, J. Lim, T. Ha, Y. M. Kim, C. Park, J. Yu, J. H. Kim, and K. Char, Phys. Rev. Mater. **2**, 021601 (2018).
[145] K. Fujiwara, K. Nishihara, J. Shiogai, and A. Tsukazaki, Appl. Phys. Lett. **110**, 203503 (2017).
[146] H. Wang, J. Walter, K. Ganguly, B. Yu, M. Greven, and Leighton C., Phys. Rev. Mater. (in preparation, 2018).

10 Appendices

I. Calculation of Pseudocubic Lattice Parameter

Pseudocubic lattice parameter (a_{pc}) is determined for orthorhombic and rhombohedral crystal structures using the following equations:

$$a_{pc}(O) = \frac{\sqrt{a^2 + b^2}}{2}$$

$$a_{pc}(R) = \frac{a}{\sqrt{2}}$$

where *a*, *b*, and *c* are the respective orthorhombic lattice constants.

II. Structure and Transport in High Pressure Oxygen Sputter-Deposited $BaSnO_{3-\delta}$

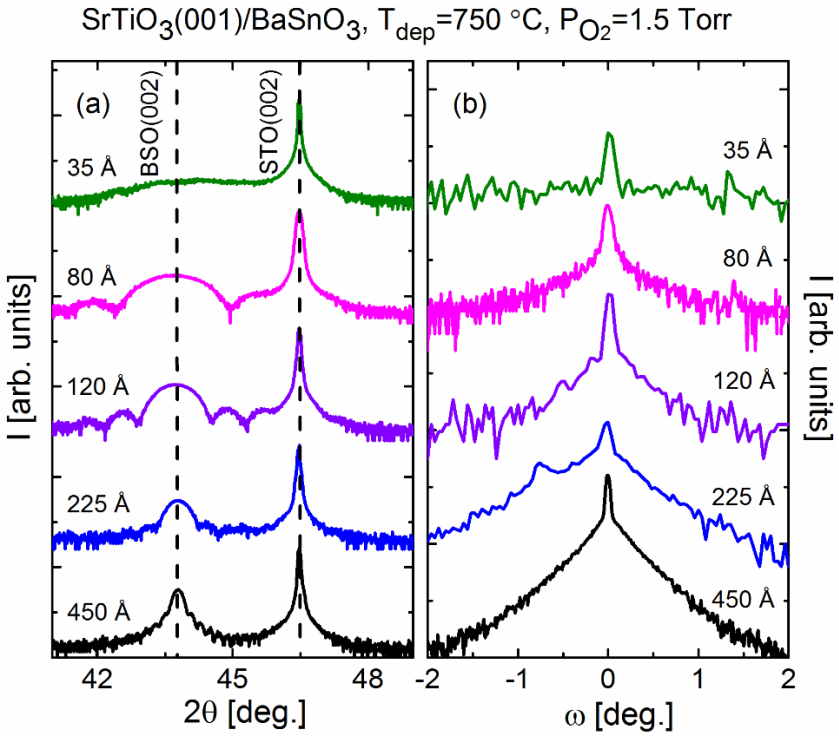

Fig. A1: (a) High-resolution wide-angle X-ray diffraction (around the 002 reflections), and (b) 002 rocking curves (transverse scans) from $SrTiO_3(001)/BaSnO_3$ films as a function of

$BaSnO_3$ film thicknesses (from 35 to 450 Å). The intensity is shown on a log-scale, with the curves displaced for clarity. Note the evolution in the film peak width and fringe spacing in (a), and the progressive additional broad contribution in (b). The vertical dashed lines in (a) are guides to the eye, marking the film and substrate peak positions.

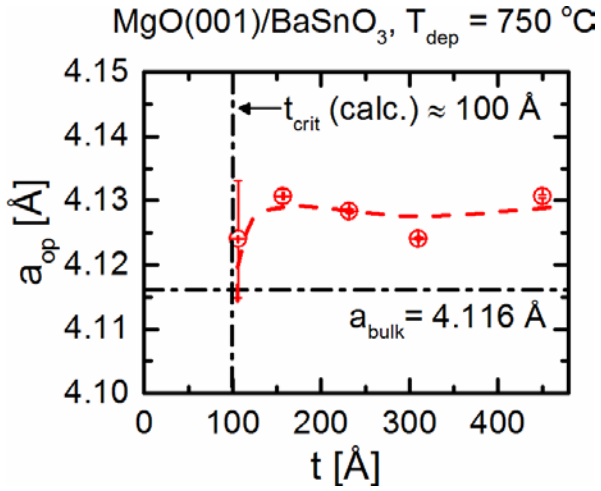

Fig. A2: Thickness dependence of the out-of-plane lattice parameter of $BaSnO_3$ films grown on MgO(001). The films were deposited at 750 °C in 1.5 Torr of O_2. The horizontal and vertical dash-dot lines mark the bulk lattice parameter and estimated critical thickness for strain relaxation (from the Matthews-Blakeslee formula). Note the thickness independence above approximately 150 Å, and the slightly expanded value compared to bulk. The true critical thickness is expected to lie below 100 Å.

III. Mobility-Electron Density Relation Probed *via* Controlled Oxygen Vacancy Doping in Epitaxial $BaSnO_3$

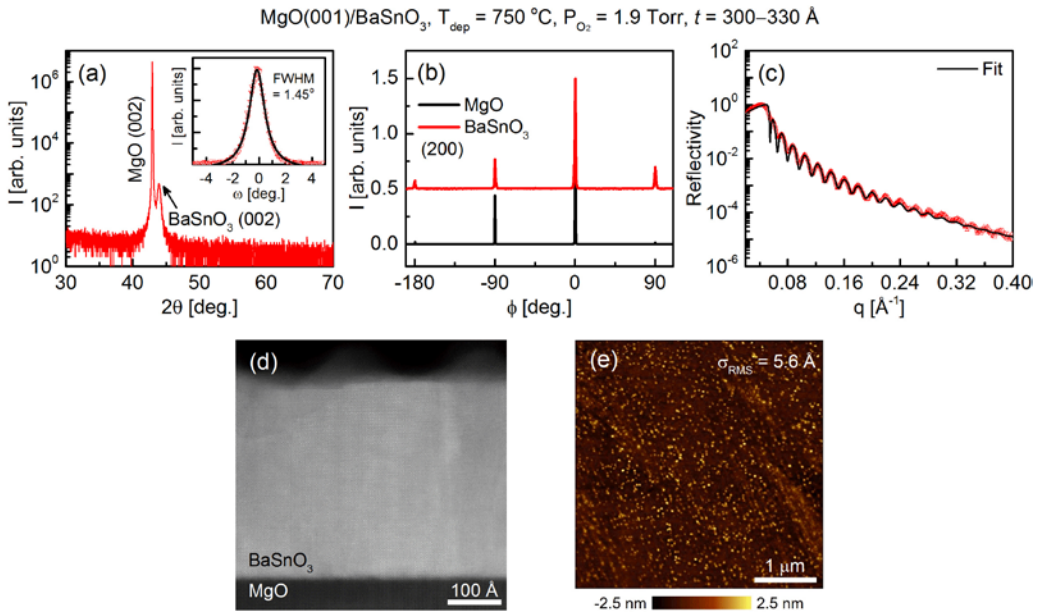

Fig. A3: Summary of structural characterization results for 300 – 330-Å-thick BSO films deposited on MgO(001) at 750 °C in 1.9 Torr of O_2. (a) High resolution wide-angle X-ray diffraction (WAXRD) showing the (002) substrate and film reflections; no peaks from any secondary phase can be seen. The out-of-plane lattice parameter extracted from the (002) BSO reflection is 4.121 Å, close to the bulk value of 4.116 Å, indicating a relaxed film. As noted in our prior work, the slight remnant lattice parameter expansion could indicate some small non-stoichiometry. Inset: (002) rocking curve for the same film having a full-width-at-half-maximum (FWHM) of 1.45º; this is larger than BSO on perovskite substrates. (b) Grazing incidence in-plane X-ray diffraction (φ scan) for the (200) film and substrate reflections (reproduced from the supplementary material from Ref. [92]). The data in (a) along with that in (b) confirm the cube-on-cube epitaxial growth of BSO on MgO(001). (c) Grazing incidence X-ray reflectivity (GIXR) along with a GenX fit (solid black line). The refined film densities and surface roughnesses are 7.16 g cm^{-3} and 2.6 Å, respectively, while the bulk density of BSO is 7.24 g cm^{-3}. The long lateral length scale roughness is thus beneath a unit cell from GIXR. (d) Cross-sectional high-angle annular dark field scanning transmission electron microscopy (HAADF STEM) image. Note the sharp

film/substrate interface, epitaxy, but non-negligible contrast in the film interior. Ref. [92] provides a fuller discussion of such images. (e) Contact mode atomic force microscopy (AFM) image, suggesting an RMS roughness of 5.6 Å, again confirming relatively smooth surfaces.

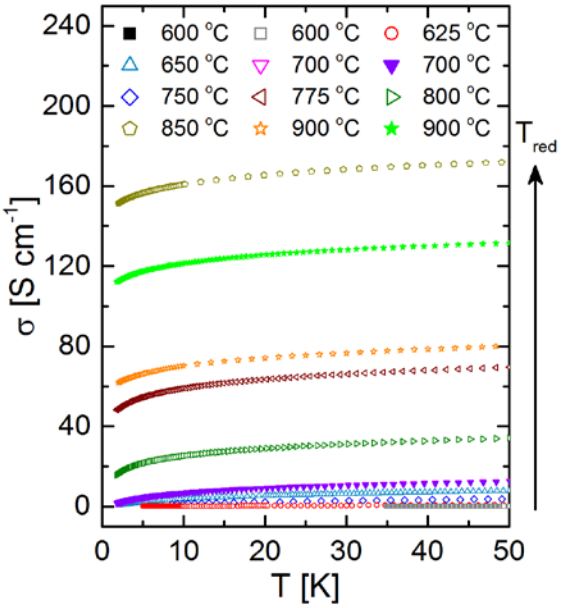

Fig. A4: Temperature (T) dependence of the film conductivity, $\sigma = 1/\rho$, below 50 K for 300 – 330-Å-thick epitaxial BSO films on MgO(001) annealed in vacuum at reduction temperatures (T_{red}) between 600–900 °C. For $T_{red} \gtrsim 775$ °C the $T \rightarrow 0$ extrapolation of σ appears finite, implying metallic behavior.

IV. Thickness-Driven Insulator-Metal Transition and Two-Dimensional Weak Localization in Epitaxial $BaSnO_3$ Thin Films

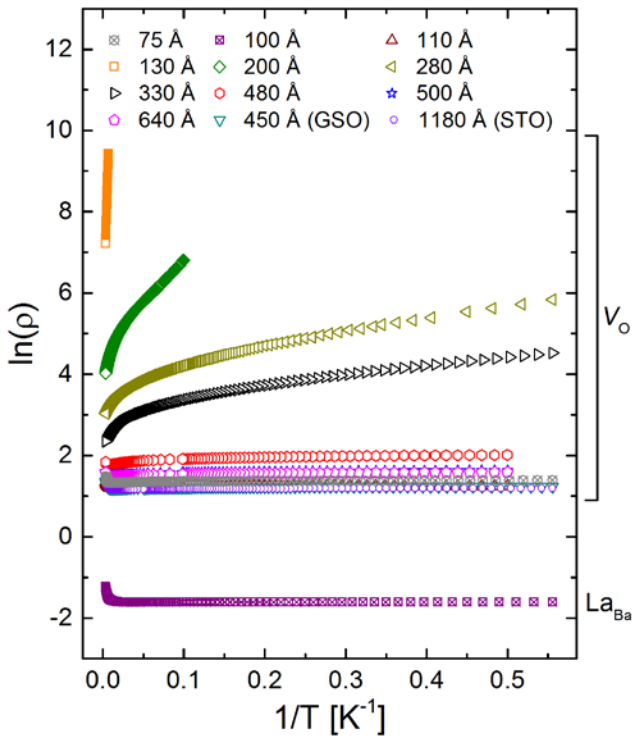

Fig. A5: Natural logarithm of the film resistivity (ρ) *vs.* inverse temperature (T^{-1}) for doped BSO films on $LaAlO_3$(001), $SrTiO_3$(001), and $GdScO_3$(001). These are the same films shown in Figure 3 of the main manuscript. Film thicknesses are shown at the top of the figure. Films on $LaAlO_3$ (75–640-Å-thick) and $GdScO_3$ (450 Å, grey) were annealed in vacuum for 4 hrs. at 900 °C to oxygen vacancy dope (labeled "V_O"), whereas the film on $SrTiO_3$ (1180 Å, purple) is 2% La doped (labeled "La_{Ba}"). Note the negligible activation energy (at least down to 1.8 K) for film thickness greater than 130 Å.

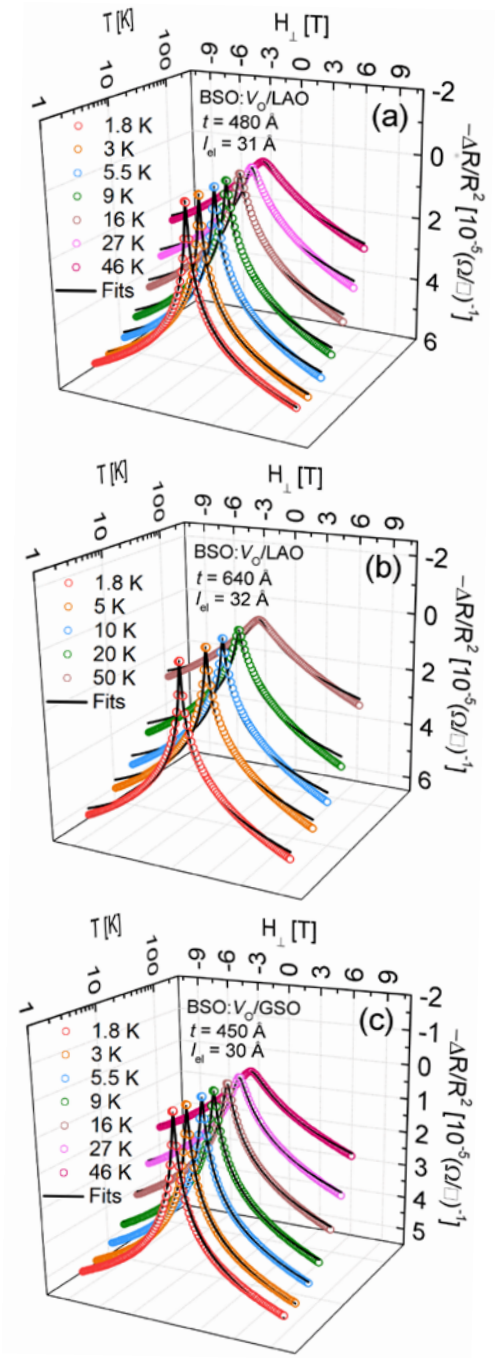

Fig. A6: Magnetic field (H) dependence of the sheet conductance, plotted as $-\Delta R/R^2$ (scale reversed), at various measurement temperatures for a (a) 480 Å, and (b) 640-Å-thick BSO films on $LaAlO_3$(001), and (c) a 450-Å-thick BSO film on $GdScO_3$(001). All films were annealed in vacuum for 4 hrs. at 900 °C to oxygen vacancy (V_O) dope, resulting in 300 K

Hall electron densities in the range of 4.5–5.3×10^{19} cm^{-3}. H is along the [001] direction, perpendicular to the film surface. Solid black lines are fits to a 2D weak localization model (with no high field logarithmic correction), where sheet conductance ($-\Delta R/R^2$) is given by:

$$\frac{-\Delta R}{R^2} = \frac{e^2}{2\pi^2\hbar}\left[\Psi\left(\frac{1}{2}+\frac{\hbar/2e}{l_{el}l_{in}H}\right)-\ln\left(\frac{\hbar/2e}{l_{el}l_{in}H}\right)\right]$$

Here, l_{el} and l_{in} are the elastic and inelastic scattering length scales, respectively, and Ψ is the digamma function. l_{el} values for these films are extracted from fitting ρ *vs.* T to a Fermi liquid model for T greater than the resistivity upturn temperature, T_{up}.

V. Structure and Mobility Optimization of High-Pressure-Oxygen-Sputtered $Ba_{0.98}La_{0.02}SnO_3$ Thin Films

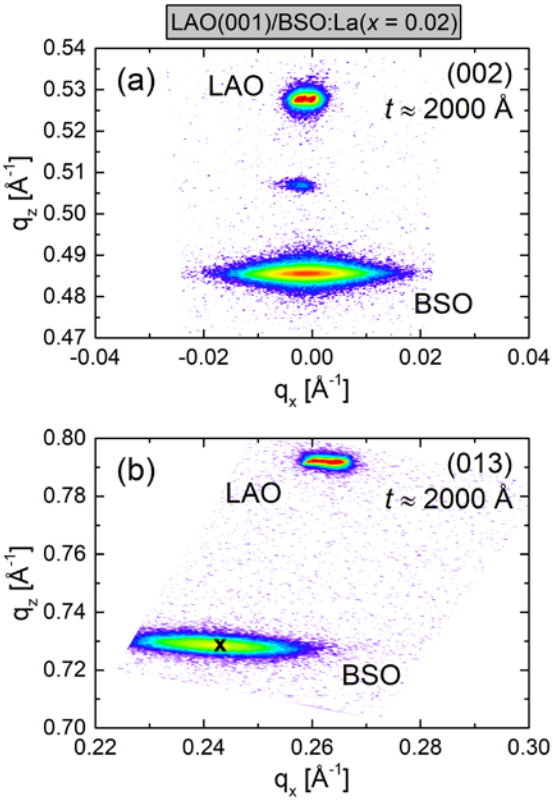

Fig. A7: (a) Symmetric specular reciprocal space map (RSM) around the 002 reflection, and (b) asymmetric non-specular RSM around the 013 reflection for a 2000-Å-thick $Ba_{0.98}La_{0.02}SnO_3$ (BSO:La) film deposited on $LaAlO_3$(001). The film was deposited at T_{dep}

= 900 °C, I_{dc} = 150 mA, and P_{O2} = 1.9 Torr, resulting in a growth rate of ~7.8 Å/min. Cross in (b) mark the expected position of fully strain-relaxed $BaSnO_3$. The estimated out-of-plane (a_{op}) and in-plane (a_{ip}) lattice parameters of the film are both 4.12 Å, confirming stoichiometric and fully relaxed BSO:La films with cube-on-cube epitaxial relationship with LAO(001).

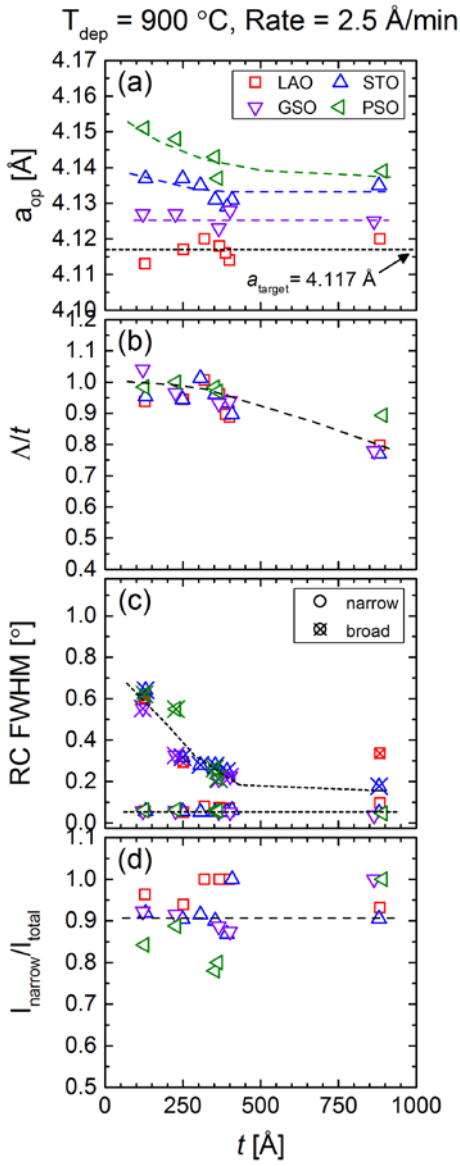

Fig. A8: Thickness (t) dependence of structural parameters determined from WAXRD. (a) Out-of-plane lattice constant, a_{op}, (b) Scherrer length-to-film-thickness ratio, Λ/t, (c) film 002 RC FWHM, and (d) intensity ratio, I_{narrow}/I_{total}, of 002 film RC (RCs exhibit both broad

and narrow components). The dashed line in (a) indicates the bulk lattice parameter of the sputtering target, while all other dashed lines are guides to the eye. All films were deposited at 900°C and ~2.5 Å/min.

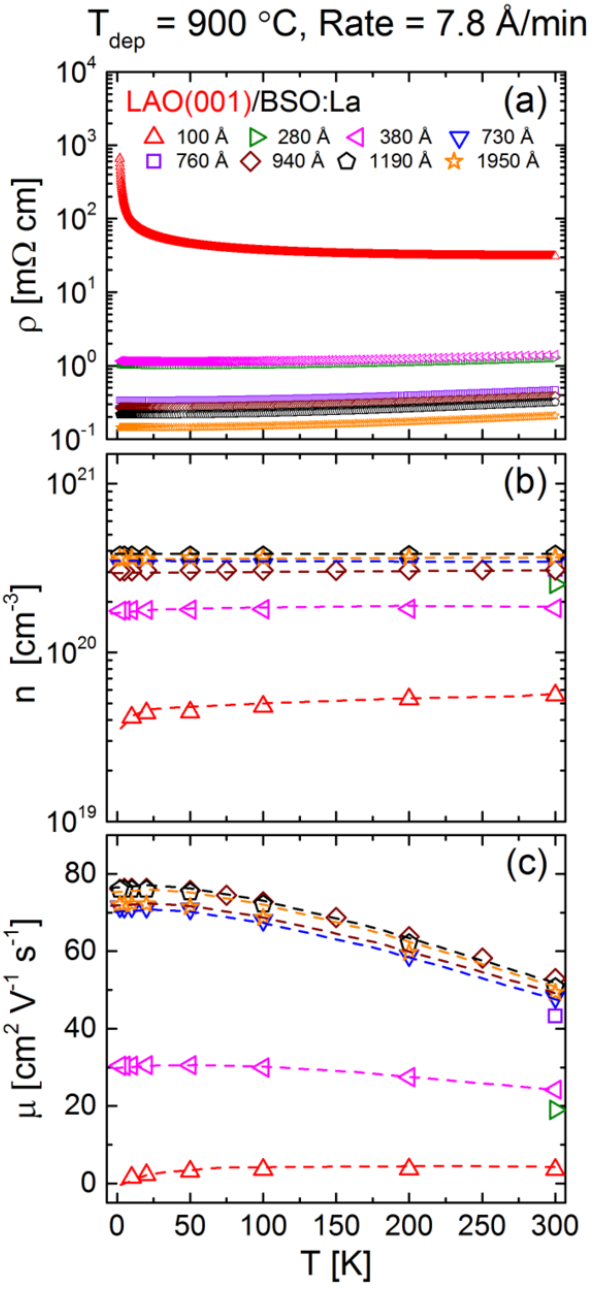

Fig. A9: Measurement temperature (*T*) dependence of transport properties (a) resistivity, ρ, (b) Hall electron density, *n*, and (c) Hall electron mobility, μ, for 100–2000-Å-thick BSO:La films grown on $LaAlO_3$(001) substrates. Films were deposited at ~8 Å/min.

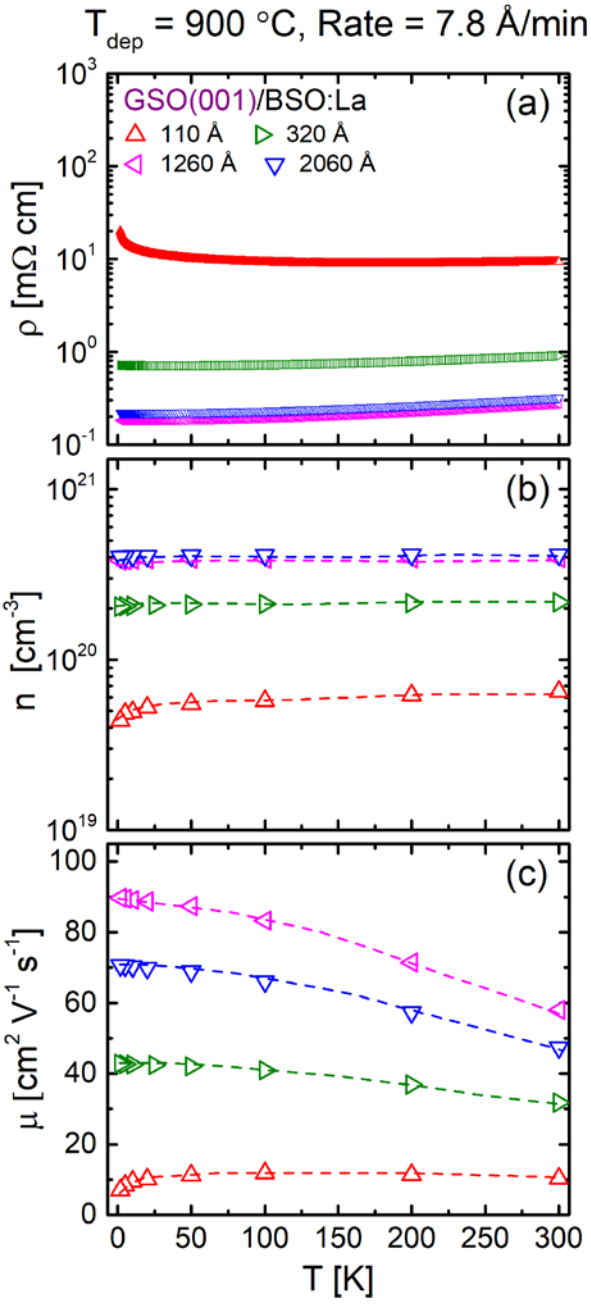

Fig. A10: Measurement temperature (*T*) dependence of transport properties (a) resistivity, ρ, (b) Hall electron density, *n*, and (c) Hall electron mobility, μ, for 100–2000-Å-thick BSO:La films grown on $GdScO_3$(001) substrates. Films were deposited at ~8 Å/min.

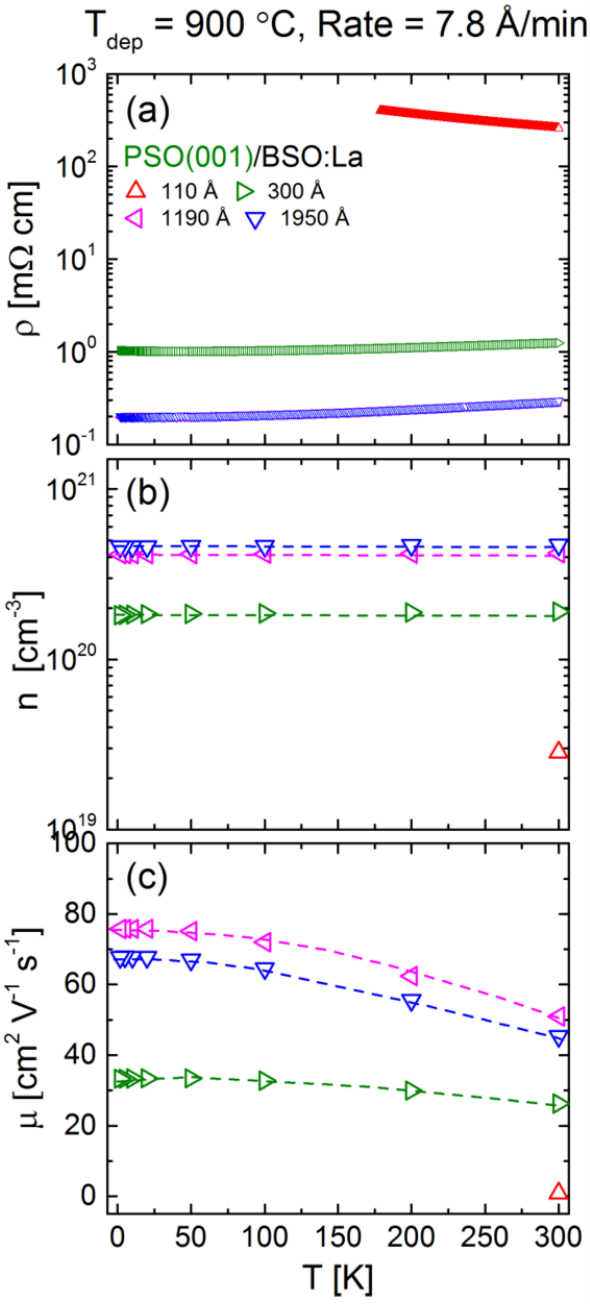

Fig. A11: Measurement temperature (*T*) dependence of transport properties (a) resistivity, ρ, (b) Hall electron density, *n*, and (c) Hall electron mobility, μ, for 100–2000-Å-thick BSO:La films grown on $PrScO_3$(001) substrates. Films were deposited at ~8 Å/min.

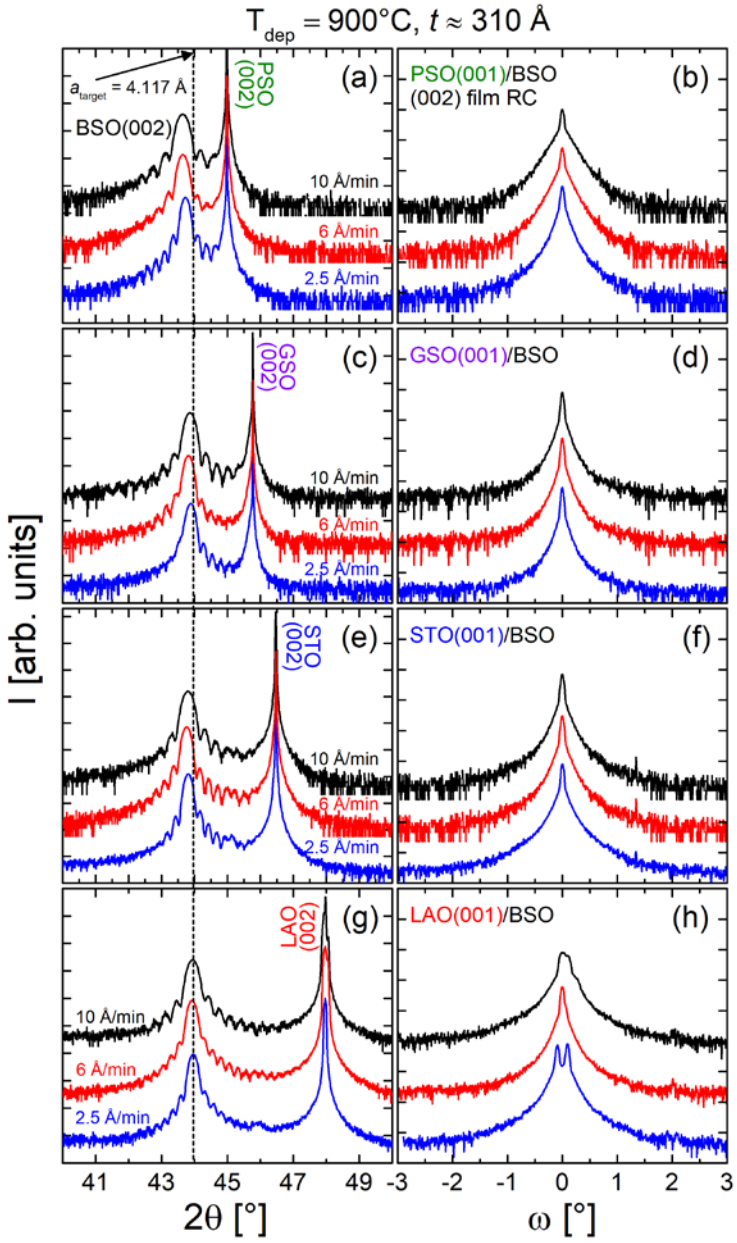

Fig. A12: High resolution WAXRD of 340-Å-thick BSO:La films deposited at different growth rates. Displayed are wide-angle θ–2θ coupled scans of the film/substrate 002 peaks (left panels), and complimentary 002 film RCs (right panels). (a), (b) films on PSO (001),

(c),(d) GSO (001), (e),(f) STO (001), and (g),(h) LAO. The dashed line indicates the bulk lattice parameter of the sputtering target. All films were deposited at 900°C.